Thermodynamical Stability Analysis of a Model Quasicrystal

Master Thesis of
Moritz Holzwarth

6.11.2022

Examiner: Prof. Dr. Johannes Roth
Co-Examiner: Prof. Dr. Christian Holm

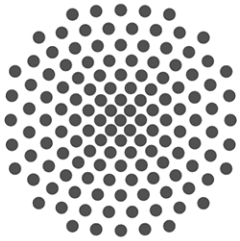

Institut for Functional Matter and Quantum Technologies
Universität Stuttgart
Pfaffenwaldring 57, 70569 Stuttgart

Contents

1 Introduction

Arguably one of the most interesting but also complicated questions in science is about how the vast variety of matter that we find in the universe comes about. There seems to be an endless diversity of macroscopic or microscopic properties by which materials can be classified and also distinguished. We experience several of such properties constantly in every day life, like the state of aggregation, the viscosity, the density, the stiffness, transparency and many more. Others are less obvious and require deeper scientific investigation, e.g. conductivity, the width of the band gap in semiconductors, radioactivity, binding energy or ionisation energy in gases, dia-, para- or ferroelectricity, the speed of sound or light inside a material, etc. Fundamentally, all these properties are related to the types of atoms that make up the material, the types of molecules to which the atoms may be joint together, and the way these molecules are arranged among each other. Specifically for solid matter, one of the most important concepts concerning the arrangement of a large number of atoms or molecules is 'order'. Since order is a familiar concept in everyday life it seems convenient to distinguish between ordered and disordered atom structures of solid matter. A term closely related to order is symmetry. The macroscopic symmetries that sometimes appear in natural crystals like diamond or pyrite were noticed and interpreted by humans already in antiques times [1]. However, the relation between macroscopic symmetries and the underlying ordered molecule arrangement is far from obvious. Already in 1611 Johannes Kepler proposed that the hexagonal symmetry of snowflakes should be related to the fact that the hexagonal packing of spheres must be the tightest possible. The latter mathematical conjecture was proven only in 1998 by Thomas C. Hales [2]. Also the term 'order' becomes harder to grasp if one tries to formulate it with mathematical exactness. Using the method of X-ray and electron diffraction physicists found a method that should distinguish microscopically ordered and disordered matter. While this tool helped to identify the lattice structure of many crystals, it also unleashed a question about the most essential properties that an ordered atomic or molecular lattice should have [3]. The idea of a crystal as a repetitive stacking of indistinguishable unit cells was challenged by a material that was found in 1982 by Daniel Shechtman [4] and was soon called a quasicrystal. Such quasicrystals do provide rotational symmetry and long range order in terms of their diffraction images, but they lack the translational invariance that is the most prominent feature of conventional crystals. Also, the relation between a quasicrystal's symmetry and its lattice is more subtle than for conventional crystals. Given one unit cell with its basis of atoms, the whole lattice of a periodic crystal is determined. But a quasicrystal does not have a unit cell. Given its symmetry group and atom composition, there are still infinitely many possibilities for the actual, microscopic lattice. This ambiguity is due to an extra degree of freedom usually called phasons. The phasons, which are local restructurings of the atom arrangements contribute a lot to the quasicrystal's entropy. It is hypothesized that the phason induced entropy is the crucial mechanism for thermodynamic stability of certain quasicrystals [5].

There have been several studies about this idea [6, 7, 8]. One model crystal that was created in a molecular dynamics simulation by Engel [9] showed quasicrystalline symmetry only at temperatures above zero. Also, small local restructurings called phasonic flips were a prominent feature in this material. The mathematical tessellation that could be recognized in its atom lattice is called the Tübingen triangle tiling (TTT). Later, a more theoretical approach based on the theory of the phasonic free energy and using the construction formalism of the TTT was given by Kiselev [10] to explain the observations in Engel's simulation. In the present thesis we want to recalculate Kiselev's results, which relied mostly on numerical methods, and use only geometrical computations that can in principle be carried out completely analytically. The central formalism is called the polar

calculus. It is based on the mathematical representation of quasicrystals as projections of higher-dimensional lattices onto a lower dimensional subspace, usually called the 'cut and project scheme'. Furthermore, we will propose several changes and extensions of Kiselev's work. Especially the correlations between two phasonic flips and their significance for the thermal QC-stability will be investigated. Throughout the thesis, several subtleties and curiosities of the theory of the phason elastic free energy in general will be highlighted and discussed.

The contents are structured as follows. Starting with section 2, the fundamental difference between conventional, crystallographic point symmetry groups and non-crystallographic or quasicrystalline point symmetries will be explained. Then, the concept of tilings and especially aperiodic tilings that are models for ideal quasicrystals is introduced. Here, a broad idea should be given about different aspects of aperiodic tilings, like substitution rules or local derivability, that are present in mathematical research. An important part of this overview will be the height representation, followed by the polar calculus. Deriving the latter distinctly for aperiodic and 1D periodic tilings should show its usefulness and relation to aperiodicity. Next, the phasonic strain will be introduced, which is necessary to understand the following discussion about random tilings and global phasonic strain-classes. In section 3, the work of Baake et al. [11], who invented the TTT is reviewed, as well as parts of the dissertation of Engel and diploma thesis of Kiselev. Proceeding to section 4, we show how 'flip densities', which are central for the free energy calculation, can be obtained from the polar calculus. Also an extended model of the phasonic free energy is presented that takes into account couplings between nearest neighbour flips. The results of these free energy calculations are then shown and discussed in section 5. Here we explicitly distinguish between different models that do or do not include flip correlations or certain flip restrictions as used by Kiselev. We finish by putting the results in relation with the random tiling hypothesis and with the quasicrystal from Engel's simulation.

2 Quasicrystals

In 1992, the International Union of Crystallography (IUC) changed its definition for 'crystal' [3]. Before, a crystal was identified as a homogeneous, anisotropic material made out of periodically ordered building blocks, and thereby distinguished from amorphous materials [12, 13]. The central feature of periodic order was first measured experimentally by Max von Laue using the revolutionary tool of X-ray diffraction in crystals [14]. He was awarded the Nobel Prize in physics in 1914. Since then the method of X-ray diffraction has developed magnificently. Today also other radiation like neutrons [15] or electrons [16] is used to measure structural and chemical properties of crystals. The diffraction patterns of crystals show a discrete and ordered grid of intensity points called Bragg peaks (fig. 1a).

Using the equations of von Laue and the reciprocal lattice formalism information about the crystal lattice and its symmetry group can be obtained from the relative positions of the spots in the diffraction pattern. For more on the theory of diffraction see [17]. Contrary to crystals, amorphous materials like glass [18], wood [19] or various kinds of plastic [20] show a continuous, blurry distribution of intensity as a diffraction image (fig. 1b). No Bragg peaks and hence no discrete symmetry is visible. This shows the lack of long range order in the probe. Because the diffraction pattern distinguishes between materials with and without an ordered lattice structure it can be used as the very definition of 'order' and therefore of 'crystal' [3].

This raises the question which atomic structures give rise to a discrete diffraction pattern and which cause a continuous one. Even though this question has not yet been answered completely on mathematical grounds, many examples have shown that there are a lot of different cases to be considered. Deterministically ordered point sets can also have continuous diffraction images and seemingly random point sets of maximal entropy can cause Bragg peaks [3, 21](chapter 9-11). Many of these mathematical point set examples were constructed purely for the purpose of a counter example and are not (yet) found in reality.

However, the condition of strictly periodic ordered atom lattices, which crystals previously were thought to inhabit, had to be dropped also outside of pure mathematics. In 1982 Dan Shechtman studied a metal alloy which showed a discrete diffraction pattern but had no periodic atom structure [4]. So the condition of periodicity shrunk from the defining crystal property to a characteristic feature that only a subset of crystals possesses. The new definition by the IUC calls a solid material a crystal "if it has essentially a sharp diffraction pattern"(Online Dictionary of Crystallography [24]). The position of each Bragg peak is given by a vector

$$H = \sum_{i=1}^{n} h_i \mathbf{b_i}, \tag{1}$$

where the $\mathbf{b_i}$ are the basis vectors of the reciprocal lattice and are linearly independent with integer coefficients h_i. If the number n of basis vectors is equal to the number of spacial dimensions of the material it is a conventional periodic crystal. If n is greater than the number of spacial dimensions the material is called a *quasicrystal*.

2.1 Noncrystallographic Symmetries

As suggested by their shape when growing freely (idiomorphic) [13](pages 14-16), crystals have a discrete point symmetry group. This group can contain operations like reflection

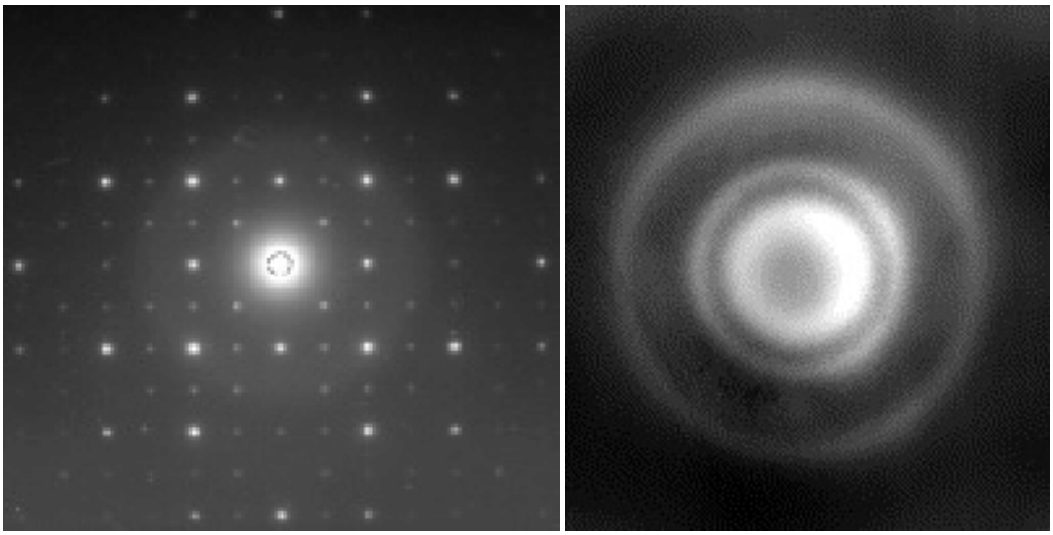

(a) X-ray diffraction image of NaCl. The pattern shows the crystal lattices cubic symmetry group O_h. [22]

(b) Diffraction image of amorphous calciumphosphat (ATCP). No discrete Bragg peaks are visible. [23]

Figure 1

on a plane, rotations and inversion. For background on group theory and its application in physics, see [25]. Lets consider an infinite periodic crystal lattice in two or three dimensions. The operations of a point group are then applied onto the lattice with respect to one fixed point that is not affected by any of the operations. The fixed point may or may not be chosen a lattice point. If all operations of a point group $\mathcal{G}$ map each lattice point again onto a lattice point, then $\mathcal{G}$ is a symmetry group of the crystal lattice. Periodic crystals additionally have translational symmetry. Shifting the infinite grid by any lattice vector $\mathbf{R}$ maps each lattice point again onto a lattice point. Except for $\mathbf{R} = 0$ such a shift allows no fixed points. It follows from the periodicity condition that the lattice vectors can be written as

$$\mathbf{R} = \sum_{i=1}^{n} h_i \mathbf{a}_i, \tag{2}$$

where h_i are integers, $n \in \{2, 3\}$ and the vectors $\mathbf{a}_i$ are a basis for the lattice. An element g of the symmetry group $\mathcal{G}$ applied onto a basis vector gives

$$g(\mathbf{a}_i) = \sum_{j=1}^{n} g_{ij} \mathbf{a}_j. \tag{3}$$

The numbers g_{ij} are the matrix elements of g represented in the the basis $\{\mathbf{a}_i\}$. Since the right expression in eq. (3) must be again a lattice vector of form (2) and the basis vectors $\{\mathbf{a}_i\}$ are linearly independent it follows that all g_{ij} must be integers. Now let g be a rotation operation around some axis by angle ϕ, and lets switch to the euclidean basis $\{\mathbf{e}_x, \mathbf{e}_y, \mathbf{e}_z\}$. Then for $n = 3$ and $\mathbf{e}_z$ parallel to the rotation axis g is represented by the matrix

$$\mathbf{M}(g) = \begin{bmatrix} \cos\phi & -\sin\phi & 0 \\ \sin\phi & \cos\phi & 0 \\ 0 & 0 & 1 \end{bmatrix}. \tag{4}$$

For $n = 2$ it would be just the 2×2 matrix in the upper left block. It is well known from linear algebra that the trace of a matrix is independent of the basis. So since the trace of g in the g_{ij}-representation was obviously an integer it follows that

$$2\cos\phi \in \mathbb{Z} \tag{5}$$

for $n = 2$ or $n = 3$. This leads to the famous crystallographic restriction, i.e.: if $\phi = \frac{2\pi}{n}$ eq. (5) is fulfilled only for $n \in \{1, 2, 3, 4, 6\}$. So the point symmetry group $\mathcal{G}$ of a periodic crystal can contain no rotations of order 5 or higher than 6. These forbidden symmetries used to be called *non-crystallographic*. In 2D, there are only two types of point groups, namely the cyclic groups C_n and the dihedral groups D_n, leaving us with ten crystallographic 2D point groups. For 3D it was known since 1830 [26] that there are 32 point groups satisfying the crystallographic restriction [27].

The point symmetry group of the crystal lattice determines the point symmetry group of the diffraction pattern, but they are in general not identical. One difference is that a 3D crystal can have different rotational symmetries around different axis. So the diffraction pattern, which can only show 2D point symmetries, must be recorded along several symmetry axis. Then, the 3D point group obtained from combining all the 2D point groups will be one of the 11 Laue classes [28]. The Laue classes follow directly from the 32 crystallographic point groups as their direct product with the inversion symmetry. This is due to Friedels law, which states that the diffraction image is always centrosymmetric [17](pages 97-98). In general, the true point symmetry group of the crystal lattice cannot be obtained from the Laue class alone, but it will always be a subgroup of the Laue class. There are other methods, like dynamical diffraction [29] or anomalous scattering [30], to find the true point group of the lattice but they will not be explained here.

Knowing all this about crystals, it was a striking observation when Dan Shechtman and his team measured the electron diffraction images of an AlMn alloy along various axis (fig. 2). Especially the patterns on top and bottom right are remarkable. Clearly they have tenfold rotational symmetry, and therefore do not occur in any of the Laue classes. They might correspond to a ten- or fivefold symmetrical axis in the crystal lattice, both violating the crystallographic restriction. So the material cannot be a periodic crystal. In total six tenfold, ten sixfold and fifteen twofold axis were found. Because of the sharp Bragg peaks it is clear that the true point symmetry group of this crystal lattice must be of finite order. Only amorphous materials are isotropic (on large scales) and show continuous diffraction with spherical symmetry. It is another well known fact from group theory that in 3D only few types of rotation axis are compatible with each other. Such combinations of rotation axes must be excluded where the respective rotation around different axis would correspond to a total rotation angle of $2\pi\alpha$ where α is irrational. This leads to only three types of polyhedral groups (with more than one rotation axes of order >2): The tetrahedral, octahedral and icosahedral point group. None of these have a tenfold axis and only the icosahedron has fivefold axis. And indeed, by comparing the symmetries of the icosahedral group and the diffraction pattern (with sixfold and tenfold diffraction symmetry corresponding to threefold and fivefold lattice symmetry respectively) they coincide.

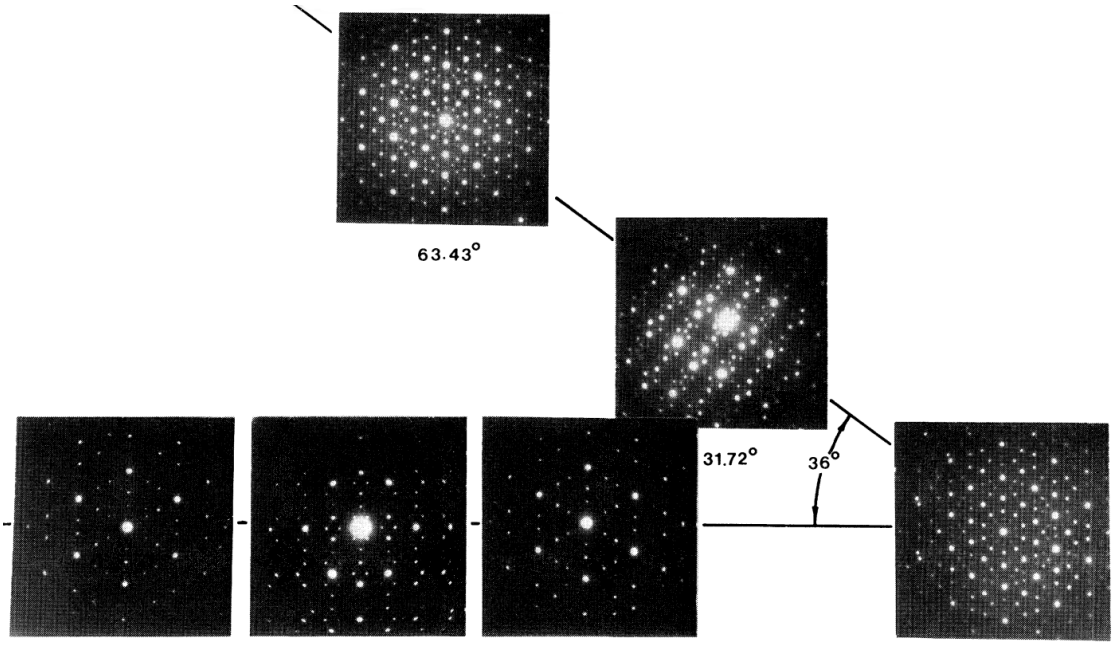

Figure 2: Electron diffraction patterns of AlMn from the original paper on the discovery of quasicrystals. Two of the images have tenfold symmetry, representing the fivefold axis of an icosahedron [4].

After Shechtmans revolutionary work, further materials with quasicrystalline symmetry (meaning rotation of order $n = 5$ or $n > 6$) were discovered in laboratories. Besides the icosahedral symmetry there are also 2D quasicrystals with rotational symmetry of order 8 [31], 10 [32] or 12 [33]. In 2009 the first discovery of a non-synthetic quasicrystal by Paul Steinhard and Luca Bindi and their team was announced [34]. It is called icosahedrite due to its icosahedral symmetry. An analysis of the rock in which the small icosahedrite samples where found suggests that it might be of extraterrestrial origin [35]. It is suggested that the quasicrystal might have formed upon a strong explosion or collision of meteorites. This idea is supported by the finding of another quasicrystal which was created unintentionally in the first nuclear bomb explosion at Alamogordo, New Mexico [36].

Naturally, the question arises what this crystal lattice with icosahedral or other unconventional symmetry looks like. How is it possible to inhabit long range order without being periodic?

2.2 Tilings and their Construction

Before physical quasicrystals were discovered mathematicians already thought about aperiodic tilings. In a tiling (or tessellation) the infinite two dimensional plane is covered by an infinite repetition of one or several different prototiles (shapes) without overlapping and without gaps. The concept can be generalized to three dimensions and higher. For 2D periodic tilings, there are only 17 types characterized by their symmetry group, called wallpaper group [38]. In 3D, there are 230 types of periodic space tilings, characterized by 230 crystallographic space groups [13](pages 173-182). The wallpaper and space groups are not to be confused with the point symmetry groups mentioned before, as they also include operations like translations, screw displacements or glide reflections. Clearly, periodic tilings are a mathematical, or even artistic (cp. fig. 3) representation of

Figure 3: The tessellation 'Two Birds' by M.C. Escher (1938) is a periodic 2D tiling using two prototiles: the white and the blue bird. [37]

periodic crystal lattices. So it seems justified to believe that non-periodic tilings might be a way to model quasicrystals.

2.2.1 Examples of 2D Aperiodic Tilings

The attributes aperiodic, quasiperiodic and almost periodic are often used in similar manners. We will stick to the term 'aperiodic' in this work since it is most prominently seen in the context of tilings. Quasicrystals will be seen as a special kind of aperiodic crystals. In the mathematical definition, a tiling $\mathcal{T}$ of $\mathbb{R}^d$ is called aperiodic if its hull contains only non-periodic tilings [21](page 79). The hull of a tiling is the closure of the set of all translated tilings $\overline{\{\mathcal{T} + x | x \in \mathbb{R}^d\}}$, which also includes tilings being translated infinitely far. In simpler words this means that aperiodic tilings are distinguished from non-periodic tilings by excluding tiling sequences like *..aaabaaa..* (with the *a*s continuing forever), which are non-periodic but contain periodic sub-sequences of arbitrary length.

One of the most famous aperiodic tilings is the Penrose rhomb tiling (PT) (fig. 4a) discovered 1974 by Roger Penrose [39]. It uses only two kinds of tiles (a thick and thin rhombus), which, so far, is the smallest number of prototiles used in an 2D aperiodic tiling. In 3D, the Schmitt–Conway–Danzer biprism is an example for a single prototile that can tile space only non periodically [41], while in 2D the existence of such a single, connected, aperiodic prototile is an open question ('einstein problem' [1] [42]). The PT shows a tenfold symmetrical diffraction pattern, very similar to those found in various quasicrystals. The diffracion pattern (fig. 4b) was calculated from a lattice where a pointlike atom was assumed at all the corners of the rhombs.

Due to its many fivefold symmetric, local structures, like stars and rings, the PT might

[1] In German, 'einstein' translates to 'one stone'. The word is also used in English literature concerning this problem. That one stone refers to a single prototile that can tile the plane only aperiodicly.

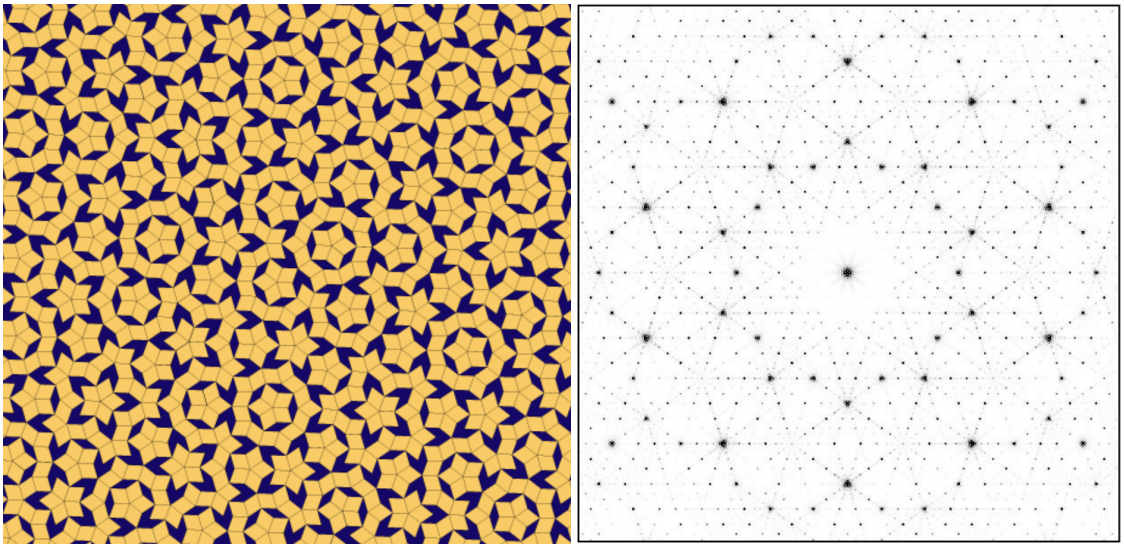

(a) A patch of the rhombic Penrose tiling, also known as P3. [39]

(b) Diffraction pattern of the rhombic Penrose tiling. The patch used to calculate this was much larger than the one on the left. [40]

Figure 4

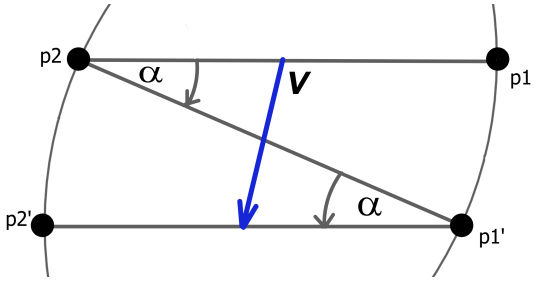

Figure 5: Sketch of two respective rotations around different rotational centres.

seem to be only fivefold symmetric, like the icosahedron. But actually its full point symmetry is the decagonal dihedral group D_{10}. However, rotational symmetry has a different meaning in the context of aperiodic tilings as for periodic tilings. There every lattice point could be the center of rotation for the full point group. For an aperiodic tiling there can be at most one center of rotation, which would have only fivefold symmetry in the case of the PT. This can be understood geometrically (fig. 5). Assume there were two rotation centres p1 and p2 with distance l. Then after two respective rotations around p1 and then p2 by the same angle α the tiling should look identical. But this operation is the same as a translation by a vector $\boldsymbol{v} = l(\cos\alpha - 1, -\sin\alpha)$. So the tiling would be also periodic with respect to $\boldsymbol{v}$.

To define point symmetry in the context of quasicrystals, one must first know about the concepts of tiling patches and local indistinguishability. The following definitions are taken from [43]. A patch of radius r is simply a finite subset of a specific tiling. $P(r, q)$ denotes a patch that lies completely inside a circle of radius r around a point q. If any arbitrary patch of one tiling A is, up to translation, also contained in a different tiling

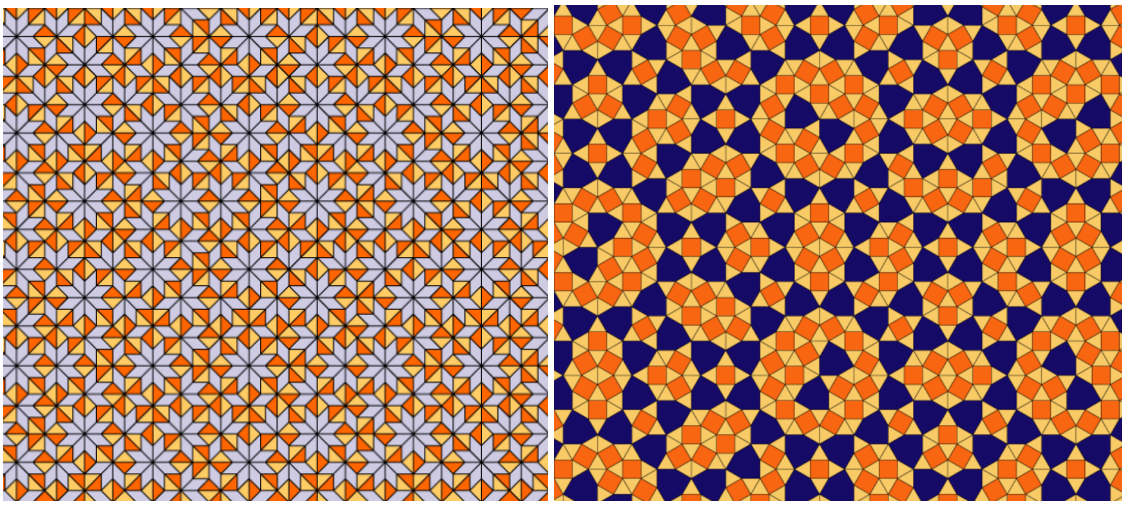

(a) The Ammann-Beenker tiling with 8-fold rotational symmetry. [39]

(b) The shield tiling with 12-fold rotational symmetry. [39]

Figure 6

B and vice versa these tilings are called locally indistinguishable (LI). It is common to say that the tilings are in the same local indistinguishability class (LI-class) since the local indistinguishability is an equivalence relation. Now, a tiling $\mathcal{T}$ is symmetric to an operation g of some point group $\mathcal{G}$, if, and only if, $\mathcal{T}$ and the transformed tiling $g(\mathcal{T})$ are in the same LI-class.

Graphically this means for any finite region of the PT also all the rotations and reflections of that region with respect to D_{10} can be found in the PT. Examples for 8-fold and 12-fold symmetric tilings are the Ammann-Beenker tiling, found by Robert Ammann in 1977 [39], and the so-called shield tiling, found by Franz Gähler [39] (fig. 6a and 6b). In the case of periodic tilings, this generalized symmetry definition coincides with the previous definition. For periodic tilings, the point symmetry and translational symmetry are combined to one space group. In [44], the concept of space groups has been extended and applied to 2D quasicrystals, based only on the lattice in the diffraction pattern.

2.2.2 Matching Rules and Inflation Symmetry

There are many ways to construct aperiodic tilings as the ones above. And not all methods work for all tilings. However, all popular tilings in the research around quasicrystals (all tilings in the tiling encyclopedia [39]) can be created using a substitution rule (SR). Such a recursive construction starts with any finite patch of tiles. Each tile is scaled up (inflated) by a certain factor and decomposed into tiles of the original size. Repeating this process again and again creates the full tiling (an element of the LI-class). Two congruent prototiles can have different decomposition rules. This is mostly displayed by using different colors for equally shaped tiles or by decorating them with symmetry breaking arrows.

The SR for the rhombs of the PT is shown in fig. 7a. Its inflation factor is the golden ratio (or golden mean) $\tau = \frac{1+\sqrt{5}}{2}$. The curved, orange lines can be used to describe matching rules, which will be explained later. The substitution rule can also be seen as an additional symmetry of the tiling. Applying the SR to a complete, infinite tiling

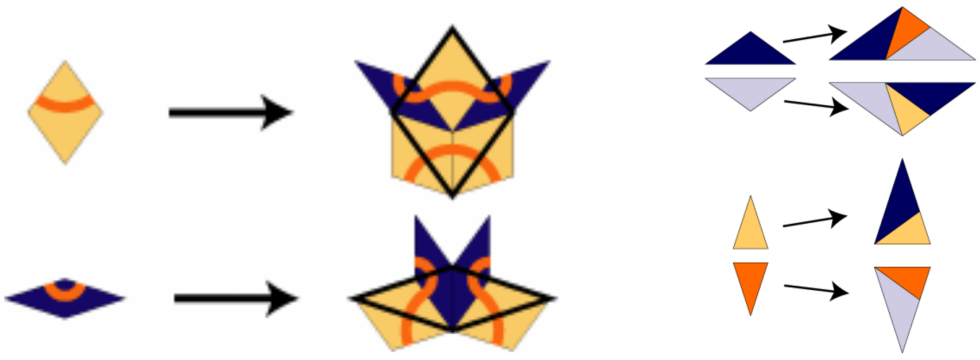

(a) Substitution rule for the rhombic PT. [39] (b) Substitution rule for the PT using golden triangles. [39]

Figure 7

results again in a tiling of the same LI-class. This is called inflation symmetry. Similarly, performing the inverse SR on an infinite tiling is called deflation symmetry. There several tiles are glued together to create a larger version of the tiling, which is then scaled down by the inverse inflation factor.

Let us leave the rhombs for a moment and consider two triangles as prototiles following a SR as in fig. 7b. Here, the effect of asymmetric decomposition rules mentioned earlier occurs. The two obtuse (light and dark blue) triangles are congruent tiles, and so are the two acute (orange and yellow) triangles. Distinguishing two triangles with identical shape and size through colors shows that they are differently (mirrored) disassembled within the SR. Fig. 8a shows the tiling that is created by the SR of fig. 7b (still with the colour coding), which also has τ as inflation factor. It is actually just another version of the PT. By gluing together the bottom sides of all the light and dark obtuse triangles as well as for all the red and yellow acute triangles, the rhombic PT of fig. 4a emerges. This process of gluing together triangles is a simple example of uniformly locally deriving one tiling from another. Vice versa, there is a unique process of cutting the rhombs of the rhombic PT in two to obtain the triangular PT.

This equivalence relation between the tilings of fig. 4a and 8a is called 'mutual local derivability' or 'local equivalence'. The two tilings are in the same mutual-local-derivability-class (MLD-class). The mathematical definition of an MLD-class, found in [43], is more abstract. A tiling $\mathcal{T}_1$ is locally derivable from a tiling $\mathcal{T}_2$ with derivability radius R_{21} iff: Any two patches $P_{\mathcal{T}1}(r,h)$, $P_{\mathcal{T}1}(r,k)$ of radius r in tiling $\mathcal{T}_1$ at positions h and k are equal if the patches $P_{\mathcal{T}2}(r+R_{21},h)$, $P_{\mathcal{T}2}(r+R_{21},k)$ of radius $r+R_{21}$ in tiling $\mathcal{T}_2$ at the same positions are equal. If $\mathcal{T}_2$ is also locally derivable from $\mathcal{T}_1$, with a possibly different derivability radius R_{12}, then the tilings are in the same MLD-class. The derivability radius gives a measure for how large a patch around some position in a tiling $\mathcal{T}_1$ is needed to derive any information about that positions environment in another tiling $\mathcal{T}_2$. Given a lattice of atoms with a quasicrystalline symmetry, there is an ambiguity of which tiling models its structure best. The choice of different tilings in an MLD-class to describe a quasicrystral can be seen as a generalization of the choice of different unit cells that can describe a periodic lattice.

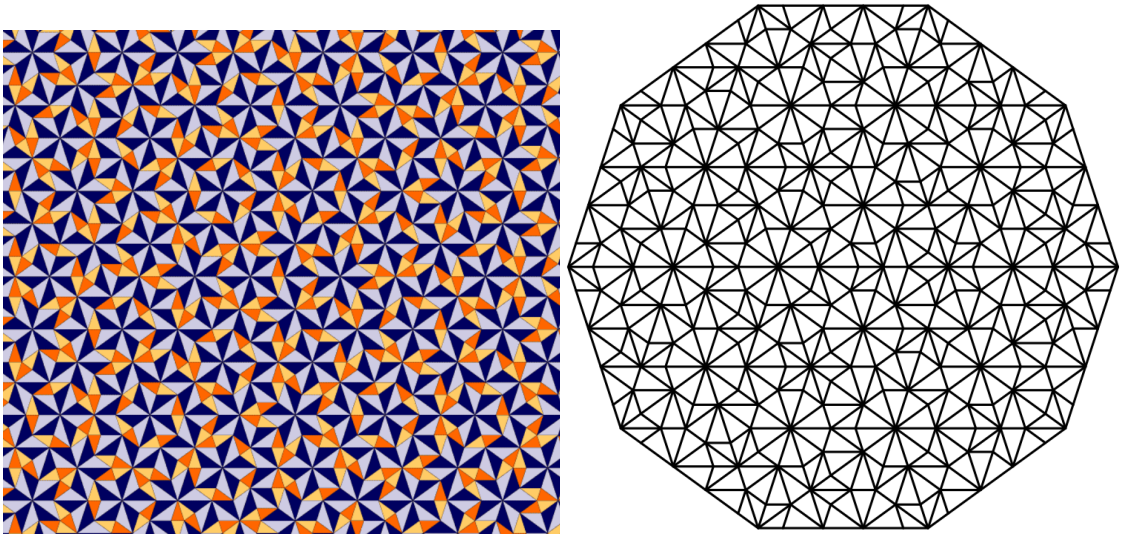

(a) The Penrose pattern, where the rhombs are split into two triangles. This pattern is obtained from the substitution rule in fig. 7b. [39]

(b) The Robinson decomposition pattern, which follows from the substitution rule in fig. 9a. It is MLD with the PT. [43]

Figure 8

Lets look at another, less obvious element of the Penrose MLD-class. The tiling in fig. 8b is called Robinson's decomposition (RD). Apart from the typical pentagonal stars, it also shows decagonal structures. Its SR is seen in fig. 9a where arrow decorations are used to specify the tile decomposition. The RD tiles have the same triangular shape as the tiles in the triangular PT (fig. 8a) but the ratio of the two triangle areas is inverted (acute : obtuse $= \tau : 1$). To recover the triangular PT from RD, one obtuse and acute triangle must be glued together to create a similar obtuse triangle that is larger by a factor τ^2 as shown in fig. 9b. In general the elements of an MLD-class can look quite different from each other. A variety of elements of the Penrose-MLD-class can be found in [39]. It should also be mentioned that not all tilings with a certain symmetry (D_{10} for the PT) are in the same MLD-class. An example will be shown later.

Taking a look at the rhombic PT (fig. 4a), one finds that the rhombs are only put together in certain, specific manners. The variety of possible finite tile combinations is much larger than the number of present configurations. For example, the fivefold star made from five yellow (obtuse) rhombs shows up very frequently. But a tenfold star (fig. 10b), which could be built from ten blue (acute) rhombs, never occurs. This information that is stored in the tile arrangements was first extracted into a simple statement by N.G. de Brujin in 1980 as the nowadays well known concept of matching rules [46]. One example of matching rules are the orange lines drawn on the Penrose rhombs in fig. 7a. The rule is: If the lines are never broken anywhere in the tiling, then it is truly an element of the LI-class that is generated by the SR.

There are various other ways to manifest equivalent matching rules on the prototiles. The original modification of de Brujin used different types of arrows on the rhombs edges (fig. 10a(1)). The condition is then that for any two tiles sharing an edge the arrows of their common edges must be of the same type and pointing in the same direction. These

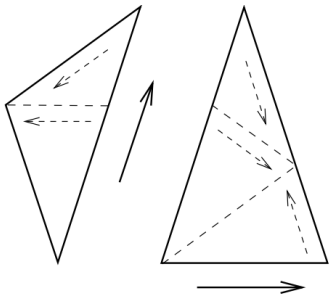

(a) Substitution rule for the RD. [43]

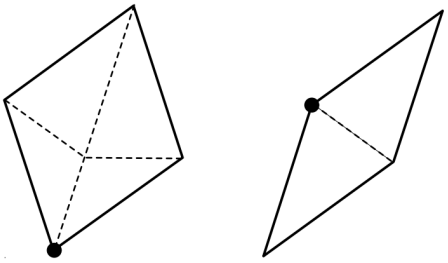

(b) The local transformation rule to derive the rhombic or triangular PT from the RD and vice versa. [43]

Figure 9

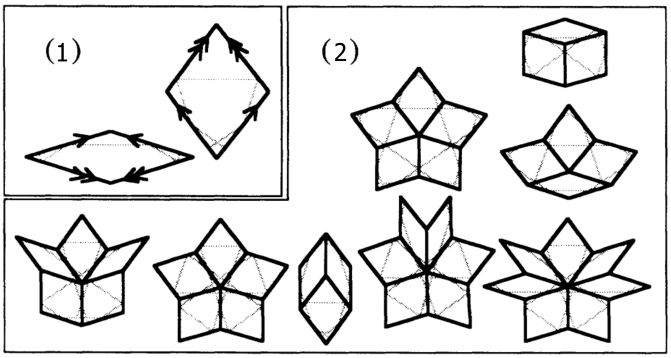

(a) (1): Rhombs with arrows to express matching rules for the rhombic PT. (2): The eight vertices of a perfect PT satisfying the matching rules. [45]

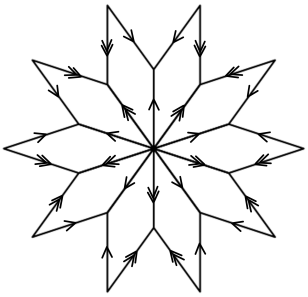

(b) This decagonal star-vertex is not present in the PT. It can be created by successively adding tiles without violating the matching rules (arrow condition). Only when more surrounding tiles are added a violation would occur.

Figure 10

kinds of matching rules are said to be strong since they force the right LI-class. They are also local as each tile must be compared only to a few neighbouring tiles to check its validity. Strong, local matching rules can be formulated for many other aperiodic tilings beside the PT, but not for all. There are also weak matching rules which only guarantee that a tiling is not too different from a certain LI-class. For a detailed explanation of how the difference between LI-classes is measured and for more information on which tilings posses strong matching rules see [47].

The concept of matching rules is of interest in the quasicrystal community because it might be interpreted as local information exchange between tiles that could correspond to local interactions between the particles that build a real quasicrystal. Ever since quasicrystals were discovered, people in the crystallographic community were puzzled

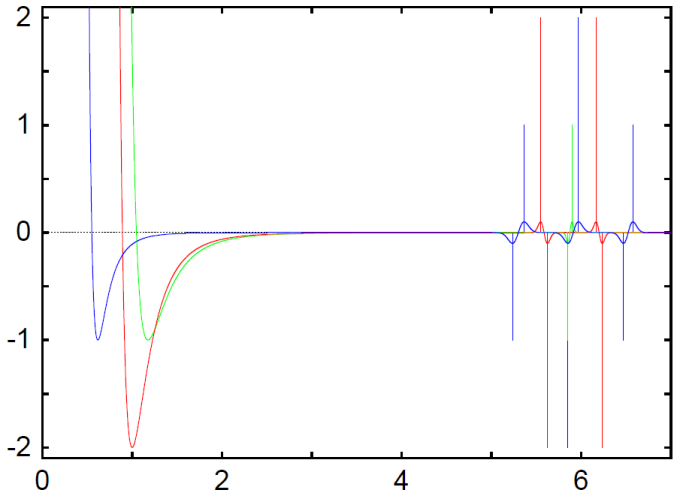

Figure 11: Pair potentials to grow a binary tenfold symmetric quasicrystal. The different colored potentials correspond to interactions between atoms of the same type (blue, green) and atoms of different type (red). [48]

about the microscopic mechanisms that can form structures non-periodically but with long range order. However, the matching rules are only well-defined when applied to an already existing, infinite tiling. A finite structure like the tenfold star of acute rhombs (fig. 10b) might not contradict the matching rules by itself (arrow condition in shared edges). But it would determine contradictions in the further tessellation around. So simply sticking tiles together and only obeying the arrow condition everywhere does not at all ensure a proper quasicrystal growth. Nevertheless, proper growth rules, as an extension of matching rules, were defined for the PT using additional growth conditions [45]. Apart from the arrow rule, it is also demanded that each vertex (a point where several tile corners meet) must be one of the eight vertices shown in fig. 10a(2) (vertex condition). Also, it is not allowed to freely add tiles to an ambiguous position (in accordance with the arrow condition) when there are still other positions left which force a certain tile by the vertex condition. The authors discuss how these rules still might correspond to natural molecular growth behaviour. But it certainly must be quite complex interactions between the particles to reproduce these rather artificial looking conditions.

In the dissertation of Koschella pair interaction potentials were constructed to grow a stable quasicrystal ground state in a simulation with two kinds of atoms (binary tiling) [48]. The stabilized crystal lattice was a decagonal tiling constructed from the Penrose-rhombs, but not LI with the PT discussed before. These potentials are based on a Lennard-Jones-potential with additional maxima and minima (figure 11). The distances between these new maxima and minima is quite large compared to the usual LJ-minimum. Also their position must be chosen extremely precise, otherwise forbidden configurations in the crystal structure are supported.

2.2.3 The Height Representation for 1D Crystals

Another way to construct many of the better known aperiodic tilings is the *height representation*, also known as *cut and project scheme* (CPS). It allows to create uncountably many different LI-classes of tilings with as little as a single parameter to distinguish them exactly. This scheme also gives the fascinating perspective on quasicrystals as generalized crystals in higher dimensions. Recall that the crystallographic restriction,

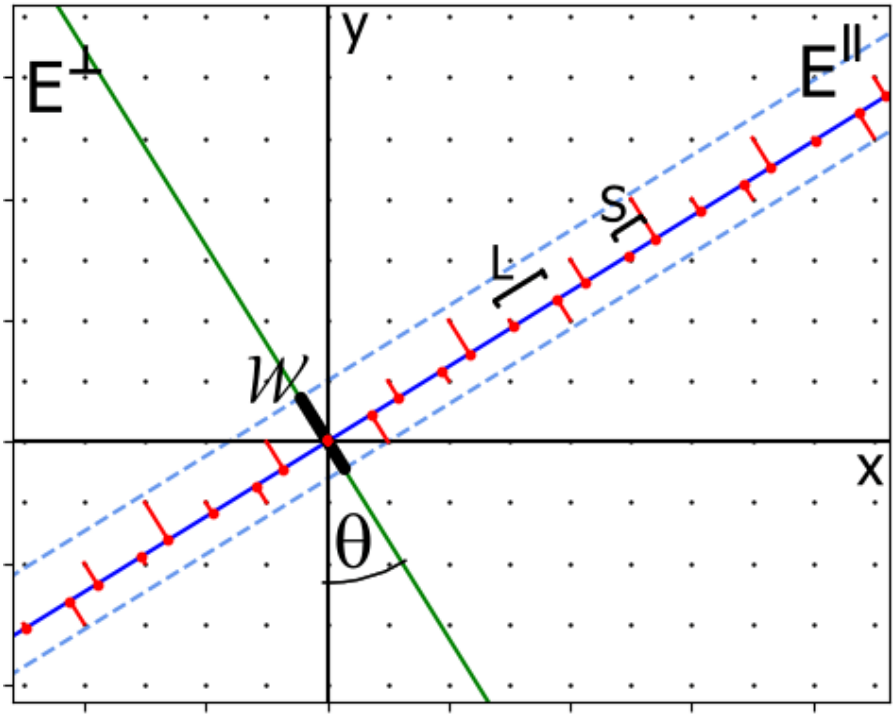

Figure 12: Construction of a one-dimensional CPS-crystal. The window $\mathcal{W}$ defines a strip. All hyperlattice points inside it are projected onto $E^{\parallel}$.

which led to the distinction between periodic and aperiodic crystals, was limited to two and three dimensions. For simplicity though, the CPS will first be demonstrated with a one-dimensional system, where the aspect of rotational symmetry is naturally neglected. Later, the concept will be generalized and also used for 2D crystals. The term *CPS-crystal* (or *-tiling*) will be used to emphasize that a certain periodic or aperiodic crystal (or tiling) is constructed from a height representation.

For a one-dimensional CPS-crystal, first consider the 2D plane $\mathbb{R}^2$ and the two dimensional square lattice $\mathbb{Z}^2$. $\mathbb{R}^2$ is then subdivided into two one-dimensional subspaces $E^{\parallel}$ and $E^{\perp}$

$$\mathbb{R}^2 = E^{\parallel} \oplus E^{\perp}. \tag{6}$$

$E^{\parallel}$ will be called *parallel space* (in some literature also referred to as physical space). $E^{\perp}$, being perpendicular to $E^{\parallel}$, will be called *perpendicular space*. Each choice for parallel and perpendicular space can be labeled by an angle θ. $E^{\parallel}$ and $E^{\perp}$ are simply rotations of the x and y-axis around the origin by θ. While $\mathbb{R}^2$ and $\mathbb{Z}^2$ are easiest defined in the euclidean basis $\{\mathbf{e}_x, \mathbf{e}_y\}$, the rotated basis vectors $\mathbf{k}^{\parallel}$ and $\mathbf{k}^{\perp}$ are used to span the parallel and perpendicular space. Let $v^{\parallel}$, $v^{\perp}$ denote the projections of a vector $\boldsymbol{v} \in \mathbb{R}^2$ onto $E^{\parallel}$, $E^{\perp}$, realized by projection operators $\mathbf{P}^{\parallel}$, $\mathbf{P}^{\perp}$, respectively. Next, one defines a finite area subset of the perpendicular space, which will be called the window $\mathcal{W} \subset E^{\perp}$ (sometimes also acceptance domain). In general, the window can be any relatively compact area with non-empty interior [21](page 263-264). A well known-tiling can be obtained by choosing $\mathcal{W}$ as the projection of the half open unit square $S = \{(a, b) \in \mathbb{R}^2 | 0 \leq a \leq 1; 0 \leq b < 1\} \subset \mathbb{R}^2$ onto $E^{\perp}$

$$\mathcal{W} = \{v^{\perp} | \boldsymbol{v} \in S\} = \mathbf{P}^{\perp} S. \tag{7}$$

This is the half open interval $[-\sin\theta, \cos\theta)$. The half-open-condition of $\mathcal{W}$ is a specific choice for the example tiling, which is about to be constructed. The set of all points reached by translating $\mathcal{W}$ along $E^{\parallel}$ defines a strip $\mathcal{S}$ around $E^{\parallel}$ (blue dotted lines in figure 12)

$$\mathcal{S} = \{\boldsymbol{\mathcal{W}} + \boldsymbol{v} | \boldsymbol{v} \in E^{\parallel}\}. \tag{8}$$

The bold symbol $\boldsymbol{\mathcal{W}}$ denotes the window to be embedded in $\mathbb{R}^2$ and represented by 2-component vectors. Now, all the points of $\mathbb{Z}^2$ that lie inside this strip are projected onto $E^{\parallel}$. The lattice of projected points finally is the one-dimensional CPS-crystal $\mathcal{Q}$. While the strip is a nice geometrical representation of this construction, it is not really necessary in the mathematical sense. The $\mathbf{P}^{\parallel}$-projection $v^{\parallel}$ of a lattice point $\boldsymbol{v} \in \mathbb{Z}^2$ is a part of the CPS-crystal $\mathcal{Q}$ if the $\mathbf{P}^{\perp}$-projection $v^{\perp}$ of $\boldsymbol{v}$ lies within the window $\mathcal{W}$

$$\mathcal{Q} = \{v^{\parallel} | \boldsymbol{v} \in \mathbb{Z}^2 \wedge v^{\perp} \in \mathcal{W}\}. \tag{9}$$

$\mathcal{Q}$ is only a lattice without tiles so far. In the one-dimensional example the tiles can easily be defined as the two possible lengths L (long) and S (short) between two lattice points. The number of prototiles follows from the specific choice of $\mathcal{W}$. Two adjacent points in $\mathcal{Q}$ are also nearest neighbours in $\mathbb{Z}^2$. So one step along the quasicrystal lattice corresponds either to one step up (for S-tile) or one step to the right (for L-tile) in $\mathbb{Z}^2$-lattice. Because the strip is bounded by the corners $(0,1)$ and $(1,0)$ of the square S and the upper corner is not included, there is always only one possible move for the next step for any θ. If the point $(0,1)$ was also included in $\mathcal{W}$, the ambiguous step following the point $(0,0)$ would lead to a new tile of length $L - S$.

The cut and project scheme can also be formulated in a slightly different but completely equivalent way, which is sometimes helpful for visualisation. Let us rewrite the definition of $\mathcal{Q}$ using $v^{\perp} = \mathbf{P}^{\perp}\boldsymbol{v}$

$$\begin{aligned}
\mathcal{Q} &= \{v^{\parallel} | \boldsymbol{v} \in \mathbb{Z}^2 \wedge \mathbf{P}^{\perp}\boldsymbol{v} \in \mathcal{W}\} \\
&= \{v^{\parallel} | \boldsymbol{v} \in \mathbb{Z}^2 \wedge \exists w \in \mathcal{W} : \mathbf{P}^{\perp}\boldsymbol{v} = w\} \\
&= \{v^{\parallel} | \boldsymbol{v} \in \mathbb{Z}^2 \wedge \exists w \in \mathcal{W} : \mathbf{P}^{\perp}\boldsymbol{v} - w = 0\} \\
&= \{v^{\parallel} | \boldsymbol{v} \in \mathbb{Z}^2 \wedge 0 \in \mathbf{P}^{\perp}\boldsymbol{v} - \mathcal{W}\} \\
&= \{v^{\parallel} | \boldsymbol{v} \in \mathbb{Z}^2 \wedge 0 \in \mathbf{P}^{\perp}(\boldsymbol{v} - \boldsymbol{\mathcal{W}})\}.
\end{aligned} \tag{10}$$

The geometric interpretation of eq. (10) is shown in figure 13. The inverted window is attached to all points in $\mathbb{Z}^2$. In this case, the windows are also called *atomic surfaces*. If the atomic surface of a certain lattice point intersects the physical space $E^{\parallel}$, this point will be part of the CPS-crystal $\mathcal{Q}$.

Given the lattice $\mathbb{Z}^2$ and the definition of $\mathcal{W}$ as eq. (7), the defining parameter for all these CPS-tilings is the angle θ, or equivalently, the slope $m^{\parallel} = \tan(\theta)$ of $E^{\parallel}$ in $\mathbb{R}^2$. Choosing the slope as a rational number $m = p/q \in \mathbb{Q}$ the sequence of L and S will repeat after $p + q$ steps. This is most easily seen in the strip-picture (fig. 12). Each line parallel to $E^{\parallel}$ that cuts through a $\mathbb{Z}^2$-point in the first $p + q$ steps (q in $\mathbf{e}_x$ direction, p in $\mathbf{e}_y$ direction) will do so again after exactly $p + q$ steps. So a rational slope of $E^{\parallel}$ creates a periodic crystal with $p + q$ points in the unit cell. Vice versa, also all periodic CPS-crystals correspond to a rational slope $m^{\parallel}$. If the sequence of L and S repeats, so must the 'staircase' of up- and right-steps in $\mathbb{Z}^2$.

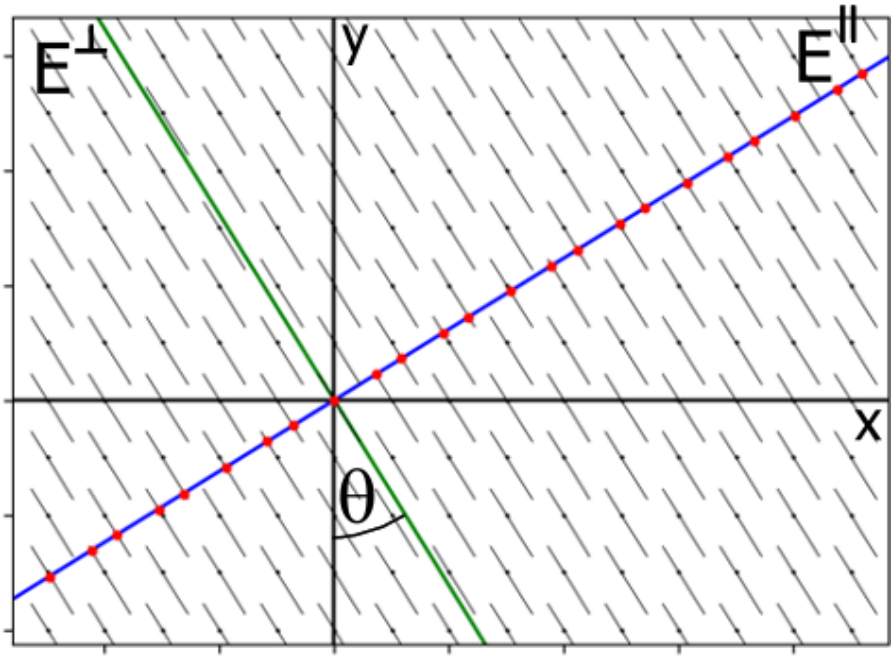

Figure 13: Construction of a one dimensional CPS-crystal. Each hyperlattice point has an inverted atomic surface, $-\mathcal{W}$, attached. If it intersects $E^{\parallel}$, the point is part of the crystal by projection.

So there is a one to one correspondence between periodic CPS-crystals and rational slopes. Then on the other hand there must be a one to one correspondence between aperiodic CPS-crystals and irrational slopes. The irrational slope of $E^{\parallel}$ is also equivalent to the condition that $E^{\parallel}$ and all its parallel lines contain at most one point of $\mathbb{Z}^2$. This again is equivalent to the mapping $\mathbf{P}^{\perp} : \mathbb{Z}^2 \mapsto \mathbf{P}^{\perp}(\mathbb{Z}^2)$ being bijective. It is clear that non-periodic crystals with infinitely long periodic subsequences, like $..LLLSLLL..$ (hence not aperiodic) cannot be created in the CPS. An infinite line of L-tiles would correspond to an infinite number of steps in x-direction, which is only possible for $m^{\parallel} = \theta = 0$.

Each θ creates a tiling of a different LI-class. So the difference of angles $\theta_1 - \theta_2$ could be seen as measure of how much the LI-classes of two 1D CPS-tilings $\mathcal{T}_1$, $\mathcal{T}_2$ deviate from each other. Shifting the $E^{\parallel}$-$E^{\perp}$ coordinate system in $\mathbb{R}^2$ changes the tiling but preserves the LI-class. One nice aperiodic sequence is obtained from choosing the inverse golden ratio $1/\tau$, which already showed up in the Penrose tilings, as the slope. This time, the aperiodic structure is known as the Fibonacci chain. The name is not only due to the prominent role of the golden ratio in this construction. Its SR is also based on the famous Fibonacci sequence. Starting with an S-tile, it is just scaled up by inflation factor τ to become an L-tile. Scaling the L-tiles by τ, it can be decomposed into a pair of tiles LS of the previous size.

$$S \to L \to LS \to LSL \to LSLLS \to LSLLSLSL \to LSLLSLSLLSLLS... \qquad (11)$$

From the third iteration on, all strings F_i can be written as the joined together previous two strings like $F_i = F_{i-1}F_{i-2}$.

2.2.4 The Height Representation for 2D Crystals

Now lets generalize the above construction of a CPS-crystal to two dimensions. A 2D aperiodic lattice may or may not inhabit a generalized rotational symmetry. Lets call those 2D lattices with generalized rotational symmetry of order $n = 5$ or $n > 6$ 2D quasicrystals (QC). Assume we are interested in constructing a 2D quasicrystal $\mathcal{Q}$ with rotational symmetry of order n. The construction starts from a hyperspace $\mathcal{H}$ with a periodic hyperlattice $\mathcal{L}$. In the 1D example, it was $\mathcal{H} = \mathbb{R}^2$ and $\mathcal{L} = \mathbb{Z}^2$. In principle $\mathcal{H}$ can be any locally compact abelian group [21](page 263), but for this work, $\mathcal{H} = \mathbb{R}^m$ is always sufficient. The hyperlattice $\mathcal{L}$ will deviate from a simple cubic lattice $\mathbb{Z}^m$ in some cases. The generalized n-fold rotational symmetry ($C_n \subset D_n$) of $\mathcal{Q}$ will be a consequence of the exact n-fold point symmetry of $\mathcal{L}$. The dimension of $\mathbb{R}^m$ must be chosen large enough for $\mathcal{L}$ to be symmetric under the dihedral point group D_n. Also the representation of D_n should allow a 2D invariant subspace of $\mathbb{R}^m$. The smallest dimension m to fulfill these conditions is given by Euler's totient function $\phi(n)$, which counts the positive integers that are smaller than n and coprime with n. For the physically most interesting cases, this is $\phi(5) = \phi(8) = \phi(10) = \phi(12) = 4$.

Embedding $\mathcal{Q}$ in a hyperspace of dimension $m = \phi(n)$ is called minimal embedding. Often, this is not the most obvious choice and it can account for $\mathcal{L}$ deviating from $\mathbb{Z}^m$. The parallel space $E^{\parallel}$ will be a 2D invariant subspace of $\mathcal{H}$ with respect to D_n , while the complementary invariant subspace is the perpendicular space $E^{\perp}$. For a QC, and aperiodic CPS-crystals in general, $E^{\parallel}$ will always cut trough $\mathcal{H}$ such that it contains at most one hyperlattice point. If not explicitly stated differently, $E^{\parallel}$ will be assumed to contain the origin. As already in the 1D example, this ensures that the projection $\mathbf{P}^{\perp}$ is an isomorphism between $\mathcal{L}$ and $\mathbf{P}^{\perp}(\mathcal{L}) \equiv \mathcal{L}^{\perp}$. For the following section it will also be assumed that the projection $\mathbf{P}^{\parallel}$ is an isomorphism between $\mathcal{L}$ and $\mathbf{P}^{\parallel}(\mathcal{L}) \equiv \mathcal{L}^{\parallel}$. In the 1D example above, this is clearly given, since if the slope $s^{\parallel}$ of E is irrational, then so is the slope $s^{\perp} = 1/s^{\parallel}$ of $E^{\perp}$. This property follows easily for $\mathcal{L} = \mathbb{Z}^m$, but it also holds for the perhaps more complicated hyperlattices of other prominent QCs (Penrose tilings, Ammann-Beenker tiling, etc.). Combining $\mathbf{P}^{\perp}$ and $\mathbf{P}^{\parallel -1}$, we find that $\mathcal{L}^{\perp}$ and $\mathcal{L}^{\parallel}$ are isomorphic. Finally, one defines a window $\mathcal{W} \subset E^{\perp}$, and the quasicrystal is given by

$$\mathcal{Q} = \{v^{\parallel} | \boldsymbol{v} \in \mathcal{L} \wedge v^{\perp} \in \mathcal{W}\}, \tag{12}$$

where $v^{\parallel}$ and $v^{\perp}$ are analogous as in eq. (9), but now they have dimension 2 and $m-2$ respectively. Though the window should reflect the D_n-symmetry, its shape and size can still vary among different D_n-symmetric tilings, with or without MLD. Within the set of CPS-crystals, a tiling $\mathcal{T}_1$ is locally derivable from another tiling $\mathcal{T}_2$ if the window of $\mathcal{T}_1$ can be obtained from finitely many intersections, unions or complements of the window of $\mathcal{T}_2$ [43].

Let us again consider the rhombic PT, which can be constructed in several ways within the CPS. In deBrijun's original projection scheme the hyperlattice is $\mathcal{L} = \mathbb{Z}^5$. This method is well explained in [46] or [49]. The hyperspace $\mathbb{R}^5$ has two 2D and one 1D invariant subspaces with respect to the group D_{10}. Choosing one of the 2D subspaces as $E^{\parallel}$, the PT's lattice points are the $\mathbf{P}^{\parallel}$-projections of those $\mathcal{L}$-points whose Voronoi cell (5D-hypercube) intersect $E^{\parallel}$. As the PT's point lattice without edges is MLD with the rhombic PT [21](page 185), the tiles can be constructed from the point lattice simply by drawing an edge between all vertices of shortest distance. This is the 5D analog of the strip-construction of the Fibonacci chain above. In the same manner, tilings of other symmetries can be obtained.

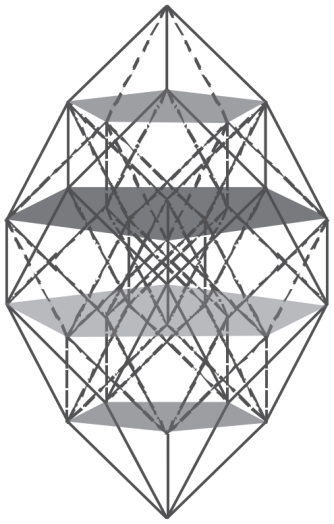

Figure 14: The window of the PT constructed from 5D hyperspace is a rhombic icosahedron. The fivefold symmetry axis is parallel to the subspace E^{Δ}, which cuts periodically through $\mathcal{L}$. $\mathbf{P}^{\perp}$-projections of the $\mathbb{Z}^5$-points lie all in the four shaded pentagons. [49]

Alternatively, the PT-tiles can be directly constructed as $\mathbf{P}^{\parallel}$ projections of the 2-boundaries (2D surfaces) of the hypercube. Those 2-boundaries are projected onto $E^{\parallel}$ for which the $\mathbf{P}^{\perp}$-projection of its *dual object* contains a certain fixed point $c \in E^{\perp}$ (in the 1D tiling it was $c = 0$). Here, 'dual' refers to the reciprocal lattice. The dual object of a 2-boundary of the 5D Voronoi cell will be a 3-boundary of the reciprocal lattice's Voronoi cell.

However, there is a subtlety here due to the non-minimal embedding. The perpendicular space has two D_{10}-invariant subspaces

$$E^{\perp} = \widehat{E}^{\perp} \oplus E^{\Delta}.$$

The 1D subspace E^{Δ} is spanned by the vector $\Delta = [1, 1, 1, 1, 1]$. So, projecting $\mathbb{Z}^5$ onto E^{Δ} gives a periodic 1D lattice $\mathcal{L}^{\Delta}$. The 2D subspace $\widehat{E}^{\perp}$ has irrational orientation, like $E^{\parallel}$. The window, being the projection of the 5D hypercube onto $E^{\perp}$, is a rhombic icosahedron (fig. 14). It is not exactly symmetric under D_{10}. Still, the tiling has generalized D_{10}-symmetry as will be explained in the next section. All $\mathcal{L}^{\perp}$-points in $\mathcal{W}$ sit on the pentagonal slices, which are arranged along the $\mathcal{L}^{\Delta}$-points. While shifting the window within $\widehat{E}^{\perp}$ does not change the LI-class of the constructed tiling, shifting along E^{Δ} creates a continuum of different LI-classes, which are called the generalized Penrose tilings. This shifting of the window can equivalently be interpreted as moving the point c in $E^{\perp}$, or moving the strip in $E^{\perp}$. The original PT from section 2.2.1 emerges if the bottom point of the window has zero E^{Δ}-component, i.e. if $\Delta \cdot c = 0$, i.e. if $E^{\parallel} \cap E^{\Delta} = \{0\}$. For a nice, interactive visualization of how shifting the coordinate system changes the LI-class, see [51]. Still, all the different LI-classes have generalized D_{10} symmetry and even have the same diffraction pattern as long as the orientation of $E^{\parallel}$ is not changed [49].

Another way to construct the PT as a CPS-tiling was found by Baake et al., where the choice $\dim(\mathcal{H}) = 4$ omits any ambiguities. Instead of one 3D window with pentagonal slices, they just use four windows (the pentagons from figure 14) simultaneously, each PT-lattice point belonging to one window (figure 15). See [11] or [50] for a detailed

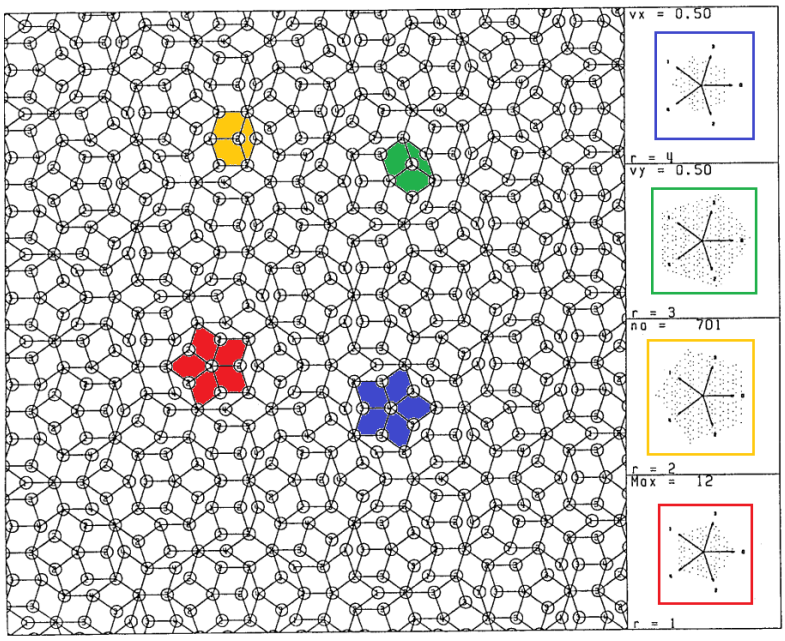

Figure 15: A patch of the PT from [50]. Each vertex has an index indicating its window (pentagon). The coloring shows an example of how two congruent vertices, twisted relative to each other by $\frac{2\pi}{10}$, belong to rotated windows. Both orientations of the pentagons are necessary for the full D_{10}-symmetry.

explanation of this method. A very similar approach will also be used to construct the Tübingen triangle tiling, on which this work is mainly focused. Therefore, it shall be explained later in more detail.

Apart from QCs the general mechanism described above can of course also create aperiodic crystals without point symmetry. These correspond to planes $E^{\parallel}$ with irrational orientation in $\mathcal{L}$ (meaning $\mathcal{L}^{\perp} \simeq \mathcal{L}^{\parallel}$), but which are not invariant subspaces with respect to the point symmetry of $\mathcal{L}$. Similarly allowing $E^{\parallel}$ to contain more than one $\mathcal{L}$-point gives access to an infinite variety of periodic crystals. These can have arbitrarily large unit cells, thereby approaching aperiodic structures with unbounded precision. Again, see [51] for a playful visualisation.

The argumentation in the following section will hold for all kinds of aperiodic CPS-crystals.

2.2.5 The Polar Calculus for Aperiodic Crystals

For anyone familiar with the Fibonacci sequence it will not be surprising that the ratio of the number of L-tiles over the number of S-tiles approaches τ when applying the SR to infinity. Writing these tile-numbers at the ith iteration like

$$\#S_i = \#L_{i-1} \tag{13}$$
$$\#L_i = \#L_{i-1} + \#S_{i-1} = \#L_{i-1} + \#L_{i-2}, \tag{14}$$

they are exactly the $i-1$th and ith Fibonacci numbers. This ratio of tile-numbers can also be calculated for a general aperiodic CPS-crystal using the height representation.

Consider the strip-method in figure 12. All the L-tiles correspond to a step $(1,0)$ in x-direction. Due to the specific definition of $\mathcal{W}$, such a step is only possible within the strip if it starts from a $\mathbb{Z}^2$-point above the $E^{\parallel}$-line. Likewise, all the S-tiles correspond to a y-step starting from a $\mathbb{Z}^2$-point below $E^{\parallel}$. The strip contains infinitely many $\mathbb{Z}^2$-points. But since $\mathbf{P}^{\perp}|_{\mathbb{Z}^2}$ is bijective, no two such points have the same $E^{\perp}$-component. So $\mathbf{P}^{\perp}(\mathbb{Z}^2)$ is a countably infinite set. In fact, it even is dense in $\mathbb{R}$. This allows the following identification. The ratio of the number of $\mathbb{Z}^2$-points in the strip above $E^{\parallel}$ to those below $E^{\parallel}$ is equal to the ratio of the upper and lower area segments of $\mathcal{W}$. So it is

$$\frac{\#L}{\#S} = \frac{\cos\theta}{\sin\theta} = \cot\theta. \tag{15}$$

This argumentation is a special case of the *polar calculus* in 1D CPS-crystals. This method was first explained in [52] and allows to calculate the density of any vertex- or tile-arrangement in an aperiodic CPS-crystal. It shall now be explained for a general $d^{\parallel}$-dimensional aperiodic lattice $\mathcal{Q}$ that can be obtained using the CPS.

Consider a configuration of $\mathcal{Q}$-points $C_a = \{p_i^{\parallel} | i = 1, ..., k\}$. To define C_a, it is sufficient to know the difference vectors $d_{ij}^{\parallel} = p_i^{\parallel} - p_j^{\parallel}$ and just one actual position represented by the label a. The atomic surfaces attached to all the hyperlattice points $\boldsymbol{p}_i$ must intersect $E^{\parallel}$. Projecting on $E^{\perp}$ this condition reads

$$0 \in \bigcap_{p_i \in C_a} (p_i^{\perp} - \mathcal{W}) \equiv \overline{C_a}. \tag{16}$$

A difference vector $d_{ij}^{\parallel}$ of the C_a-points must not lie in $\mathcal{Q}$ itself, but since $d_{ij}^{\parallel} = \mathbf{P}^{\parallel}(\boldsymbol{p}_i - \boldsymbol{p}_j)$, it still corresponds to exactly one point in $\mathcal{L}$ and therefore to one point $d_{ij}^{\perp} \in \mathcal{L}^{\perp}$. Now consider all the configurations C at a different location but with the same structure as C_a. Their relative hyperlattice coordinates $\boldsymbol{d}_i$ must also be the same as for C_a. All the C-type configurations must then differ from each other only through one hyperlattice translation $\boldsymbol{t} \in \mathcal{L}$. So the set of all C configurations $\{C\}$ has a bijection ($\leftrightarrow$) to the set of all hyperlattice translations of one representative C_a-configuration that satisfy eq. (16)

$$\{C\} \leftrightarrow \{\boldsymbol{t} \in \mathcal{L} | 0 \in t^{\perp} + \overline{C_a}\}. \tag{17}$$

The $t^{\perp}$-vectors of this set are exactly those which lie inside $\overline{C}_a$. They are defined by the set $\mathcal{L}^{\perp} \cap \overline{C}_a$. It is densely filling the area $|\overline{C}_a| \subset E^{\perp}$ because $\mathcal{L}^{\perp}$ is dense in $E^{\perp}$. The latter will be shown at the end of this section. With the density condition, the final statement of the polar calculus can be formulated

$$\rho_C = \frac{|\mathcal{L}^{\perp} \cap \overline{C_a}|}{|\mathcal{L}^{\perp} \cap \mathcal{W}|} = \frac{|\overline{C_a}|}{|\mathcal{W}|}. \tag{18}$$

Comparing the number of points representing a C-configuration to the total number of $\mathcal{Q}$-points is equivalent to comparing the area $|\overline{C_a}|$ to the total area $|\mathcal{W}|$. ρ_C is the density of C configurations. $\overline{C_a} \subset \mathcal{W}$ is called the *acceptance domain* (AD) of C configurations. Every $\mathcal{L}^{\perp}$-point that lies within this region corresponds to a $\mathcal{Q}$-point that is part of a C configuration.

The polar calculus also gives a better understanding of how the generalized point symmetry is inherited from $\mathcal{L}$ to $\mathcal{Q}$. Given again some point configuration C_a, consider the transformed configuration $C_a' = D^{\parallel}(g)C_a = \{D^{\parallel}(g)p^{\parallel} | p^{\parallel} \in C_a\}$. $D^{\parallel}(g)$ is a representation on $E^{\parallel}$ and $g \in \mathcal{G}$ is a point symmetry operation of the hyperlattice $\mathcal{L}$. Since $E^{\parallel}$ is

an invariant subspace of $\mathcal{H}$, the symmetry operation can equivalently be performed on the corresponding hyperlattice point.

$$D^{\parallel}(g)p^{\parallel} = \mathbf{P}^{\parallel}(\mathbf{D}(g)\boldsymbol{p}),$$

with $\mathbf{D}(g)$ the representation of $g \in \mathcal{G}$ on $\mathcal{H}$. Clearly $\mathbf{D}(g)\boldsymbol{p} \in \mathcal{L}$. So the transformed configuration C'_a also corresponds to a specific set of $\mathcal{L}$-points. Using the fact that $E^{\perp}$ is also an invariant subspace, we calculate the density of the transformed configuration using eq. (18)

$$\rho_{C'} = \frac{|\overline{C_a}'|}{|\mathcal{W}|} = \frac{|\bigcap_i \left(\mathbf{P}^{\perp}(\mathbf{D}(g)\boldsymbol{p}_i) - \mathcal{W}\right)|}{|\mathcal{W}|} = \frac{|D^{\perp}(g)\bigcap_i(p_i^{\perp} - \mathcal{W})|}{|\mathcal{W}|} = \frac{|\overline{C_a}|}{|\mathcal{W}|} = \rho_C. \quad (19)$$

The third equality is trivial if $\mathcal{W}$ is symmetric under $\mathcal{G}$. The situation is less obvious for the example of the PT constructed from $\mathbb{Z}^5$, where the window, the rhombic icosahedron, appears to be asymmetric under $\mathcal{G} = D_{10}$. But it turns out that the representation of D_{10} on $E^{\perp} = \widehat{E}^{\perp} \oplus E^{\Delta}$ leaves the window invariant. Any D_{10}-operation that would break the windows D_5 symmetry in $\widehat{E}^{\perp}$, like a rotation $2\pi n/10$ with odd n around the fivefold symmetry axis, is represented in E^{Δ} by a reflection along the fivefold symmetry axis [2]. It is easy to see from fig. 14 that such combined operations leave the rhombic icosahedron invariant. So the transformation of $\mathcal{W}$ by $D^{\perp}(g)$ is legitimate. Finally, rotating or reflecting the whole volume $\overline{C}_a$ does again not change its measure, hence the transformed configuration has the same density as the original one.

To better understand why the polar calculus allows truly exact calculations in an aperiodic crystal the following explanation of $\mathcal{L}^{\perp}$ being dense in $E^{\perp}$ may be helpful. Let us write an arbitrary $\mathcal{L}$-vector $\boldsymbol{q}$ in the lattice basis $\{\boldsymbol{v}_i\}$ with integer coefficients h_i and in the basis $\{\mathbf{k}_i^{\parallel}\} \cup \{\mathbf{k}_i^{\perp}\}$ of parallel and perpendicular space, where a matrix with elements $M_{ij}^{\parallel}$ and $M_{ij}^{\perp}$ describes the basis transformation

$$\boldsymbol{q} = \sum_{i=1}^{m} h_i \boldsymbol{v}_i = \sum_{ij} h_i M_{ij}^{\parallel} \boldsymbol{k}_j^{\parallel} + \sum_{ij} h_i M_{ij}^{\perp} \boldsymbol{k}_j^{\perp}. \quad (20)$$

Here we assume minimal embedding, meaning that all $\boldsymbol{q} \neq \mathbf{0}$ have nonzero $E^{\parallel}$- and $E^{\perp}$-components. Otherwise, only a subspace of $E^{\perp}$ will be filled densely as in the case of the $\mathbb{Z}^5$-window for the PT. The summation on the right of eq. (20) is the $E^{\perp}$-part of $\boldsymbol{q}$. It can only vanish for $h_i = 0\ \forall i \in \{1, .., m\}$. Any other choice of $\{h_i\}$ with $q^{\perp} = 0$ would mean $\boldsymbol{q} \neq \mathbf{0}$ and $\boldsymbol{q} \in \ \mathrm{span}(\{\mathbf{k}_i^{\parallel}\}) \simeq E^{\parallel}$. Which is impossible as for an aperiodic crystal $\mathbf{0}$ is the only $\mathcal{L}$-point to be contained in $E^{\parallel}$. Lets rewrite the case of $q^{\perp} = 0$

$$\sum_{ij} h_i M_{ij}^{\perp} \mathbf{k}_j^{\perp} = 0 \Leftrightarrow \sum_j \Big(\sum_i h_i M_{ij}^{\perp} \Big)^2 = 0 \Leftrightarrow \sum_i h_i M_{ij}^{\perp} = 0\ \ \forall j \in \{1, .., d^{\perp}\}. \quad (21)$$

Looking at the sum on the right in eq. (21), assume one ratio of matrix elements $\frac{M_{kj}^{\perp}}{M_{lj}^{\perp}}$ was a rational number $\frac{a}{b}$ with $0 \neq a, b \in \mathbb{Z}$. Then choosing $h_k = b$, $h_l = -a$ and other $h_i = 0$ would also let the sum vanish. Since we just argued that this is impossible with any nonzero h_i, the assumption of $\frac{M_{kj}^{\perp}}{M_{lj}^{\perp}}$ being rational must be wrong for all $k \neq l$. This is

[2] This will be derived in section 3.1.1. There, all irreducible representations of D_{10} are listed.

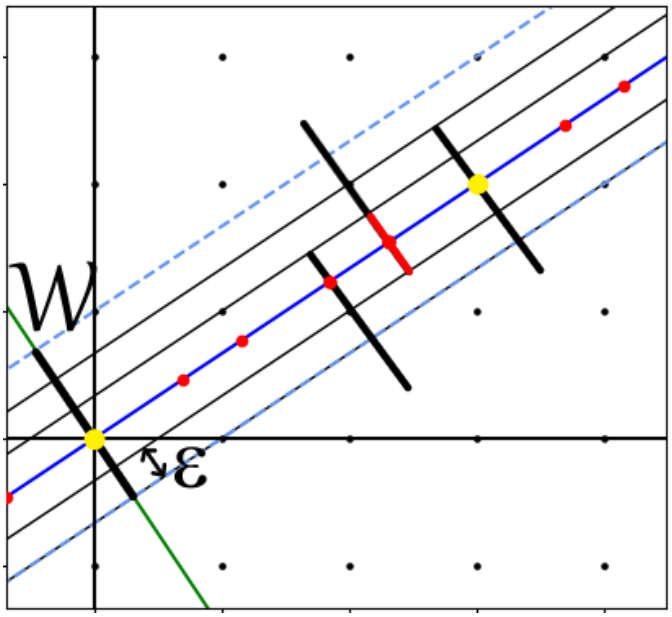

Figure 16: A periodic 1D-crystal constructed from a 2D CPS. The slope of $E^{\parallel}$ (blue line) is 2/3. The unit cell $\mathcal{U}$, marked by yellow dots, contains 5 points, corresponding to 5 equidistant lines, parallel to $E^{\parallel}$. The configuration of 3 points with distances S, L occurs twice in $\mathcal{U}$. This can be calculated by counting the $\mathcal{L}^{\perp}$-points that lie in the intersection of the atomic surfaces of an $S-L$-configuration (red line). Recall that $\mathcal{W}$ is half open.

what the expression 'irrational orientation' really means. Next, WLOG again let $h_i = 0$ for $i \neq k, l$ and write

$$\sum_i h_i M^{\perp}_{ij} \propto \alpha h_k + h_l, \tag{22}$$

where now $\alpha = \frac{M^{\perp}_{kj}}{M^{\perp}_{lj}}$ must be irrational. Then Kronecker's approximation theorem can be used [53], which states that

$$\text{the set } \{n\alpha - \lfloor n\alpha \rfloor | n \in \mathbb{Z}\} \text{ is dense in } [0,1] \text{ for irrational } \alpha. \tag{23}$$

Setting $h_l = -\lfloor \alpha h_k \rfloor + c$ where $c \in \mathbb{Z}$ is free, it is clear that the numbers in eq. (22) are dense in $\mathbb{R}$. As the above argumentation holds simultaneously for all directions $j \in \{1, .., d^{\perp}\}$ we conclude that $\{\sum_{ij} h_i M^{\perp}_{ij} \boldsymbol{k}^{\perp}_j | h_i \in \mathbb{Z}\} \simeq \mathcal{L}^{\perp}$ is dense in $E^{\perp}$.

2.2.6 The Polar Calculus for Periodic Crystals

The prominent role of Kronecker's theorem in the argumentation above suggests that the irrational orientation of E and therefore the aperiodicity of $\mathcal{Q}$ is a necessary condition for the polar calculus. And indeed, in general the polar calculus (eq. (18)) does not hold for periodic CPS-crystals. However, there are exceptions.

Let us revisit the special 1D CPS of the previous section and see why there, the polar calculus actually works also for all periodic crystals. First, note that for periodic crystals, the isomorphism between $\mathcal{L}^{\parallel}$ and $\mathcal{L}^{\perp}$ is lost as well as the bijection between $\mathcal{Q}$

and $\mathcal{L}^\perp \cap \mathcal{W}$. But a periodic crystal will have a finite unit cell $\mathcal{U} \subset \mathcal{Q}$ that contains all the information about the crystal structure. The $\mathcal{L}^\parallel$-points in this unit cell still have the same one-to-one relation to the $\mathcal{L}^\perp$-points in $\mathcal{W}$ as in the aperiodic case. Only outside of $\mathcal{U}$ the mapping $\mathcal{Q} \to \mathcal{L}^\perp \cap \mathcal{W}$ is no longer injective. In this sense an aperiodic CPS-crystal is the limit of a periodic crystal with an infinite unit cell.
Fig. 16 shows a periodic 1D crystal. The slope of the parallel space in this example is $m^\parallel = a/b = 2/3$. This picture should help to understand the following argumentation. The window is still defined as in eq. (7). It has length $|\mathcal{W}| = \cos\theta + \sin\theta = \frac{a+b}{\sqrt{a^2+b^2}}$. Points $\boldsymbol{p} = (x, y)$ of $\mathbb{Z}^2$ have a perpendicular component $\mathbf{P}^\perp \boldsymbol{p} = y\cos\theta - x\sin\theta = \frac{yb-xa}{\sqrt{a^2+b^2}}$. They form the periodic $\mathcal{L}^\perp$-lattice with lattice constant $\varepsilon = \frac{1}{\sqrt{a^2+b^2}}$. Then, the following proportionality will be very useful

$$|\mathcal{W}| = (a+b)\varepsilon. \tag{24}$$

Now again assume an arbitrary configuration $C_z = \{p_i^\parallel, i = 1, .., k\}$ of k points in $\mathcal{Q}$. The distances $d_i^\parallel = p_i^\parallel - z^\parallel$ with respect to an arbitrary but fixed point $z^\parallel \in C_z$ are of the form $d_i^\parallel = \alpha S + \beta L$, $\alpha, \beta \in \mathbb{Z}$. The elementary steps S and L in $E^\parallel$ correspond to steps $-a\varepsilon$ and $+b\varepsilon$ in $E^\perp$ respectively. Therefore, we write

$$d_i^\perp = (-a\alpha + b\beta)\varepsilon = n_i\varepsilon, \qquad n_i \in \mathbb{Z} \qquad \forall i = 1, .., k.$$

The only further condition is that all the points $p_i^\perp$ corresponding to points $p_i^\parallel \in C_z$ lie within the window. To find the number $\#C$ of C-type configurations (translations of C_z) in the unit cell, we ask how many points $\widetilde{z}^\parallel \in \mathcal{U}$ have k neighbours with distances $\{d_i^\parallel; i = 1, .., k\}$. This question can be formulated equivalently in perpendicular space: How many $\widetilde{z}^\perp \in \mathcal{L}^\perp$ are there such that $(\widetilde{z}^\perp + n_i\varepsilon) \in \mathcal{W}\ \forall i = 1, .., k$?

Translating to the atomic-surface-formulation, this reads:
How many points $\widetilde{z}^\perp \in \mathcal{L}^\perp$ are there such that $0 \in (\widetilde{z}^\perp + n_i\varepsilon - \mathcal{W})\ \forall i = 1, .., k$?

This is just the number of $\mathcal{L}^\perp$-points in the set

$$\bigcap_i (n_i\varepsilon - \mathcal{W}) \equiv \overline{C_z}. \tag{25}$$

The index 'z' in eq. (25) just notes that this set is constructed from one example of a C-type configuration. Because the shifting distance between the intersecting windows and the lengths of the windows are all integer multiples of ε, the area $|\overline{C}_z|$ is also always an integer multiple of ε. Since also the $\mathcal{L}^\perp$-points have a minimal distance ε, we can calculate the density of C-configurations in $\mathcal{Q}$ as

$$\rho_C = \frac{\#C}{\#\mathcal{U}} = \frac{|\mathcal{L}^\perp \cap \overline{C}_z|}{|\mathcal{L}^\perp \cap \mathcal{W}|} = \frac{|\overline{C}_z|/\varepsilon}{|\mathcal{W}|/\varepsilon}. \tag{26}$$

The ε in the right expression cancel and the statement is the same as the polar calculus of eq. (18). In this particular example of periodic CPS-crystals, the polar calculus works because the window length is exactly an integer multiple of the $\mathcal{L}^\perp$-lattice-parameter ε. In principle, this trick can also be applied in higher dimensions. It becomes more complicated though, because not only the size of the window but also its shape must be in accordance with the $\mathcal{L}^\perp$-lattice. This won't be the case for the periodic 2D crystals in this thesis. But for most of them the crucial third equality in eq. (26) is a good approximation for their true configuration densities.

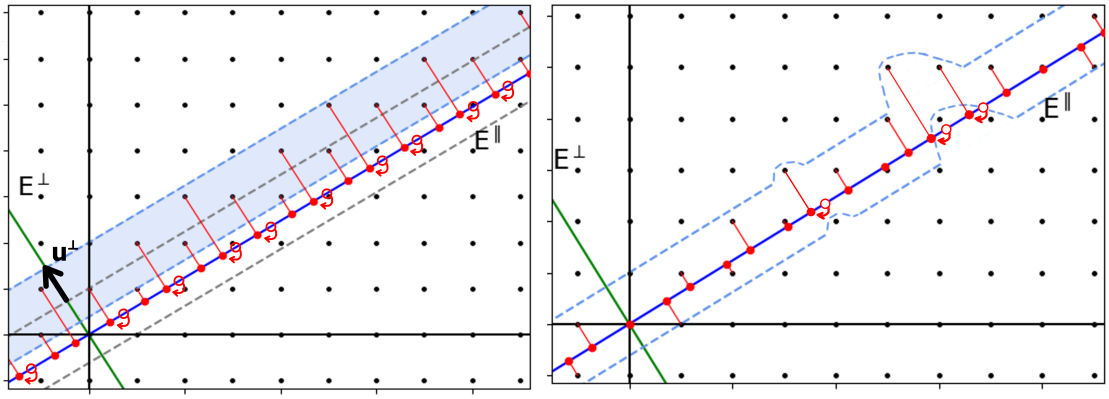

(a) Homogeneous phasonic displacement in the Fibonacci chain QC. The tiling before and after the shift $u^\perp$ are in the same LI-class and are related through a precise sequence of infinitely many phasonic flips (marked by red arrows).

(b) Three phasonic flips in the Fibonacci chain. Each flip changes a tile sequence LS to SL. In the CPS, this can be represented by projecting the point $P+(-1,1)$ instead of P, which is shown by deforming the strip around P. The two flips on the right are correlated, meaning only if the right most point flips first its neighbour can also flip.

Figure 17

2.3 Phasonic Displacement and Flips

As mentioned in chapter 2.2.3 and 2.2.4, shifting the projection-strip, or equivalently the hyperlattice $\mathcal{L}$, in $E^\perp$-direction does not change the LI-class of the CPS-tiling. The same holds for a constant shift in $E^\parallel$-direction. This is clear as the polar calculus formalism for an arbitrary atom configuration C works independently of the actual location of C in $\mathcal{H}$, meaning that the densities of all possible atom configurations are invariant under translations in $\mathcal{H}$.

While a shift $u^\parallel$ of $\mathcal{L}$ along $E^\parallel$ causes simply a translation of the CPS-crystal $\mathcal{Q}$, the effects of a shift $u^\perp$ along $E^\perp$ are less trivial. Shifting the strip in $E^\perp$-direction, $\mathcal{L}$-points that used to lie close to one boundary will drop out of the strip and won't be projected anymore. At the opposite boundary the strip will include new $\mathcal{L}$-points. Considering an aperiodic CPS-crystal, then due to the density of $\mathcal{L}^\perp$ in $E^\perp$ any displacement $u^\perp \in E^\perp$ will cause infinitely many old $\mathcal{L}$-points to drop out and new $\mathcal{L}$-points to be included into the strip. It also follows from the strips irrational orientation that the atoms which are newly projected into $E^\parallel$ will have different positions as those that dropped out. From the $\mathcal{Q}$-point of view the displacement $u^\perp$ of the strip causes infinitely many local changes in the crystal structure. However complicated these restructurings may be, they will always preserve the set of possible relative coordinates between atoms (hence the prototiles in the corresponding tiling), as this is a property of the LI-class.

Consider for example a small shift $0 < u^\perp < |\mathcal{W}|$ in the 1D Fibonacci chain as in fig. 17a. The set of lost atoms and the set of newly added atoms can be nicely combined into one set of pairs of one lost and one new atom. Recall that the strip in this example is just wide enough to contain one full square of $\mathcal{L}$-points. So, wherever an $\mathcal{L}$-point P drops out of the strip a new $\mathcal{L}$-point with coordinates $(-1,1)$ relative to P will be included.

In $\mathcal{Q}$ this exchange of two $\mathcal{L}$-points looks, as if the old atom instantly jumps a distance $L - S$ to the left. For a small displacement $0 < u^\perp < |\mathcal{W}|$, all the local restructurings are 'atom-jumps' of this kind. An arbitrarily large displacement $u^\perp > |\mathcal{W}|$ can be decomposed into a sequence of consecutive small displacements, each causing only simple atom jumps. Then, the complicated structural rearrangements caused by any larger $E^\perp$-displacement must be just sequences of these elementary atom jumps.

These jumps are usually called *phasonic flips* (or just *flips*) and the coordinate shift in $E^\perp$-space is called *phasonic displacement* (noted $u^\perp$) in contrast to the conventional shift in $E^\parallel$-space that is called *phononic displacement* ($u^\parallel$). Phasonic displacement and flips are also an important feature of 2D and 3D quasicrystals and have been investigated in theoretical [54, 55] and experimental physics [56, 57, 58]. The term 'phasonic' might not be self-explanatory. In Appendix A, it is motivated how a displacement in perpendicular space is related to the phase of a wave.

Instead of considering flips as a consequence of a phasonic displacement, one could also see it the other way around. Roughly speaking, the flips happen first and thereby cause an adjustment of the phasonic displacement, which works as a tool to categorize the flip-sequence. This is a more realistic point of view as atom flips are real excitations in a physical crystal, while the hyperspace and the CPS are idealized and purely mathematical concepts. The flips that would be necessary for an aperiodic tiling to transition to a different tiling of the same LI-class (as in fig. 17a) are extremely specific and correlated throughout the whole crystal. Here, *correlated* means that whether or not a certain particle is being flipped depends on whether other particles are being flipped. In his dissertation, [48] Koschella has computed these flips corresponding to a homogeneous phasonic displacement in the example of the 2D Mikulla-Roth-Tiling.

If instead arbitrary numbers and combinations of flips were allowed, the quasicrystal would certainly not be characterized by a single LI-class and the phasonic displacement $u^\perp(x^\parallel)$ would strongly depend on the position in physical space. In fig. 17b, a simple example of few elementary flips in the Fibonacci chain is shown. For each such isolated flip the strip would have to be deformed only around the flipping site $x_f^\parallel$ with a displacement $u^\perp(x_f^\parallel) \leq |\mathcal{W}|$.

2.4 Phasonic Strain and Approximants

The *phasonic strain* is defined as the derivative of the phasonic displacement with respect to the parallel space coordinates. In a general CPS with dimensions $d^\parallel$ and $d^\perp$ for $E^\parallel$ and $E^\perp$ this will be a $(d^\perp \times d^\parallel)$-matrix denoted $\boldsymbol{\chi}$

$$\chi_{ij} = \frac{\partial u_i^\perp}{\partial x_j^\parallel}. \tag{27}$$

It was mentioned before that having $u^\perp$ depend on $x^\parallel$ (meaning $\boldsymbol{\chi} \neq \mathbf{0}$) makes sense if we want to describe flip-processes that do not preserve the LI-class. Having the phasonic displacement also depend on the positions in $E^\perp$-space is not desirable, as varying $x^\perp$ preserves the LI-class and physical properties (like the flip-processes that are measured by $u^\perp$) should be invariant within the LI-class.

A straightforward and elegant way of varying the LI-class is to apply a constant phasonic strain. The phasonic strain $\boldsymbol{\chi}$ is always applied with respect to some reference LI-class (usually the ideal QC) that is then labeled by $\boldsymbol{\chi} = \mathbf{0}$. Given a hyperlattice $\mathcal{L}$ and a

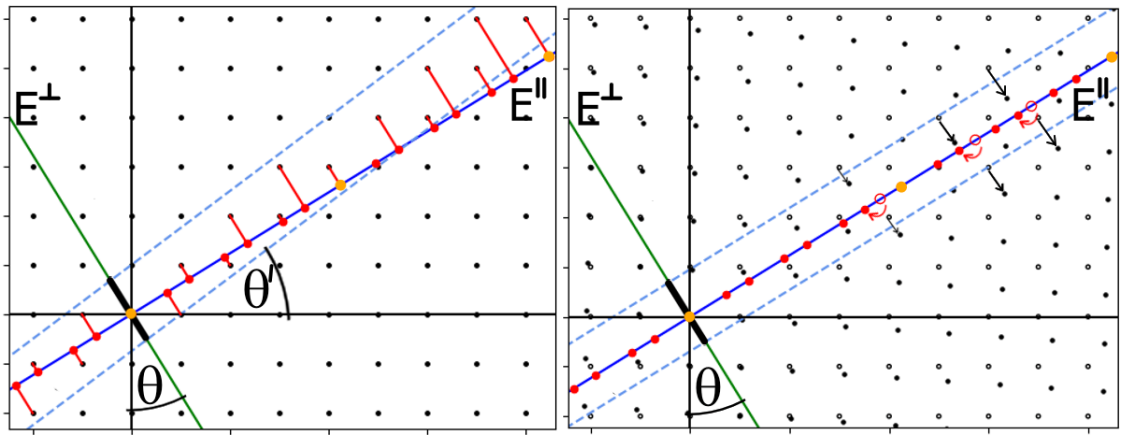

(a) One way to see constant phasonic strain is by tilting the strip. Here, the new angle $\theta' = \arctan(3/4)$ creates an approximant of the Fibonacci chain. The tile size does not change as the projection $\mathbf{P}^{\parallel}$ is still defined by $\theta = \arctan(1/\tau)$.

(b) The same approximant as on the left is created by phasonic deformation of the hyperlattice $\mathcal{L}$ (old points are empty circles). The window must adapt its shape to the new lattice. Flips are induced where $\mathcal{L}$-points enter and exit the strip.

Figure 18

window $\mathcal{W}$, this reference LI-class is fully defined by the orientation of $E^{\parallel}$ in $\mathcal{H}$ and the strip being parallel to $E^{\parallel}$. A constant phasonic strain changes the orientation of the strip $\mathcal{S}$ in $\mathcal{H}$, while leaving the orientation of $E^{\parallel}$ fixed.

As always, it is helpful to consider this concept in the simple 1D case (fig. 18a). There the orientation of $E^{\parallel}$ is defined by an angle $\theta = \arctan(1/\tau)$. We define a new projection operator $\mathbf{P}^{\perp\prime}$ as the $E^{\perp}$-projection parallel to a line $E^{\parallel\prime}$ that is a rotation of $E^{\parallel}$ by $\theta' - \theta$. Then, the window $\mathcal{W}$ is constructed as the $\mathbf{P}^{\perp\prime}$-projection of the unit square and the strip as the translations of the window along $E^{\parallel\prime}$. This changes not only the strips orientation, but also the size and shape of $\mathcal{W}$. The latter is important to ensure that the number of prototiles (2 in fig. 18a) is fixed for all LI-classes reached by this method. The final projection of the $\mathcal{L}$-points in the strip is aimed onto the $E^{\parallel}$-space of fixed angle θ that represents the $\boldsymbol{\chi} = \mathbf{0}$ LI-class. This makes sure that also the shape and size of prototiles is fixed (e.g. $\cos(\theta)$ and $\sin(\theta)$).

In section 2.2.3, it was mentioned that choosing the slope $\tan(\theta)$ in a 1D CPS rational will produce a periodic crystal. The same holds if $\tan(\theta')$ in a phasonically deformed CPS as above is rational, only that now the tile shapes are independent of θ'. Such periodic crystals will have larger and larger unit cells, approximating the true quasicrystal ($\boldsymbol{\chi} = \mathbf{0}$) better and better as $\theta' \to \theta$. They are called *Approximants* of this quasicrystal.

Instead of changing the direction of the projection operator $\boldsymbol{P}^{\perp\prime}$ in a fixed hyperlattice $\mathcal{L}$, one could also deform $\mathcal{L}$ while leaving the strips orientation fixed. Only the shape of $\mathcal{W}$ must be adapted to the $\mathcal{L}$-points of the new, deformed unit cube. The linear transformation of an $\mathcal{L}$-point $\boldsymbol{x}$ is directly given by the matrix $\boldsymbol{\chi}$ from eq. 27

$$\boldsymbol{x} = \begin{bmatrix} x^{\parallel} \\ x^{\perp} \end{bmatrix} \mapsto \boldsymbol{x}' = \begin{bmatrix} x^{\parallel} \\ x^{\perp} + \boldsymbol{\chi} x^{\parallel} \end{bmatrix}. \tag{28}$$

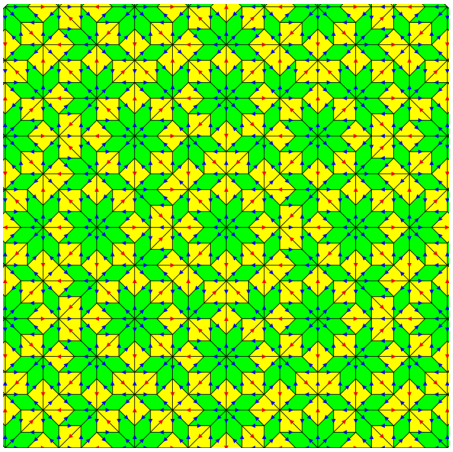

(a) Patch of the ideal Ammann-Beenker tiling. The arrow markers on the tiles are not sufficient for perfect matching rules, but they are used in the substitution rule, which is also why the squares are divided into triangles. [59]

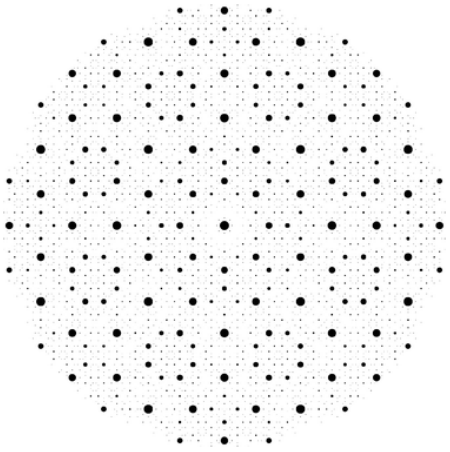

(b) Diffraction pattern of the Ammann-Beenker tiling with 8-fold rotational symmetry. [60]

Figure 19

Figure 20: The elementary flip ('Simpleton') of the Ammann-Beenker tiling, or any square-rhombus tiling. Only one point in the center of the hexagon flips. (page 474 in [21])

This process is shown in fig. 18b, analogous to the 1D example described above. In the 1D case, the one-to-one correspondence between the two methods is given by the relation

$$\chi = -\tan\big(\theta' - \theta\big). \tag{29}$$

The projection operator $\mathbf{P}^{\perp\prime}$ from the above description can be written in terms of $\boldsymbol{\chi}$ like

$$\mathbf{P}^{\perp\prime} = \mathbf{P}^{\perp} + \boldsymbol{\chi}\mathbf{P}^{\parallel}. \tag{30}$$

While the picture of tilting the strip might be visually helpful to understand the consequences of constant phasonic strain, the method of deforming $\mathcal{L}$ and adapting $\mathcal{W}$ seems mathematically more straightforward. It is how phasonic strain will be used later.

2.5 Thermodynamic Stability and Random Tilings

Why do certain materials form into a stable structure with quasiperiodic symmetry? In canonical thermodynamics, the question of stability, meaning thermodynamic equilibrium, comes down to optimizing two quantities: The *internal energy* (or average energy)

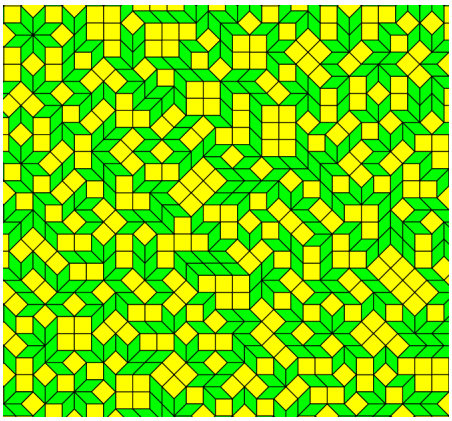

(a) A randomized version of a square-rhombus tiling, that was constructed from the Ammann-Beenker tiling by repeatedly and randomly applying the simpleton flip. This tiling is not ordered but it still has statistical 8-fold rotational symmetry. ([59], or page 475 in [21])

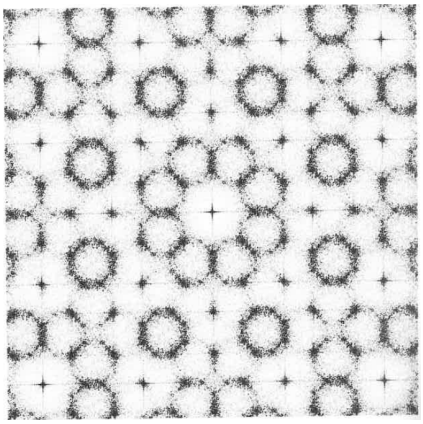

(b) Diffraction pattern of a finite patch of the randomized square-rhombus tiling. The pattern shows strong similarities with fig. 19b, although the peaks are not as sharp. The 8-fold symmetry is clearly visible. (page 476 in [21])

Figure 21

U and the *entropy* S. Roughly speaking, the internal energy tries to become as small as possible, while the entropy tries to be as large as possible. Since entropy is a measure for the variety and accessability of canonical microstates that a physical system can occupy, it can only contribute to the stability if transitions between different microstates are possible. As we assume that such transitions, in general, cost energy (e.g. different microstates are separated by a potential hill in phase space), the entropy contribution should vanish at zero temperature $T = 0$ [3]. Then the system would be in its *ground state* (or one of the ground states, if there is degeneracy), which is the state of lowest possible internal energy, the *ground state energy* $E_0 = U(T = 0)$. At higher temperatures, there will always be a non-vanishing probability for the system to explore the high energy microstates around the ground state, meaning the average energy cannot be E_0 anymore. The entropy reaches its maximum if all microstates, regardless of their potential energy, are occupied with the same probability. This is the case either, if the states are all energetically degenerate, or if the system has infinite temperature. So the two conditions of minimizing U and maximizing S are, in general, not simultaneously satisfied. The quantity called the *Helmholz free energy* F combines these two mechanisms, where the entropy is weighted by temperature T

$$F = U - TS. \tag{31}$$

Then for an arbitrary temperature a physical system (e.g. a structure of atoms) is in thermal equilibrium, iff its free energy is minimal. In general both U and S will depend on the materials temperature T and various other parameters, like interaction strength between particles, atom masses, charge, relative spin orientation, etc.

[3] The entropy itself must not vanish. A system with n ground states will still have an entropy $S = k_B \ln(n)$ at $T = 0$. But this won't make it any more stable if it is fixed in one particular ground state.

There are now two possible scenarios of why a quasicrystal should be the thermal equilibrium phase of some material (e.g. some alloy). One is that the quasicrystalline structure is the ground state of the material and its interaction potential. It would then be an ideal tiling only at $T = 0$ and experience deviations as the temperature is increased. This is how the stability of conventional crystals is usually understood. There is research on interaction potentials that would support a perfect QC. One example of a potential stabilizing a binary tenfold QC was already mentioned at the end of section 2.2.2. In [61], Gähler and Jeong report the stabilization of the Ammann-Beenker tiling (ABT) (fig. 19a) as a ground state using a simple cluster interaction. Two kinds of clusters (patches), an octagon and a boat, were attributed negative energies with a specific ratio, while all other clusters were given zero energy. This is even more remarkable as the authors mention that the ABT does not allow perfect matching rules[4], which where previously assumed to resemble interaction potentials. However, here the challenge remains to find a microscopic particle potential, that supports this rather coarse grained type of interaction. An extensive mathematical argumentation was given by Burkov [62] about general symmetry conditions that any 2D QC ground state must necessarily fulfil.

The other scenario of quasicrystal stability is usually called *entropical stabilization*, which this thesis will focus on. The main aspect hereby is that quasicrystals must not be precisely ordered, like a single LI-class, to produce a symmetric diffraction pattern. Assuming the symmetry in the diffraction pattern resembles the generalized symmetry group of an atom lattice as described in section 2.2.1, this becomes very apparent. Take for example again the ABT, shown in fig. 19 together with its diffraction pattern. The elementary flip, also called *simpleton flip*, of the ABT is shown in fig. 20. Imagine all the possible flips, or finite sequences of flips, in the ideal ABT are performed with some probability that is independent of the flip's orientation. Then, on average, each orientation of every patch will be altered due to flips with the same probability. Hence also the densities of the altered patches will be the same for each orientation. So the new tiling will still have generalized 8-fold rotational symmetry, now also called *statistical symmetry*.

Such a process of randomly performing flips is called *randomization*. The emerging tiling is then called a randomized version of the ABT in this case, or simply a *random tiling* (RT). Note that the symmetry argument still works, even if the flips have different probabilities depending on their environment up to some radius, as long as they do not discriminate between different orientations. A randomized version of the ABT is seen in fig. 21 together with its numerically calculated diffraction image. The patch is much too small to see the statistical symmetry, but the diffraction pattern, which was of course computed from a much larger patch, clearly shows an 8-fold symmetry axis. The diffraction pattern is not as sharp as for the ideal ABT (fig. 19b), which has perfect Bragg peaks. According to [21](page 475) it is not fully understood whether the diffraction pattern of a truly infinite 2D RT would produce pure point diffraction, absolute continuous, or singular continuous diffraction, or some mixture of these. However, diffraction patterns measured in reality always have some blurriness due to diffuse scattering. So it might be difficult to experimentally distinguish a real, ideal QC from a real, randomized QC based only on their diffraction pattern.

The advantage of a RT QC over the deterministic, ideal QC is that it is part of a much larger ensemble of RTs all connected to each other via flips. This *random tiling en-*

[4]While the argumentation by Gähler and Jeong for missing arrow-type matching rules seems perfectly reasonable and is confirmed by Baake, Grimm and Moody in [59], the latter article also shows how to further modify the tiles by markers in the corners to establish perfect matching rules in the ABT.

semble certainly allows for a much larger entropy than a single LI-class. Instead of being ground states with minimal potential energy, some quasicrystals might actually be RTs, stabilized by a large entropy. This idea is known as the first *random tiling hypothesis*, originally formulated by Henley:

> *The entropy density $S(\overline{\boldsymbol{\chi}})$ has its maximum at $\overline{\boldsymbol{\chi}} = 0$.*
>
> Henley C. (1991) [5]

$\overline{\boldsymbol{\chi}}$ is the average, or *global phasonic strain* of a CPS crystal and the case $\boldsymbol{\chi} = 0$ is assumed to represent the most symmetric LI-class, which is the ideal QC.

Given a CPS model and thereby a set of prototiles, one can calculate the average phasonic strain of any tiling $\mathcal{T}$ built from these prototiles. Each point in $\mathcal{T}$ will be an element of the projected hyperlattice $\mathcal{L}^{\parallel}$. As $\mathcal{L}^{\parallel}$ is isomorphic to $\mathcal{L}$, one computes the hyperspace-coordinates of $\mathcal{T}$. These $\mathcal{L}$-points will roughly (perhaps very roughly) describe a 2D plane embedded in $\mathcal{H}$. Its average orientation can be found from a numerical fit. Comparing this orientation with the orientation of $E^{\parallel}$ the average phasonic strain is obtained [5].

Such a computation is useful if one is given a certain atom lattice from an experiment or a simulation. In this thesis we want to compute and compare the free energies of different tiling ensembles which are a priori defined through their global phason strain. The ensemble of tilings corresponding to a certain $\overline{\boldsymbol{\chi}}$ shall be understood as follows. Starting from one specific tiling with global phasonic strain $\overline{\boldsymbol{\chi}}$[6] , we consider all those tilings that can be reached from it through a distribution of flips such that the distance of correlated flips is limited by some finite number μ. Such an ensemble of tilings will be called a *global phasonic strain class*, short GPS-class, since the operation of transforming a tiling through a flip distribution defines an equivalence relation.

Two flips F_1, F_2 are correlated if they do not commute, meaning that flipping F_1 and then F_2 results in a different configuration than vice versa, or if one flip is only possible, provided that the other flipped before (compare fig. 18b). The restriction of bounded correlation distances should assure that this definition is consistent with the construction of $\overline{\boldsymbol{\chi}}$ as explained above. Such infinite flip sequences with the flips correlated infinitely far would also allow to change the global phasonic strain. Even though every finite arrangement of correlated flips cannot change the tile densities, which are fixed for a given $\overline{\boldsymbol{\chi}}$, infinitely correlated flip clusters could. Hence, in an infinite crystal we want to allow arbitrarily many, but not arbitrarily large correlated flip clusters. Then we would like to propose the following equivalence. Two tilings $\mathcal{T}_1$ and $\mathcal{T}_2$ have the same average phasonic strain if, and only if, they can be transformed into each other by a, possibly infinite, number of flips with bounded flip correlation distance. The statement that such a restricted flip distribution cannot change the global $\overline{\boldsymbol{\chi}}$ seems clear from the argument of fixed tile densities. More questionable is the idea that all tilings with the same $\overline{\boldsymbol{\chi}}$ can be transformed into each other by such a process. If not, then there would exist two disjoint GPS-classes for the same $\overline{\boldsymbol{\chi}}$. This could actually have physical consequences because these classes could have different free energies and switching between them could be seen as a phase transition. This seems very odd, as two different GPS-classes with common $\overline{\boldsymbol{\chi}}$ have the same symmetry properties, and $\overline{\boldsymbol{\chi}}$ was supposed to be the order parameter.

[5] In 1D $\overline{\chi}$ is just the slope of the cut space relative to $E^{\parallel}$ (compare fig. 22b). In general, one has to find $d^{\perp} \cdot d^{\parallel}$ relative slopes.

[6] For this representative tiling, we shall choose the one that is defined by a fully constant phasonic strain $\boldsymbol{\chi} = \overline{\boldsymbol{\chi}}$. The other tiling in its ensemble will have local $\boldsymbol{\chi}$-fluctuations.

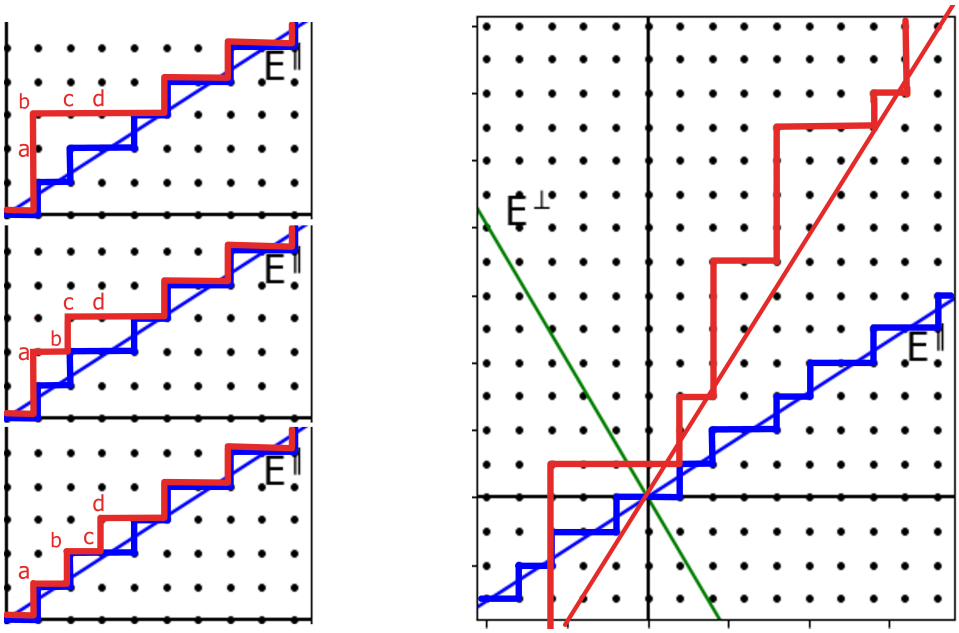

(a) Transforming the red staircase from above into the blue one. First only point b can flip. Then a and c, and lastly d. The largest correlation distance in this patch is between b and d, 2 steps in x-direction, so two L-steps in the projected tiling.

(b) The red and blue staircases have different average slopes. Trying to transform the red into the blue staircases, according to (a), one would create larger and larger vertical segments. As all points along one vertical segment are correlated, the correlation distance in the projected tiling becomes infinite.

Figure 22: Projecting the points form a 1D tiling with prototiles S and L into the hyperlattice creates a staircase. A flip SL $\mapsto$ LS in the tiling corresponds to replacing an up-right corner by a right-up-corner in the staircase. The average slope of the staircase fixes the density of vertical and horizontal steps. All finite deviations between two staircases can be repaired through finitely many flips (a).

For 1D CPS crystals, the proposal of equivalence between global phasonic strain and finitely correlated flip transformations is certainly true, and the idea is roughly explained in fig. 22. For tilings in a hyperspace of dimension 4 and larger, the problem seems more difficult and we do not know of any proofs, counter examples or other work about this question. However, in this thesis, we will consider explicitly only a small fraction of the range of tilings in a certain GPS-class. So the question, whether the GPS-class, as defined above, reaches truly all possible tilings with common $\overline{\chi}$ will not be a bother. Nevertheless, it is worth mentioning from a conceptual point of view.

Since this thesis won't mention local phason fluctuations much, but rather focuses on varying the global phason strain, we shall denote the latter by the symbol χ as long as confusion can be avoided.

Let us reformulate the random tiling hypothesis. It states that of all GPS-classes the entropy is largest in the most symmetric GPS-class, labeled by $\chi = 0$.

In the case of complete energetical degeneracy among the elements of each GPS-class, meaning no interaction between tiles, this seems very plausible. A system without any forces acting on it should tend towards the most isotropic, and thereby most symmetric, configuration. Using the grand canonical formalism and tile densities as variables, this idealized version of the random tiling hypothesis was proven rigorously in [8].

In reality though, this idealization probably does not apply. Even if the tiles arrange themselves in a symmetric way simply due to statistics, we are still left to explain how particles form into such tiles in the first place. This leaves again the question for a particle interaction potential. But now the search would be easier than for the QC-ground state hypothesis, since the potential must only stabilize few interatomic distances that make up the tiles. But then one should not exclude the possibility that such a potential will reach beyond the tile boundaries, causing non trivial interactions among tiles and thereby presumably inhomogeneous flip dynamics. The role that these consequences of realistic interaction potentials play in the entropical QC-stabilization will be investigated on the example of a model QC, while focusing on analytical, mathematical methods.

3 The Decagonal Model-Quasicrystal

3.1 The Tübingen Triangle Tiling

When one observes a QC in an experiment or a simulation, it is not obvious which tiling model represents the empirical data best. For the decagonal QC discovered by Engel in a molecular dynamics (MD) simulation, this became a bit easier, as it was built from only one type of particle, while real QCs so far have at least two components. Connecting all atoms of shortest distance, he found that most of the shapes created this way are tiles of the Tübingen triangle tiling (TTT). The latter, in its original form, consists of triangular tiles and was invented by Baake et al. [11] at the university of Tübingen, explaining the name. Its construction and properties shall be summarized in the following.

3.1.1 Construction of the TTT

The Tübingen triangle tiling is a decagonal mathematical quasicrystal. As mentioned in section 2.2.4, the minimal dimension of a hyperspace for a D_{10} symmetric tiling is $\dim\mathcal{H} = 4$. The 4D hyperlattice is not a square lattice though, but rather the root lattice $\mathbb{A}_4$ [7]. A background on the mathematics of root lattices is given in the original paper mentioned above. For now it is enough to know that $\mathbb{A}_4$ is a sublattice of the square lattice $\mathbb{Z}^5$ in 5D hyperspace. As the point group D_{10} is very naturally represented in $\mathbb{R}^5$, $\mathbb{A}_4$ is usually represented by 5D vectors. Similarly, the hyperspace $\mathcal{H}$ is the subspace of $\mathbb{R}^5$ that contains $\mathbb{A}_4$

$$\mathbb{A}_4 = \{\boldsymbol{x} \in \mathbb{Z}^5 | \boldsymbol{x} \perp \Delta\} \tag{32}$$

$$\mathcal{H} = \{\boldsymbol{x} \in \mathbb{R}^5 | \boldsymbol{x} \perp \Delta\}. \tag{33}$$

The vector $\Delta = [1, 1, 1, 1, 1]$ was already mentioned in the construction of the Penrose tiling from $\mathbb{Z}^5$. Actually, the PT and the TTT are closely related in their construction and symmetry (see [11], or [50]), but are not MLD.

Given the orthogonality condition in eq. (32), a straightforward basis of $\mathbb{A}_4$ and $\mathcal{H}$ is given by the vectors $\boldsymbol{a}_i = \boldsymbol{e}_i - \boldsymbol{e}_{(i+1)\mathrm{mod}5}$, where $\boldsymbol{e}_i$, $i \in \{0, 1, 2, 3, 4\}$ are the canonical basis vectors of $\mathbb{R}^5$

$$\boldsymbol{a}_0 = \begin{bmatrix} 1 \\ -1 \\ 0 \\ 0 \\ 0 \end{bmatrix}; \boldsymbol{a}_1 = \begin{bmatrix} 0 \\ 1 \\ -1 \\ 0 \\ 0 \end{bmatrix}; \boldsymbol{a}_2 = \begin{bmatrix} 0 \\ 0 \\ 1 \\ -1 \\ 0 \end{bmatrix}; \boldsymbol{a}_3 = \begin{bmatrix} 0 \\ 0 \\ 0 \\ 1 \\ -1 \end{bmatrix}; \boldsymbol{a}_4 = \begin{bmatrix} -1 \\ 0 \\ 0 \\ 0 \\ 1 \end{bmatrix}. \tag{34}$$

Next, the hyperspace is decomposed into its invariant subspaces with respect to the group $D_{10} = C_{10} \times C_2$. The group elements operate on $\mathbb{A}_4$ by permuting or inverting the basis vectors. The matrix representations $\mathcal{R}_5$ of the generators c_{10}, the rotation by $\frac{2\pi}{10}$, and c_2, the vertical reflection, are

[7] The square lattice $\mathbb{Z}^4$ has at most 8-fold rotational symmetry.

D_{10} (20)	e (1)	$c_{10}^{2j}c_2$ (5)	$c_{10}^{2j+1}c_2$ (5)	c_{10}^5 (1)	c_{10}, c_{10}^9 (2)	c_{10}^3, c_{10}^7 (2)	c_{10}^2, c_{10}^8 (2)	c_{10}^4, c_{10}^6 (2)
Γ_1	1	1	1	1	1	1	1	1
Γ_2	1	-1	-1	1	1	1	1	1
Γ_3	1	1	-1	-1	-1	-1	1	1
Γ_4	1	-1	1	-1	-1	-1	1	1
Γ_5	2	0	0	-2	τ	$-1/\tau$	$1/\tau$	$-\tau$
Γ_6	2	0	0	2	$1/\tau$	$-\tau$	$-\tau$	$1/\tau$
Γ_7	2	0	0	-2	$-1/\tau$	τ	$-\tau$	$1/\tau$
Γ_8	2	0	0	2	$-\tau$	$1/\tau$	$1/\tau$	$-\tau$
$\mathcal{R}_5$	5	-1	1	-5	0	0	0	0

Table 1: Characters of the irreducible representations of D_{10} and the reducible $\mathcal{R}_5$-representation. Γ_1-Γ_4 are scalars, Γ_5-Γ_8 are two dimensional.

$$\mathcal{R}_5(c_{10}) = \begin{bmatrix} 0 & 0 & -1 & 0 & 0 \\ 0 & 0 & 0 & -1 & 0 \\ 0 & 0 & 0 & 0 & -1 \\ -1 & 0 & 0 & 0 & 0 \\ 0 & -1 & 0 & 0 & 0 \end{bmatrix}, \quad \mathcal{R}_5(c_2) \begin{bmatrix} 0 & 0 & -1 & 0 & 0 \\ 0 & -1 & 0 & 0 & 0 \\ -1 & 0 & 0 & 0 & 0 \\ 0 & 0 & 0 & 0 & -1 \\ 0 & 0 & 0 & -1 & 0 \end{bmatrix}. \tag{35}$$

To find the invariant subspaces of $\mathcal{H}$ we must first find the irreducible representations of D_{10} that are contained in the reducible $\mathcal{R}_5$-representation. This was done by Koschella [48], but it shall be explained briefly to avoid possible confusion with later notation. Using the decomposition formula from group theory (see [25] for background), the multiplicities m_i of all 8 irreducible representations Γ_i in $\mathcal{R}_5$ are calculated

$$m_i = \frac{1}{20} \sum_{g \in D_{10}} \mathrm{Tr}(\mathcal{R}_5(g)) \, \mathrm{Tr}(\Gamma_i(g)). \tag{36}$$

The traces (or characters) of these representations are shown in table 1. As a result, we find the direct sum

$$\mathcal{R}_5 = \Gamma_5 \oplus \Gamma_7 \oplus \Gamma_4. \tag{37}$$

Since we know that the $4D$-subspace $\mathcal{H} \subset \mathbb{R}^5$ is D_{10}-invariant, the $1D$-subspace corresponding to the Γ_4-representation must be parallel to Δ. The generators of D_{10} in the two 2D representations are [8]

[8] In general $\Gamma_{4+n}(c_{10}) = \boldsymbol{R}(\pm n \cdot 2\pi/10)$ and $\Gamma_{4+n}(c_2) = \boldsymbol{R}(\varphi)\boldsymbol{\sigma}_y\boldsymbol{R}(-\varphi)$, where $\boldsymbol{R} \in SO(2)$ is a standard 2D rotation matrix. The parameter φ and the sense of rotation ($\pm$) define all equivalent representations for a given n.

$$\Gamma_5(c_{10}) = \begin{bmatrix} \cos(2\pi/10) & -\sin(2\pi/10) \\ \sin(2\pi/10) & \cos(2\pi/10) \end{bmatrix}, \quad \Gamma_7(c_{10}) = \begin{bmatrix} \cos(6\pi/10) & \sin(6\pi/10) \\ -\sin(6\pi/10) & \cos(6\pi/10) \end{bmatrix},$$
$$\Gamma_5(c_2) = \Gamma_7(c_2) = \begin{bmatrix} 1 & 0 \\ 0 & -1 \end{bmatrix} = \boldsymbol{\sigma}_y. \tag{38}$$

As the physical space $E^{\parallel}$, we choose the invariant subspace that transforms according to Γ_5, and as perpendicular space $E^{\perp}$ the one that is transformed by Γ_7.

Symmetry adapted orthonormal bases $\boldsymbol{b}_x^{\parallel}$, $\boldsymbol{b}_y^{\parallel}$ of $E^{\parallel}$ and $\boldsymbol{b}_x^{\perp}$, $\boldsymbol{b}_y^{\perp}$ of $E^{\perp}$ are given by

$$\begin{aligned} \boldsymbol{b}_x^{\parallel} &= \sqrt{\frac{1}{2\sqrt{5}\tau}} \begin{bmatrix} 1 \\ -1 \\ -\tau \\ 0 \\ \tau \end{bmatrix}, \boldsymbol{b}_y^{\parallel} = \sqrt{\frac{1}{10}} \begin{bmatrix} \tau \\ \tau \\ -1/\tau \\ -2 \\ -1/\tau \end{bmatrix} \\ \boldsymbol{b}_x^{\perp} &= \sqrt{\frac{1}{2\sqrt{5}\tau}} \begin{bmatrix} \tau \\ -\tau \\ 1 \\ 0 \\ -1 \end{bmatrix}, \boldsymbol{b}_y^{\perp} = \sqrt{\frac{1}{10}} \begin{bmatrix} 1/\tau \\ 1/\tau \\ -\tau \\ 2 \\ -\tau \end{bmatrix}. \end{aligned} \tag{39}$$

These vectors, together with the canonical bases $\{e_x^{\parallel}, e_y^{\parallel}\}$ on $E^{\parallel}$ and $\{e_x^{\perp}, e_y^{\perp}\}$ on $E^{\perp}$, define the projection operators

$$\begin{aligned} \mathbf{P}^{\parallel} &= e_x^{\parallel} \boldsymbol{b}_x^{\parallel t} + e_y^{\parallel} \boldsymbol{b}_y^{\parallel t} \\ \mathbf{P}^{\perp} &= e_x^{\perp} \boldsymbol{b}_x^{\perp t} + e_y^{\perp} \boldsymbol{b}_y^{\perp t}. \end{aligned} \tag{40}$$

The window $\mathcal{W}$ in the TTT is defined as the $\mathbf{P}^{\perp}$-projection of the $\mathbb{A}_4$-lattices' Voronoi cell $\mathcal{V}_{\mathbb{A}_4} = \mathcal{V}_{\mathbb{A}_4}(\mathbf{0})$ around the origin

$$\mathcal{V}_{\mathbb{A}_4} = \{\boldsymbol{x} \in \mathcal{H} |\ |\boldsymbol{x}| < |\boldsymbol{v} - \boldsymbol{x}|\ \forall\, \mathbf{0} \neq \boldsymbol{v} \in \mathbb{A}_4\}. \tag{41}$$

To construct $\mathcal{V}_{\mathbb{A}_4}$ more concrete the dual lattice $\widetilde{\mathbb{A}_4}$ of $\mathbb{A}_4$ will be useful. Up to a factor of 2π this is the same as the reciprocal lattice

$$\widetilde{\mathbb{A}}_4 = \{\boldsymbol{x} \in \mathcal{H} |\ \boldsymbol{x} \cdot \boldsymbol{v} \in \mathbb{Z}\ \forall\, \boldsymbol{v} \in \mathbb{A}_4\}. \tag{42}$$

A basis of $\widetilde{\mathbb{A}}_4$ is given by $\{\widetilde{\boldsymbol{a}}_i = \boldsymbol{e}_i - \frac{1}{5}\Delta |\ i = 0, 1, 2, 3, 4\}$.

It can be shown that $|\sum_i \lambda_i \widetilde{\boldsymbol{a}}_i| < |\boldsymbol{v} - \sum_i \lambda_i \widetilde{\boldsymbol{a}}_i|$ for all $\boldsymbol{v} \in \mathbb{A}_4$ and $|\lambda_i| < 1/2$. So the Voronoi cell of $\mathbb{A}_4$ can be written as

$$\mathcal{V}_{\mathbb{A}_4} = \{\sum_i \lambda_i \widetilde{\boldsymbol{a}}_i \mid\ |\lambda_i| < 1/2\}. \tag{43}$$

Projecting $\mathcal{V}_{\mathbb{A}_4}$ onto $E^{\perp}$ yields a decagon as shown in fig. 23. For the correct construction of the TTT, it must be half open, similar as for the Fibonacci chain. Otherwise there

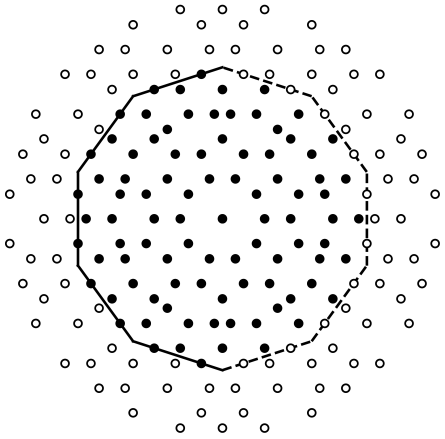

(a) The window $\mathcal{W}$ of the TTT is a half open decagon with edge length $\sqrt{2/5}$, centered at the origin. Projecting all points $\boldsymbol{v} \in \mathbb{A}_4$ onto $E^\perp$, those that lie within $\mathcal{W}$ (black) will be the atoms in $\mathcal{Q}_{\mathrm{TTT}}$. Only a seletion of projected points is shown. Actually, $\mathcal{W}$ is densely filled. Equivalently, one could attach a decagon to each point $v^\perp \in \mathbf{P}^\perp(\mathbb{A}_4)$ and see which of them contain the origin.

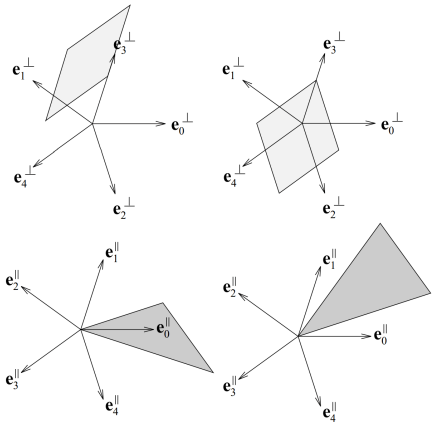

(b) Above: $E^\perp$-projection of the 2-boundaries $\mathcal{B}_2^{(1)}$ (left, angles $\frac{\pi}{5}$ and $\frac{4\pi}{5}$), $\mathcal{B}_2^{(2)}$ (right, angles $\frac{2\pi}{5}$ and $\frac{3\pi}{5}$). Both have edge length $\sqrt{2/5}$.
Below: $E^\parallel$-projection of the dual 2-boundaries $\widetilde{\mathcal{B}}_2^{(1)}$ (left, angles $\frac{\pi}{5}$ and $\frac{3\pi}{5}$), $\widetilde{\mathcal{B}}_2^{(2)}$ (right, angles $\frac{\pi}{5}$ and $\frac{2\pi}{5}$). Both have edge lengths $\sqrt{2/\sqrt{5}\tau}$ and $\sqrt{2\tau/\sqrt{5}}$. [50]

Figure 23

would be 'forbidden' distances between some atoms, corresponding to overlapping tiles. This half-open-condition has no consequences for the polar calculus though, as it does not change the window's area.

In contrast to the PT, the tiles in the TTT cannot be derived alone from the TTT's lattice points. Rather, they must also be projected. The triangle tiles are the $\mathbf{P}^\parallel$-projections of the *dual objects* of the 2-boundaries of $\mathcal{V}_{\mathbb{A}_4}$. In general, m-boundaries are the m-dimensional surface elements of the Voronoi cell. The dual object of an m-boundary is the polytope that is constructed by connecting the points $\boldsymbol{v} \in \mathbb{A}_4$, whose Voronoi cells are sharing that m-boundary. This definition is taken from Zeger [50], as are also the following expressions for the 2-boundaries. They come in two shapes: $\mathcal{B}_2^{(1)}$ and $\mathcal{B}_2^{(2)}$. All 2-boundaries of all the Voronoi cells can be found through lattice translations and D_{10}-group operations of these two prototypes. Each Voronoi cell has 20 2-boundaries of type $\mathcal{B}_2^{(1)}$ and 20 of type $\mathcal{B}_2^{(2)}$

$$\begin{aligned}\mathcal{B}_2^{(1)} &= \{\frac{1}{2}(\widetilde{\boldsymbol{a}}_0 + \widetilde{\boldsymbol{a}}_1 - \widetilde{\boldsymbol{a}}_2 + \lambda_3\widetilde{\boldsymbol{a}}_3 + \lambda_4\widetilde{\boldsymbol{a}}_4)|\ \ |\lambda_j| \leq 1\} \\ \mathcal{B}_2^{(2)} &= \{\frac{1}{2}(\widetilde{\boldsymbol{a}}_0 + \widetilde{\boldsymbol{a}}_1 - \widetilde{\boldsymbol{a}}_3 + \lambda_2\widetilde{\boldsymbol{a}}_2 + \lambda_4\widetilde{\boldsymbol{a}}_4)|\ \ |\lambda_j| \leq 1\}.\end{aligned} \tag{44}$$

The corresponding dual objects, which in a 4D lattice are also two dimensional, are given by

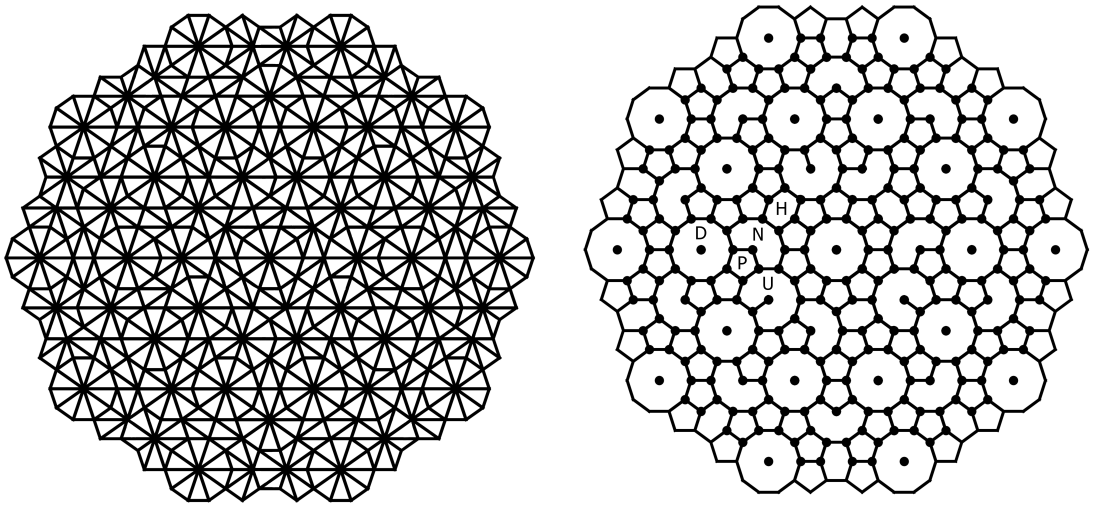

(a) A Patch of the TTT.

(b) A patch of the TTT's atom lattice $\mathcal{Q}$. Connecting all atoms of shortest distance creates 5 prototiles (D, U, N, H, P).

Figure 24

$$\begin{aligned}\widetilde{B}_2^{(1)} &= \{\mu_0(\widetilde{\boldsymbol{a}}_0 - \widetilde{\boldsymbol{a}}_2) + \mu_1(\widetilde{\boldsymbol{a}}_1 - \widetilde{\boldsymbol{a}}_2) |\ \ \mu_j \geq 0,\ \mu_0 + \mu_1 \leq 1\} \\ \widetilde{B}_2^{(1)} &= \{\mu_0(\widetilde{\boldsymbol{a}}_0 - \widetilde{\boldsymbol{a}}_3) + \mu_1(\widetilde{\boldsymbol{a}}_1 - \widetilde{\boldsymbol{a}}_3) |\ \ \mu_j \geq 0,\ \mu_0 + \mu_1 \leq 1\}.\end{aligned} \tag{45}$$

As shown in fig. 23b, $\mathcal{B}_2^{(i)}$ produce the two rhombs from the PT when projected onto $E^\perp$. Projections of the dual objects $\widetilde{\mathcal{B}}_2^{(i)}$ in $E^\parallel$ produce acute and obtuse triangles [9] , similar to those in the Robinson decomposition, but with inverse area ratio $\frac{\text{acute}}{\text{obtuse}} = \tau$. Knowing about these concepts, the construction works as follows:

First, all the $\mathbb{A}_4$-Voronoi cells $\mathcal{V}_{\mathbb{A}_4}(\boldsymbol{v})$ at all the points $\boldsymbol{v} \in \mathbb{A}_4$ are projected onto $E^\perp$. If the (half open) projection of a certain Voronoi cell $\mathbf{P}^\perp(\mathcal{V}_{\mathbb{A}_4}(\boldsymbol{w}))$ contains the origin, the corresponding center point $\boldsymbol{w}$ will be projected onto $E^\parallel$ [10]. The emerging lattice is the TTT's point lattice $\mathcal{Q}_{\text{TTT}}$ as already defined in section 2.2.4. Further, for all projected 2-boundaries of that Voronoi cell $\mathbf{P}^\perp(\mathcal{B}_2(\boldsymbol{w}))$ containing the origin, the corresponding dual 2-boundary $\widetilde{\mathcal{B}}_2(\boldsymbol{w})$ will be projected onto $E^\parallel$. All the tiles $\mathbf{P}^\parallel(\widetilde{\mathcal{B}}_2)$ belonging to one Voronoi cell $\mathcal{V}_{\mathbb{A}_4}(\boldsymbol{w})$ share the atom $\mathbf{P}^\parallel(\boldsymbol{w}) = w^\parallel$ as a common corner point.

Of course, the whole process can also be seen equivalently in the window and strip formalism. Then, the window would be subdivided into regions of different projected 2-boundaries. If an $\mathcal{L}$-point is projected into $\mathcal{W}$, it will hit one such subregion of several overlapping projected 2-boundaries of $\mathcal{V}_{\mathbb{A}_4}(\mathbf{0})$. Then all the corresponding dual 2-boundaries in that $\mathcal{L}$-points Voronoi cell will be projected onto $E^\parallel$. So each of these

[9] Projecting in $E^\parallel$, $\mathcal{B}_2^{(i)}$ also produce rhombs, but switched types as in fig. 23b. Likewise, $\widetilde{\mathcal{B}}_2^{(i)}$ produce switched triangles, being projected in $E^\perp$. These projections are important for the PT-construction but not for the TTT.

[10] This is the description of atomic surfaces, which where defined in section 2.2.4 as the inverted window $-\mathcal{W}$. This inversion can be neglected in the TTT as the Voronoi cell $\mathcal{V}_{\mathbb{A}_4}$ is centro-symmetric.

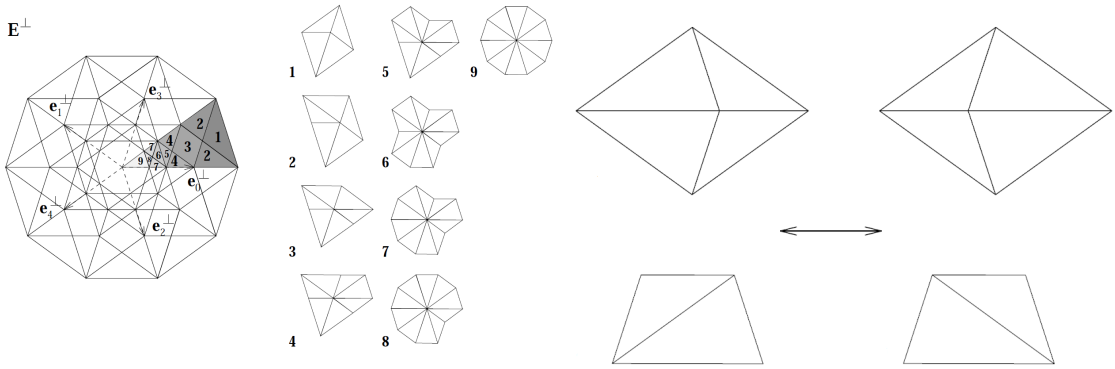

(a) There are 9 types of vertices in the TTT. The acceptance domain of a vertex is found as the intersection of the $\mathbf{P}^{\perp}$-projected 2-boundaries corresponding to its tiles. As all tiles of one vertex must come from the same Voronoi cell, one can find all possible vertex types by projecting all 2-boundaries of $\mathcal{V}_{\mathbb{A}_4}$ into $E^{\perp}$ and counting the areas.[50]

(b) The two elementary flips of the TTT. Above: Simpleton flip. Below: Trapeze flip. [50]

Figure 25

subregions in $\mathcal{W}$ is the acceptance domain for one type of vertex. The subdivided window and the nine vertex types (up to D_{10}-operations) are shown in fig. 25a.

The TTT is shown in fig. 24a. Next to it, fig. 24b shows the point lattice $\mathcal{Q}_{\mathrm{TTT}}$. Connecting all points in $\mathcal{Q}_{\mathrm{TTT}}$ to their closest possible neighbours creates a tiling with five prototiles: a regular decagon (D), a concave decagon (U), a concave nonagon (N), a non-regular hexagon (H) and a regular pentagon (P). As they are obviously MLD, we will not distinguish between the point lattice with and without connections and call both $\mathcal{Q}_{\mathrm{TTT}}$. In general, some phasonically distorted version of the TTT's point lattice will be called $\mathcal{Q}(\boldsymbol{\chi})$ or just $\mathcal{Q}$, hence $\mathcal{Q}(\mathbf{0}) = \mathcal{Q}_{\mathrm{TTT}}$

There are two kinds of elementary flips in the TTT, shown in fig. 25b. In the simpleton or rhombus flip a lattice point jumps by a distance $\frac{1}{\tau}\sqrt{\frac{2}{\sqrt{5}\tau}}$. In $E^{\perp}$ this corresponds to shifting two $\mathcal{L}^{\perp}$-points into and out of the window. The trapeze flip does not move any $\mathcal{Q}-$points, but it changes local tile configurations and thereby local vertices. The corresponding process in $E^{\perp}$ is an $\mathcal{L}^{\perp}$-point that is shifted within $\mathcal{W}$, but exits and enters the $\mathbf{P}^{\perp}$-projections of different 2-boundaries.

When a tiling as the TTT is used to model a real QC, the tiles are equipped with an atom decoration. Note that in general, the points in the lattice $\mathcal{Q}_{\mathrm{TTT}}$ must not be atoms. They are first of all just part of the abstract tiling. In [7], the TTT was used to model a decagonal QC phase of an Al-Cu-Co alloy. The acute and obtuse triangle were decorated with 34 and 21 atoms on their interior respectively. In this case, every trapeze or simpleton flip corresponds to a restructuring of many atoms. Comparing simulations of this model to experimental data, the article concluded that the Al-Co-Cu QC is a random tiling.

The present thesis shall focus on a much simpler model, where there is only one type of particle, and all particles sit exactly on the $\mathcal{Q}$-points. So a simpleton flip describes a single atom jump, while the trapeze flip has no meaning. In general, the edges of the triangle tiles will be completely ignored because they belong only to the TTT, which is not reconstructable from $\mathcal{Q}_{\mathrm{TTT}}$. In this context it is also legitimate to call the lattice points in $\mathcal{Q}$ atoms from now on. The tiles D, U, N, H, P (call them $\mathcal{Q}$-tiles) from fig. 24b are useful to talk about atom arrangements in $\mathcal{Q}$. But note that unlike the triangle tiles, the $\mathcal{Q}$-tiles are not invariant to phasonic strain and flips. Connecting all atoms of shortest distance in a phasonically distorted lattice $\mathcal{Q}(\boldsymbol{\chi} \neq \mathbf{0})$, many more shapes than only these five can be found. However, it turns out that all the CPS-crystals $\mathcal{Q}(\boldsymbol{\chi})$ considered in this work will be fully covered by these five tiles, as long as they have homogeneous phasonic strain.

3.1.2 The Phason Elastic Free Energy

The goal is to compare different tiling ensembles with different global phasonic strain (GPS-classes) and see which is the most stable one. Hence, we want to find the global phasonic strain $\boldsymbol{\chi}$ that minimizes the free energy function $F(\boldsymbol{\chi})$, which is called *phason elastic free energy*. Note again that $\boldsymbol{\chi}$ is not a parameter that can be changed directly in an experiment. The free energy comparison means, we pretend all the GPS-classes could be in thermal equilibrium and have constant valued F. In reality only the GPS-class with minimal $F(\boldsymbol{\chi})$ can be in thermal equilibrium. All other GPS-classes should undergo a phase transition into the stable GPS-class. Only by restricting the theoretical crystal to have a fixed $\boldsymbol{\chi}$-value, we can compute its hypothetical equilibrium free energy.

The random tiling hypothesis states that for some temperature $T > 0$ the quasicrystalline GPS-class is the most stable one, so $F(\boldsymbol{\chi}, T)$ should be minimal for $\boldsymbol{\chi} = \mathbf{0}$. Let us assume the free energy is an analytical function in $\boldsymbol{\chi}$. The calculations presented in this thesis will only compare GPS-classes in a very small $\boldsymbol{\chi}$-interval arond $\mathbf{0}$, so it will be sufficient to expand $F(\boldsymbol{\chi})$ only to second order. Any minima of F found this way are only local minima

$$F(\boldsymbol{\chi}) = F_0 + C_{ij}\ \chi_{ij} + M_{ijkl}\ \chi_{ij}\chi_{kl} + \mathcal{O}(\boldsymbol{\chi}^3). \tag{46}$$

In eq. (46), as also in the following equations, the Einstein summation convention is used. C_{ij} and M_{ijkl} are elements of coefficient matrices. They are called *phason elastic constants* (or just phasonic constants). All other dependencies of F besides phasonic strain, like temperature, are contained in these phason elastic constants. $F_0 = F(\boldsymbol{\chi} = \mathbf{0})$ is the QCs free energy. Together with the decagonal symmetry of the $\mathbb{A}_4$ lattice, this second order expansion allows to simplify the form of F strongly.

As explained in the previous section, the group D_{10} acts on $E^{\parallel}$ and $E^{\perp}$ through the irreducible representations (IRs) Γ_5 and Γ_7. Let $x^{\parallel\prime}$ or $x^{\perp\prime}$ denote vectors after transformation by some group operation $g \in D_{10}$. Then we write

$$\begin{aligned} x_i^{\parallel\prime} &= \Gamma_5^{ij} x_j^{\parallel} \\ x_i^{\perp\prime} &= \Gamma_7^{ij} x_j^{\perp}, \end{aligned} \tag{47}$$

where $x_i^{\parallel}$ and Γ^{ij} are components of a vector or a matrix respectively. The phasonic strain tensor is the derivative of an $E^{\perp}$-vector $u^{\perp}$ (the phasonic displacement) with respect to $E^{\parallel}$-coordinates $x^{\parallel}$. Its componentwise transformation behaviour under a D_{10}-operation g is calculated using the chain rule

$$
\begin{aligned}
\chi'_{ij} &= \frac{\partial u_i^{\perp\prime}}{\partial x_j^{\parallel\prime}} = \frac{\partial u_i^{\perp\prime}}{\partial x_k^{\parallel}} \frac{\partial x_k^{\parallel}}{\partial x_j^{\parallel\prime}} \\
&= \frac{\partial\Big(\Gamma_7^{il}(g) u_l^{\perp}\Big)}{\partial x_k^{\parallel}} \frac{\partial\Big(\Gamma_5^{km}(g^{-1}) x_m^{\parallel\prime}\Big)}{\partial x_j^{\parallel\prime}} = \Gamma_7^{il}(g) \frac{\partial u_l^{\perp}}{\partial x_k^{\parallel}} \Gamma_5^{mk}(g) \frac{\partial x_m^{\parallel\prime}}{\partial x_j^{\parallel\prime}} \\
&= \Gamma_7^{il}(g)\Gamma_5^{jk}(g) \frac{\partial u_l^{\perp}}{\partial x_k^{\parallel}} = \Big[\underbrace{\Big(\Gamma_7(g) \otimes \Gamma_5(g)\Big)}_{\mathcal{R}_\chi(g)} \cdot \overrightarrow{\chi} \Big]_{ij}.
\end{aligned}
\tag{48}
$$

In the second line, we used the fact that any two orthonormal vectors stay orthonormal upon a D_{10} operation, hence $\partial x_m^{\parallel\prime} / \partial x_j^{\parallel\prime} = \delta_{mj}$. Also, the matrices $\Gamma(g)$ are elements of the orthogonal group $O(n)$, so it is $\Gamma(g^{-1}) = \Gamma^T(g)$. The transformation of the 2×2 matrix $\boldsymbol{\chi}$ can be represented by the 4×4 matrix $\mathcal{R}_\chi(g)$ acting on the component vector $\overrightarrow{\chi} = [\chi_{11}, \chi_{22}, \chi_{12}, \chi_{21}]^t$.

The free energy F should of course not be changed by any D_{10} operation, so it transforms via the trivial representation Γ_1. Then eq. (46) makes sense only if the right side also transforms via Γ_1. So $F(\boldsymbol{\chi})$ must be a sum of D_{10}-invariant polynomials of first and second order in $\boldsymbol{\chi}$, each multiplied by a phasonic constant. We now want to find these polynomials.

From group theory it is known that a tensor product of two IRs contains Γ_1 iff the IRs are equal. As this is not the case for $\mathcal{R}_\chi$, there are no D_{10}-invariant first order polynomials. For the invariant polynomials of second order consider the decomposition of $\mathcal{R}_\chi$ into IRs.

$$
\mathcal{R}_\chi = \Gamma_6 \oplus \Gamma_8. \tag{49}
$$

Using the decomposition formula eq. (36) again, one finds that Γ_1 is contained once in $\Gamma_6 \otimes \Gamma_6$ and $\Gamma_8 \otimes \Gamma_8$, and hence twice in $\mathcal{R}_\chi^{\otimes 2} = (\Gamma_6 \otimes \Gamma_6) \oplus (\Gamma_8 \otimes \Gamma_8) \oplus (\Gamma_6 \otimes \Gamma_8) \oplus (\Gamma_8 \otimes \Gamma_6)$. This means, written in its symmetry adapted basis, the second order component vector $\overrightarrow{\chi} \otimes \overrightarrow{\chi}$ includes two polynomials transforming via Γ_1. The symmetry adapted first order component vector $\overrightarrow{\chi}_s$ and its corresponding basis of 2×2 matrices were computed by Koschella [48]

$$
\overrightarrow{\chi}_s = \begin{bmatrix} \chi_1^{(6)} \\ \chi_2^{(6)} \\ \chi_1^{(8)} \\ \chi_2^{(8)} \end{bmatrix} = \frac{1}{\sqrt{2}} \begin{bmatrix} 1 & -1 & 0 & 0 \\ 0 & 0 & 1 & 1 \\ 1 & 1 & 0 & 0 \\ 0 & 0 & 1 & -1 \end{bmatrix} \begin{bmatrix} \chi_{11} \\ \chi_{22} \\ \chi_{12} \\ \chi_{21} \end{bmatrix} \tag{50}
$$

$$
\boldsymbol{\chi} = \frac{\chi_6^{(1)}}{\sqrt{2}} \begin{bmatrix} 1 & 0 \\ 0 & -1 \end{bmatrix} + \frac{\chi_6^{(2)}}{\sqrt{2}} \begin{bmatrix} 0 & 1 \\ 1 & 0 \end{bmatrix} + \frac{\chi_8^{(1)}}{\sqrt{2}} \begin{bmatrix} 1 & 0 \\ 0 & 1 \end{bmatrix} + \frac{\chi_8^{(2)}}{\sqrt{2}} \begin{bmatrix} 0 & 1 \\ -1 & 0 \end{bmatrix}. \tag{51}
$$

The labeling is chosen according to the group representation, so $\chi_i^{(n)\prime} = \Gamma_n^{ij} \chi_j^{(n)}$ for $n \in \{6, 8\}$ and $i, j \in \{1, 2\}$. In principle, one could now also compute the symmetry adapted second order component vector $(\overrightarrow{\chi} \otimes \overrightarrow{\chi})_s$ to see which combination of product components $\chi_{ij}\chi_{kl}$ transforms with which IR. However, we are only interested in those two polynomials transforming by Γ_1. It is not hard to guess that they should be very

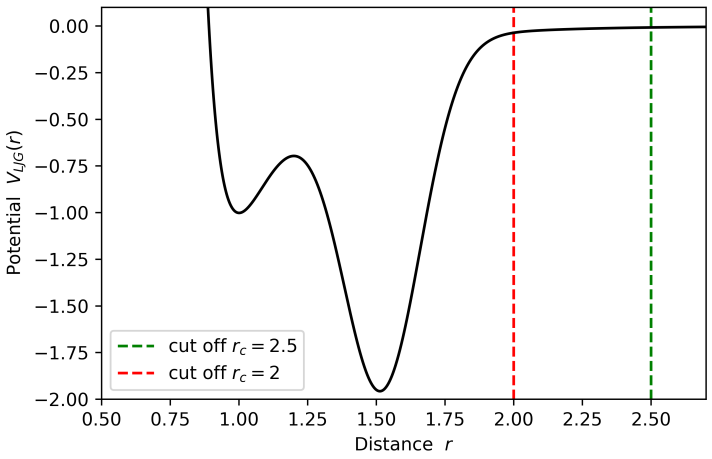

Figure 26: The LJG-potential with parameters $\epsilon = 1.8$, $r_0 = 1.52$, $\sigma^2 = 0.02$. The cutoff radius $r_c = 2.5$ was used in Engel's MD-simulation. The cut off radius $r_c = 2$ was used by Kiselev to define nine different atom environments.

symmetric. Using the explicit matrix form of Γ_6 and Γ_8, one can check that the transformation behaviour of $(\chi_1^{(6)})^2 + (\chi_2^{(6)})^2$ and $(\chi_1^{(8)})^2 + (\chi_2^{(8)})^2$ is trivial. So the free energy, up to second order, written in its simplest form reads

$$F(\boldsymbol{\chi}, T) = F_0 + \frac{1}{2}\lambda_6(T)\Big((\chi_1^{(6)})^2 + (\chi_2^{(6)})^2\Big) + \frac{1}{2}\lambda_8(T)\Big((\chi_1^{(8)})^2 + (\chi_2^{(8)})^2\Big). \tag{52}$$

If the two symmetry adapted phasonic constants λ_6, λ_8 are positive, the free energy has a minimum at $\boldsymbol{\chi} = \mathbf{0}$. So an entropical stabilization of the QC phase means that there is some $\widehat{T} > 0$, such that $\lambda_6(T), \lambda_8(T) > 0$ for all $T > \widehat{T}$. Given a concrete free energy function $F(\boldsymbol{\chi}, T)$, the phasonic constants are obtained by the second derivative $\lambda_n = \frac{\partial^2 F}{\partial \chi_i^{(n)2}}$ $n \in \{6, 8\}$. So the simpler free energy function $F(\chi_6^{(1)}, \chi_8^{(1)}, T)$ with $\chi_6^{(2)} = \chi_8^{(2)} = 0$ is already sufficient to find λ_6 and λ_8.

Analogous to the phason elastic contribution, one can also consider the phonon elastic contribution to the free energy. The phasonic strain χ_{ij} and phononic strain $\varepsilon_{ij} = \partial u_i^{\parallel}/\partial x_j^{\parallel}$ can be combined to one tensor η_{ij} that describes both, deformations in $E^{\perp}$ and in $E^{\parallel}$. Computing the combined free energy $F(\boldsymbol{\eta})$, couplings between phasonic and phononic modes are also possible. For decagonal systems this was investigated in the diploma thesis [63].

3.2 The Original Simulation by Michael Engel

In his dissertation from 2008 [9], Michael Engel studied a pair potential called the Lennard-Jones Gauß-potential (LJG-potential). This double well potential is a superposition of a conventional Lennard-Jones potential and a negative Gauß-curve

$$V_{\mathrm{LJG}}(r) = \frac{1}{r^{12}} - \frac{2}{r^6} - \epsilon \exp\left\{-\frac{(r - r_0)^2}{2\sigma^2}\right\}. \tag{53}$$

The parameters ϵ, r_0 and σ can be adjusted to model different types of interaction. Engel performed 5000 annealing MD-simulations, varying r_0 within the interval $[1.11, 2.1]$ and

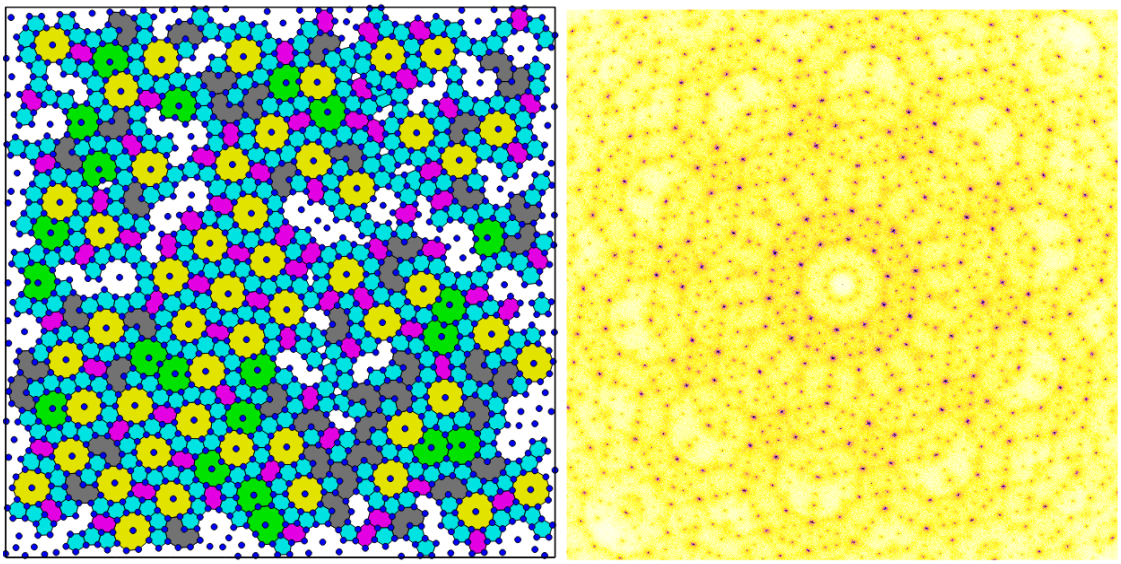

(a) Screenshot of the MD-crystal at T=0.45. [9] (b) Diffraction pattern of the MD-crystal at T=0.5. Tenfold symmetry is clearly visible. [9]

Figure 27

ϵ in the interval $[0.1, 5]$. The width of the bell curve was fixed at $\sigma^2 = 0.02$. Also, the interaction was neglected between any two particles with a distance $r > 2.5$. So to speak, the potential was cut off at $r = 2.5$. Right from its definition, the LJG-potential was introduced without units for any of its parameters or for the distance r. These simulations used 1024 particles in an NVT-ensemble with open boundary conditions. Starting from a random configuration the temperature was increased till the liquid or gas phase was reached. Then the temperature was lowered over $2 \cdot 10^6$ MD-steps till a well ordered polycrystalline or monocrystalline phase was observed. This way a wide variety of crystal structures for different r_0 and ϵ-parameters was found. Besides many regular, periodic crystals also a dodecagonal and a decagonal quasicrystalline phase was discovered. They were identified by computing the material's diffraction image. Engel found the decagonal phase to be stabilized best with the following parameters.

$$\epsilon = 1.8 \qquad r_0 = 1.52 \qquad \sigma^2 = 0.02 \tag{54}$$

A second MD-simulation using these parameters and 1600 particles in an NPT-ensemble with periodic boundary conditions was performed to investigate the decagonal phase in detail. A first order phase transition from liquid to solid phase was observed at melting temperature

$$T_m = 0.56 \pm 0.02. \tag{55}$$

This solid decagonal phase (figs. 27a and 28) shows strong similarities with the TTT's point lattice $\mathcal{Q}_{\mathrm{TTT}}$. The D, U, N, H and P-tiles are prominently present. They are not of the same size as they would be in the mathematical construction from section 3.1.1. The ratio of the shortest atom distance in the MD-crystal to the shortest atom distance in the mathematical crystal is approximately $\gamma = 1.2629$. To compute the potential energies of atoms in a lattice $\mathcal{Q}$, we construct it as in section 3.1.1 and then scale it by γ. Of course

the particles always vibrate around the potential minimum, so γ is only an average value.

But also besides this scale difference, the phase is certainly not LI with $\mathcal{Q}_{\mathrm{TTT}}$. It has several defects that can not be consistently filled by $\mathcal{Q}$-tiles. And in many places the $\mathcal{Q}$-tiles stick together in forbidden ways with respect to $\mathcal{Q}_{\mathrm{TTT}}$. For example a U-tile sticking to another U-tile does never occur in $\mathcal{Q}_{\mathrm{TTT}}$. Rather all U-tiles in the ideal QC are attached to a D-tile. Regularities like this can be proven with the polar calculus. In this case, it means that the AD of a U-tile $\overline{U}$ and the AD of a U-tile attached to a D-tile $\overline{UD}$ are equal. These defects together with the clearly decagonal, but also diffuse diffraction pattern (fig. 27b) lead to the conclusion that this decagonal phase is a randomized version of $\mathcal{Q}_{\mathrm{TTT}}$.

But it is also not maximally random. That would mean that all possible ways to cover a finite size patch with acute and obtuse triangles of fixed density would have the same probability. Clearly the triangle combinations that are the $\mathcal{Q}$-tiles are preferred in the MD-crystal over other compound tiles. For example two P-tiles attached to a D-tile is a very frequent sight in fig. 28. The concave octagon tile, which is not one of the $\mathcal{Q}$-tiles, shows up very seldom. However, as shown in fig. 29 the pentagons could form into an octagon tile through a single flip, which would not change the patch area, the tile numbers, nor the global phason strain. So why do almost none of these pentagon pairs spontaneously flip into an octagon? The answer must be that the configuration including the pentagons has a lower potential energy than the configuration including the octagon. Since this crystal is stabilized at finite temperature, such differences of potential energy cause different thermal probabilities. This is the scenario mentioned at the end of section 2.5. The LJG-potential stabilizes the triangle tiles from the TTT, but the LJG-interaction reaches beyond the tiles and the different combinations of triangles are not energetically degenerate.

Besides the rather seldom, but still possible flip example above, flips were in general a frequent feature in this RT QC. Flip frequencies were measured from 10^{-7} up to 10^{-4} flips per MD-step and per particle. And particles moved up to 4 flip-distances [11] away from their inital position within 10^4 MD-steps.

However, this RT-version of $\mathcal{Q}_{\mathrm{TTT}}$ was not the ground state in the MD-simulation. Cooling the crystal down extremely slowly with over 10^9 MD-steps and open boundaries a phase transition was observed below $T = 0.4$. The order parameter in this second order phase transition is the squared average phasonic strain, seen in fig. 30a. The open boundaries are very important here. In theory, an infinite number of infinitely far correlated flips is necessary for a change of $\overline{\boldsymbol{\chi}}$. As this is not possible in a simulation with a finite number of particles, it is expected that excessive restructurings are happening at the sample's boundaries, which account for hypothetical correlations beyond the boundaries. Closed boundaries would fix the 2D hypersurface at its borders, allowing no global change of orientation. Periodic boundaries would effectively make the sample one of infinitely many identical unit cells in an approximant. Again, the flips could not correlate beyond the unit cell. As all finite phasonic fluctuations that happen within the sample happen identically in all other cells, the overall orientation of the hypersurface would stay unchanged. $\overline{\boldsymbol{\chi}}$ was measured, as mentioned in section 2.5, by projecting the lattice points into the hyperspace and fitting a plane. The relation between Engel's notation in fig. 30a and our symmetry adapted notation is $\chi_1 = (\chi_1^{(6)} + \chi_2^{(6)})/\sqrt{2}$ and $\chi_2 = (\chi_1^{(8)} + \chi_2^{(8)})/\sqrt{2}$. The phase transition temperature T_c was measured as

[11] A flip distance is the distance between the two minima in the LJG-potential.

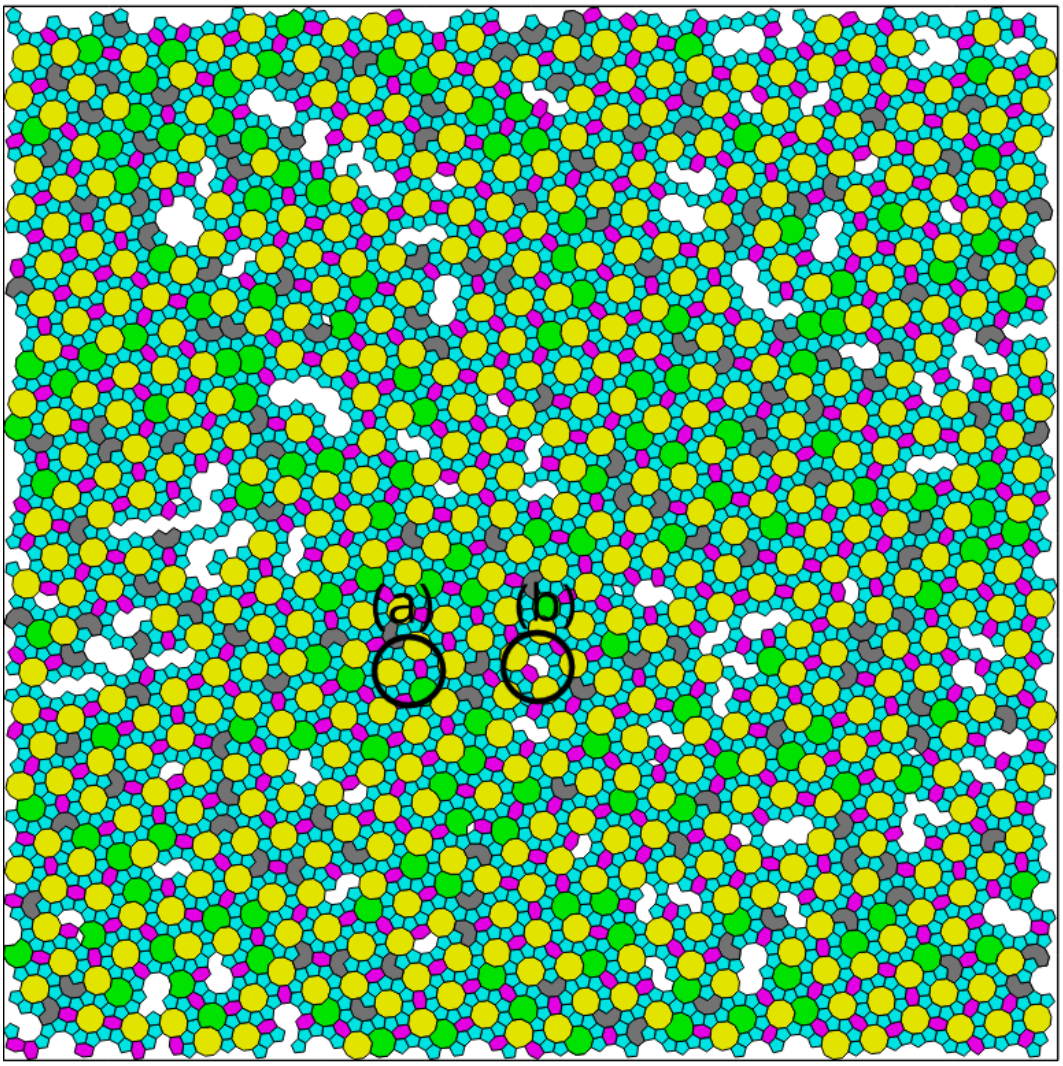

Figure 28: Screenshot of the MD-crystal at T=0.5. (a): Two or more P-tiles attached to a D-tiles is a very frequent tile combination. (b): This concave octagon tile is very seldom. The octagon is colored white, like all tiles that are forbidden in $\mathcal{Q}_{\mathrm{TTT}}$. [9]

$$T_c = 0.37 \pm 0.03. \tag{56}$$

During the cooling the density of D-tiles increases continuously. For a neighbourhood of eleven particles the D-tiles are the configuration of lowest energy. The phase that is finally stabilized as $T \to 0$ is a periodic crystal called the Xi-approximant. Actually, there are two ground state approximants Xi_1 and Xi_2 differing only slightly in the arrangement of the D-tiles (for details see Kiselev's diploma [10]). But they both have the same density of D-tiles, the same number of atoms per unit cell and the same ground state energy.

Additionally to this cooling simulation, Engel computed the ground state energy as a function of the global phasonic strain. For that, he performed simulations of 2061 approximants of different phason strain, relaxing them from $T = 0.3$ down to $T = 0$. These approximants did not emerge naturally from the simulation, but rather were constructed

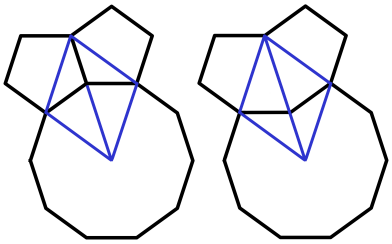

Figure 29: In an RT-version of $\mathcal{Q}_{\mathrm{TTT}}$, two P-tiles attached to a D-tile could flip into an octagon-tile and a U-tile. But in the MD-crystal based on the LJG-potential such a flip seems to be suppressed. The conclusion is that the two configurations have different potential energies and different thermal probabilities.

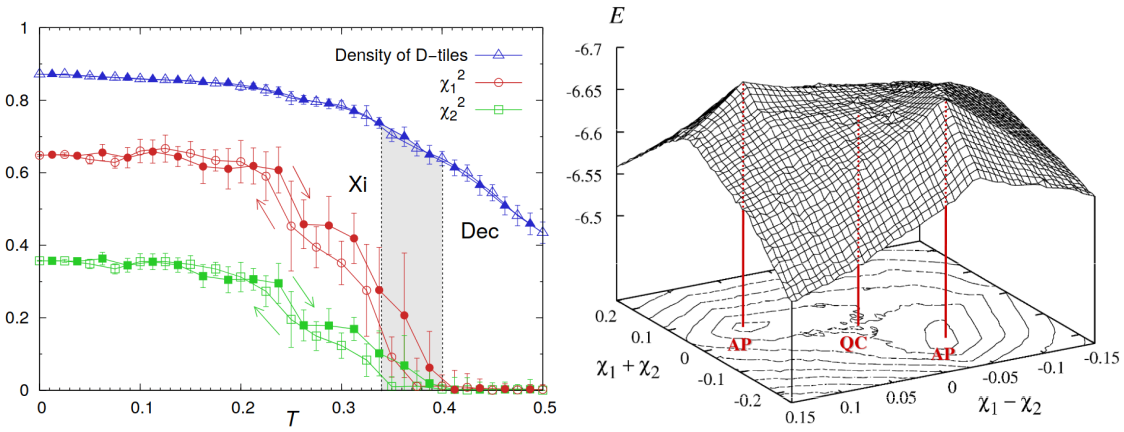

(a) Global phasonic strain and density of D-tiles plotted over temperature. The χ-curves show a 2nd order phase transition between the QC ($\boldsymbol{\chi} = \mathbf{0}$) and the Xi-approximant. [9]

(b) The ground state energy as a function of the phaonic strain. The two Xi-approximants are energy minima, while the QC lies on a saddle point [9]

Figure 30

directly from the CPS. Due to periodic boundaries, the global phason strain could not be changed. Starting from the ideal tiling with completely constant $\boldsymbol{\chi}$, alternating between MD-simulation and MC (Monte-Carlo)-simulation, the energetically lowest tiling in each of the 2061 GPS-classes was found and its energy computed numerically. This process of performing flips to lower the potential energy while keeping $\boldsymbol{\chi}$ fixed is called *phasonic relaxation*. Fig. 30b shows the resulting energy surface. Indeed the Xi-approximants have the lowest energy of all the GPS-classes. The QC lies on a saddle point [12] , so it is not stable at $T = 0$. For the phason elastic constants this saddle point corresponds to $\lambda_6(T = 0) > 0$ and $\lambda_8(T = 0) < 0$. We see that the approximation of the free energy F as a quadratic function of $\boldsymbol{\chi}$ is indeed only valid in a small interval around $\boldsymbol{\chi} = \mathbf{0}$. However, the information $\lambda_8(T = 0) < 0$ alone is enough to know that the QC is not stable at $T = 0$.

[12] Note that this hypothetical QC at $T = 0$ is not a random tiling, but also probably not the ideal $\mathcal{Q}_{\mathrm{TTT}}$. Rather it is that tiling of the $\boldsymbol{\chi} = \mathbf{0}$ GPS-class with lowest energy. It may also be one of several degenerate ground state tilings. Unfortunately pictures were not provided.

3.3 Phasonic Free Energy by Kiselev

A simple model for the phasonic free energy of a crystal stabilized by the LJG-potential was introduced in Kiselev's diploma thesis [10]. Its results were also published in a review letter from 2012 [64]. The model combined analytical and numerical methods. First we will show how the potential energy of any tiling can be computed and how the polar calculus comes into play. Then the phasonic relaxation and the dynamic part of the phasonic free energy will be explained.

3.3.1 The Energy of the TTT

Consider for now the ideal TTT, or rather the point lattice $\mathcal{Q}_{\mathrm{TTT}}$. Each atom is connected to every other atom via the LJG-potential V_{LJG}. Every pair of atoms contributes to the potential energy of the whole tiling by an amount $V_{\mathrm{LJG}}(r)$, where r is the distance between the two atoms. But since the LJG-potential falls to 0 as $r \to \infty$, actually it is equal to 0 for $r > 2.5$, every atom can only couple to atoms within a circle of radius 2.5, which shall be called the interaction circle of the central atom. All atoms in the interaction circle must sit on the corners of hypothetical triangle tiles. Due to the fixed size and number of possible orientations of the triangle tiles, there are only finitely many ways to distribute atoms in any finite circle. Specifically in $\mathcal{Q}_{\mathrm{TTT}}$ the number of atom arrangements is even more restricted by the fact that all atoms must be in a neighbourhood that corresponds to one of the nine vertices of the TTT (fig. 25a). The potential energy of a certain atom with an environment C_j of neighbour atoms in its interaction circle is given by

$$E_j = \sum_{\overrightarrow{r} \in C_j} V_{\mathrm{LJG}}(|\overrightarrow{r}|), \tag{57}$$

where $\overrightarrow{r} \in C_j$ is the difference vector between the central atom and some neighbour atom. Now, if there are M possible atom configurations C_i, $i = 1, ..., M$ for an interaction circle to be covered by, the potential energy of any finite patch $\mathcal{P}$ is exactly given by

$$E_{\mathcal{P}} = \frac{1}{2} \sum_{i=1}^{M} \#C_i|_{\mathcal{P}} E_i, \tag{58}$$

where the number $\#C_i|_{\mathcal{P}}$ counts how many atoms in $\mathcal{P}$ have an environment C_i covering their interaction circle. The factor $1/2$ is necessary because the sum counts every pair of atoms twice. In the infinite crystal $\mathcal{Q}_{\mathrm{TTT}}$, the energy should be replaced by an energy density, and hence the number of C_i configurations should be replaced by a density ρ_{C_i}. So the potential energy density of the TTT is

$$E_{\mathrm{TTT}} = \frac{1}{2} \sum_{i=1}^{M} \rho_{C_i} E_i. \tag{59}$$

The configuration densities can be calculated from the polar calculus. Eq. 59 works of course also for every other tiling with atoms coupling via the LJG-potential. For those tilings that are directly constructed from the CPS with a constant phasonic strain, the energy can be denoted $E(\boldsymbol{\chi})$ with M and ρ_i depending on $\boldsymbol{\chi}$. All other LI-classes are only reached through flips from a given tiling with constant $\boldsymbol{\chi}$. Then M and ρ_i will also depend on the flip sequence, or on the corresponding inhomogeneous function $\boldsymbol{\chi}(x^{\parallel})$.

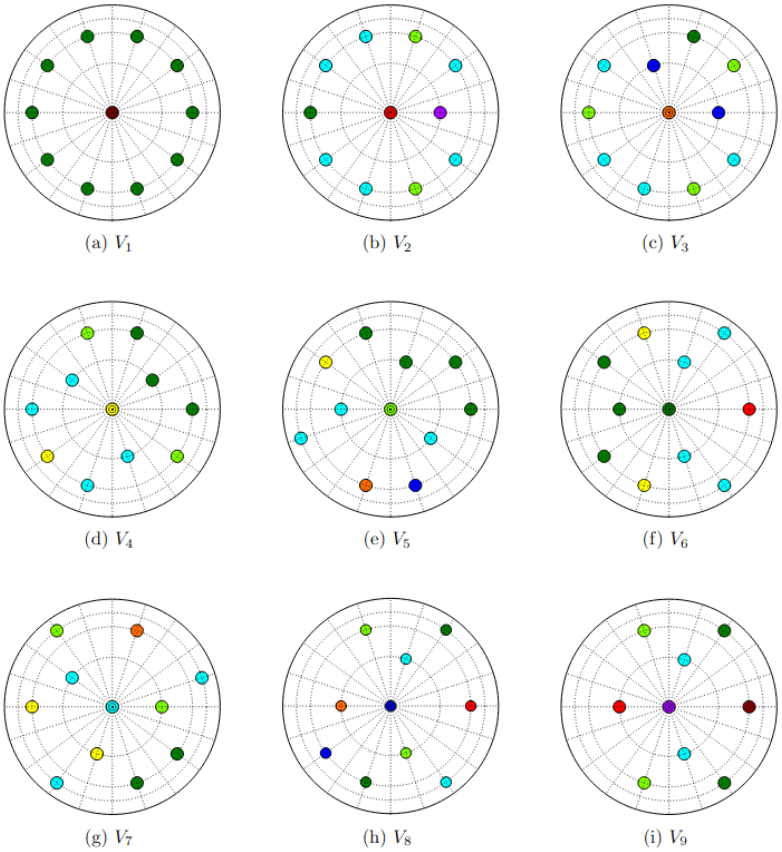

(a) V_1 (b) V_2 (c) V_3

(d) V_4 (e) V_5 (f) V_6

(g) V_7 (h) V_8 (i) V_9

Figure 31: The nine vertex environments within a radius $r_c = 2$ in the ideal TTT-point lattice. The color of the central atom is unique for its environment. but colors of the surrounding atoms are not unique. E.g., the surrounding atoms of V_1 are not all of type V_6 (green) in general. [10]

Label	Energy	Density
V_1	-19.5613	τ^{-6}
V_2	-18.3934	τ^{-9}
V_3	-17.2254	$2\tau^{-8}$
V_4	-16.0575	$2\tau^{-7}$
V_5	-14.4702	$2\tau^{-6}$
V_6	-12.8829	$4\tau^{-5}$
V_7	-11.2956	$2\sqrt{5}\tau^{-6}$
V_8	-10.9268	$4\tau^{-8}$
V_9	-8.9706	τ^{-9}

Table 2: Binding energies and densities of the nine vertex types [10].

Kiselev used eq. 59, or rather a close approximation of it. That is, instead of considering all possible atom environments in a circle or radius 2.5, he chose a smaller cutoff radius $r_c = 2$. Of course in a smaller circle there are in general less possible atom environments. In case of the perfect point lattice $\mathcal{Q}_{\mathrm{TTT}}$, there are 9 atom or vertex environments,

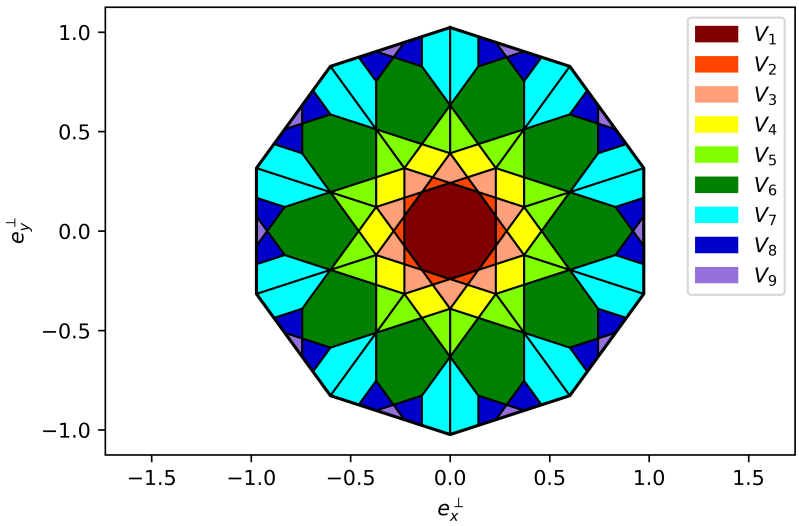

Figure 32: The window of $\mathcal{Q}_{\mathrm{TTT}}$, decomposed into acceptance domains of the nine vertex types. For each vertex type, there are ten domains for the ten possible orientations. If the configuration is not reflection symmetric, different reflections have their own acceptance domain. In the QC, domains of different orientations or reflections of a certain configuration are congruent.

denoted as $V_1, .., V_9$. They are shown in fig. 31. The approximation is justified by the fact that the LJG-potential is already very close to 0 at $r_c = 2$ (comp. fig. 26). Kiselev also computed the energy and density of each vertex type, noted in table 2. The densities were obtained using the polar calculus. Fig. 32 shows the decomposition of the window into the different acceptance domains. The resulting potential energy density of the TTT is

$$E_{\mathrm{TTT}} = -2.8025. \tag{60}$$

3.3.2 Phasonic Relaxation and Flip Dynamics

Looking at the nine environments in fig. 31, one finds that $V_4, .., V_9$ include four neighbour atoms arranged like the corners of the simpleton rhombus. Atoms with these environments can flip. But, as seen in fig. 32, the combined AD of these vertices is much larger than the AD of the simpleton rhombus in the TTT (fig. 25a). That is because the extra edges in the TTT constitute an additional constraint, compared to $\mathcal{Q}_{\mathrm{TTT}}$. The long edges could be rearranged such that the TTT vertices $2, .., 6$ would also include the simpleton rhombus. The point lattice $\mathcal{Q}_{\mathrm{TTT}}$ is invariant under any such rearrangement, which also shows that the two tilings are not MLD.

The flips are assumed to be the crucial source of entropy in the quasicrystal. Of course, in reality there are also phonons and lattice defects, which both will be ignored in this thesis. By lattice defects we mean atom clusters in the crystals that cannot be filled with the golden triangle tiles. As seen in the screenshots, fig. 27a and 28, such defects are indeed very rare. In fig. 28, almost all of the white areas can be covered by triangle tiles. They are valid components in the randomized TTT, and are part of the flip dynamics. For the phonon contribution to the free energy, Kiselev showed that it is independent

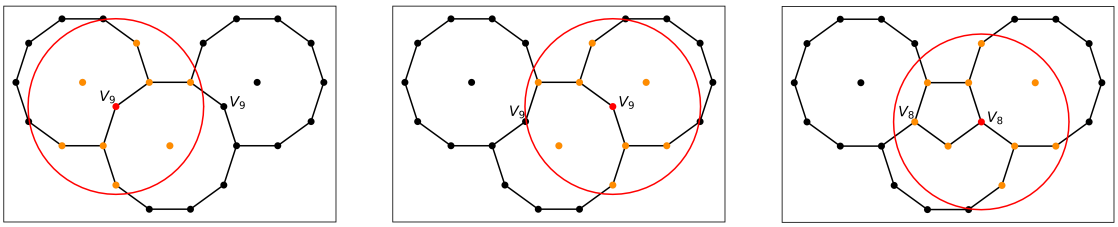

(a) (b) (c)

Figure 33: These two V_9-vertices are correlated. The red circle marks the potential cutoff $r_c = 2$. After the left V_9-vertex performs a $V_9 \to V_9$-flip, the atomic configuration around the right V_9-vertex within the radius r_c is unchanged, so it is still also V_9. But due to the change in the larger environment its flipping behaviour is now $V_9 \to V_8$. Flip sequences like this are part of the phasonic relaxation.

of the phason strain, at least in the interval $-0.03 < \chi < 0.03$. This was done using the Frenkel-Ladd-Method, which allows to numerically compute the difference of vibrational free energies of two hamiltonian systems. If one system is chosen simple enough to solve the free energy exactly, the absolute value of the free energy of the other system (some crystal $\mathcal{Q}(\boldsymbol{\chi})$) can also be obtained. So even though they might contribute to the entropy, the phononic excitations do not contribute to the QCs stability. The Frenkel-Ladd-Method is only valid as long as there are no structural changes in the system. Especially, it does not take the effect of phasonic flips into account.

To compare the ground states energies of different GPS-classes, Kiselev used a similar method as Engel. Using the CPS he created a variety of approximants, either with phasonic strain $\chi_6^{(1)}$ or $\chi_8^{(1)}$ and $-0.03 < \chi_n^{(1)} < 0.03$, $n \in \{6, 8\}$. The approximant that comes closest to the QC had phasonic strain $\chi_6^{(1)} = 0.000198$ or $\chi_8^{(1)} = -0.000122$. For all of these approximants, he computed the ground state of their GPS-class using phasonic relaxation with MD and MC-simulation. In the MC-process, randomly chosen particles were flipped with a probability $\exp\left\{-\widehat{\Delta E}/T\right\}$ till the potential energy converged. $\widehat{\Delta E}$ denotes the difference of that particle's energy before and after the flip, where the two energies are calculated with eq. (57). Note that this process includes correlations between flips. One example for energy lowering flip correlations is shown in fig. 33. In the beginning, there are two flipable particles in configuration V_9. As an individual flip, both would again end up as V_9-vertices. Such a flip is noted $V_9 \to V_9$. Any flip $V_n \to V_n$ has of course $\widehat{\Delta E} = 0$ and does not change the crystals energy. But if both particles are flipped consecutively, the second flip is $V_9 \to V_8$. As V_8 has a lower energy than V_9 (see fig. 2), this flip sequence does lower the crystal's energy. Although in the end both flip-vertices changed from V_9 to V_8, the total energy change is only $\widehat{\Delta E} = E^{(V_8)} - E^{(V_9)}$ and not $2(E^{(V_8)} - E^{(V_9)})$. There are many other, more complicated correlated flip sequences involved in the phasonic relaxation.

For the dynamic part of the free energy, also called configurational free energy F_c, he approximated the flips as spins in an Ising model without coupling (we call it flip Ising

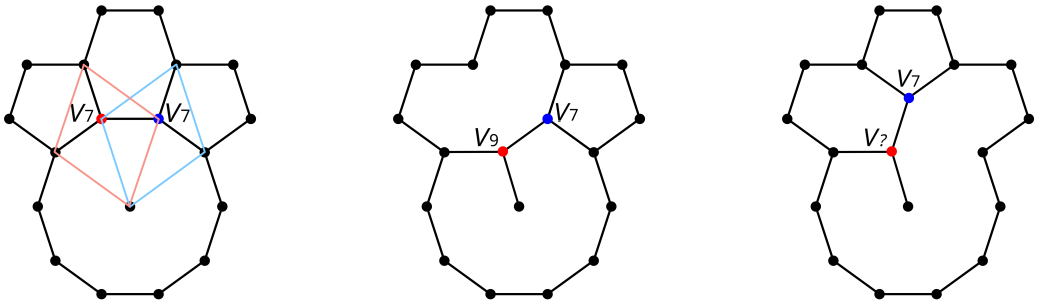

(a) (b) (c)

Figure 34: Two correlated next neighbour flips. In (a) only one particle can perform a flip $V_7 \to V_9$. This is also realized by the overlapping rhombuses. After the left particle flips, the direction and type of the right flip is changed. The right flip $V_7 \to V_7$ then creates a new vertex $V_?$ and a large new tile. Since the distance between the two flip-particles does not change during the second flip, the new vertex must have the same energy as V_9. Flip sequences like this are not taken into account in the flip-Ising model.

model). So each flippable particle has two possible states a and b with energies $E^{(a)}$ and $E^{(b)}$. One state is the particle's vertex configuration V_n in the previously phasonically relaxed crystal for a given $\overline{\boldsymbol{\chi}}$. The other state is its vertex configuration after only that particle flipped. Considering every particle only within the ground state LI-class is a strong approximation. It neglects the consequences that flipping particles have on their neighbouring particles. Another example for a correlation between two successive flips is shown in fig. 34. Other than in fig. 33, these particles are correlated in such a way that they cannot flip simultaneously. A simultaneous flip would create a lattice defect which will not be discussed, as noted earlier. Flipping the two particles after one another, a new vertex is created and a new shape that does not fit into the set of $\mathcal{Q}$-tiles. Continuing such correlated flip sequences, a wide variety of different states would emerge. In the approximation of independent flips, the possible states of an initial configuration as in fig. 34a are just $\{(V_7;V_7),(V_7;V_9),(V_9;V_7),(V_9;V_9)\}$. Nevertheless, the flip Ising model is definitely worth investigating. It is the first approach of a rather simple mathematical description of the flip dynamics that still captures the essential phenomenon of non-homogeneous flip probabilities. It is defined as follows. Unlike $\widehat{\Delta E}$, which can be positive or negative, we define $\Delta E = |E^{(b)} - E^{(a)}| \geq 0$. Now let $k \in \{1,..,K\}$ be an index for the different types of flips. Further, N_k is the number of flippable atoms of type k in a given patch $\mathcal{P}$ with a total of N particles. Because we are only interested in the temperature dependent part of the free energy (E_0 is already obtained from the phasonic relaxation), we assert to each flip atom an energy 0 for the low energy state and ΔE_k for the high energy state. Each microstate of $\mathcal{P}$ is defined by a flip distribution $r = \{S_{km} \in \{0,1\} | k = 1,..,K; m = 1,..,N_k\}$ that labels the two possible states of each flip atom by $S = 0$ and $S = 1$. Then the r-dependent Ising model Hamiltonian reads

$$H_r = \sum_{k=1}^{K} \sum_{m=1}^{N_k} S_{km}^r \Delta E_k. \tag{61}$$

With Boltzmann's constant as $k_\mathrm{B} = 1$, the well known canonical partition function of such a system is found by summing over all possible flip distributions

$$
\begin{aligned}
Z_c(N,T,\boldsymbol{\chi}) &= \sum_r \exp\{-H_r/T\} = \sum_r \prod_{k=1}^{K}\prod_{m=1}^{N_k} S_{km}^r \Delta E_k \\
&= \prod_k \prod_m \sum_{S\in\{0,1\}} \mathrm{e}^{-S\Delta E_k/T} = \prod_k \left(1+\mathrm{e}^{-\Delta E_k/T}\right)^{N_k}.
\end{aligned}
\tag{62}
$$

Then, for the whole infinite crystal with $N \to \infty$, we define flip densities $n_k = \frac{N_k}{N}$. The configurational free energy density F_c of independent flips reads

$$
F_c = -T\frac{\ln Z_c(N,T,\boldsymbol{\chi})}{N} = -T\sum_k n_k \ln\left(1+\mathrm{e}^{-\Delta E_k/T}\right). \tag{63}
$$

Finally, the complete phasonic free energy density is

$$
F(T,\boldsymbol{\chi}) = E_0(\boldsymbol{\chi}) + F_c(T,\boldsymbol{\chi}). \tag{64}
$$

The densities $n_k(\boldsymbol{\chi})$ of flippable atoms and the number $M(\boldsymbol{\chi})$ of different flip types are the only $\boldsymbol{\chi}$-dependent quantities in eq. (63). Kiselev measured the n_k by flipping all flippable atoms in the unit cell of each approximant, noting their type k every time and counting off the N_k. Then dividing by the number N of atoms in the unit cell yields the densities n_k. While counting the flips, he used a certain restriction of allowed and forbidden flips that will now be investigated.

First, he noted that he considers only those flips that originate in a vertex V_7, V_8 or V_9. He explained this by arguing that only a small phasonic strain was applied, which corresponds to a small shift $u^\perp$ of the window in $E^\perp$. So points of the hyperlattice $\mathcal{L}$ should exit and enter $\mathcal{W}$ only close to the boundary. As seen in fig. 32, the boundary regions of $\mathcal{W}$ correspond indeed to V_7, V_8 and V_9. We want to elucidate now why this kind of argument is wrong.

First, note that there are two kinds of phasonic strain present in the method described above. The global phasonic strain $\overline{\boldsymbol{\chi}}$ of a given approximant, which is indeed small and bounded by $|\chi_n^{(1)}| < 0.03$. And secondly the fluctuating phasonic strain $\boldsymbol{\chi}(x^\parallel)$ within a given approximant that corresponds to the thermal flips. Here, it is better to talk about $u^\perp$-fluctuations because different functions $\boldsymbol{\chi}(x^\parallel)$ can correspond to the same function $u^\perp(x^\parallel)$. These local phasonic displacements are bounded by the approximation of independent flips [13]. Every type of single flip in the ideal tiling produces a local phasonic displacement that is characteristic for this type. In the partition sum eq. (62), every single flip has a thermal probability $p^{(b),(a)} = 1/(1+\mathrm{e}^{\pm\Delta E/T})$ to be in state a or b. These probabilities are completely independent of the global phasonic strain $\overline{\boldsymbol{\chi}}$. They can also not depend on the local $u^\perp(x^\parallel)$-fluctuations, because these fluctuations are merely a mathematical description of the flips. All physically significant arguments must root in the flips themselves, regardless of their embedding in some abstract hyperspace. The individual flip probabilities are solely dependent on the energy differences ΔE, which originate in the LJG-potential, which, by itself, has nothing to do with the whole CPS. So in principle, all flips are possible for any $\overline{\boldsymbol{\chi}}$.

[13] It is not mentioned exactly which of the two types of phasonic strain Kiselev's argument refers to. But the global phasonic strain $\overline{\boldsymbol{\chi}}$ produces certainly unbounded $u^\perp$-shifts, since $|\overline{u}^\perp| = |\overline{\boldsymbol{\chi}}x^\parallel| \to \infty$ for $|x^\parallel| \to \infty$, no matter how small $\overline{\boldsymbol{\chi}}$ is.

Similarly, Kiselev's second flip restriction also has no physical grounds. For the phasonic relaxation, he allowed only such flips that do not create any new vertex types. Not only the flipping atoms themselves, but all vertices in the whole tiling must always be in the set $\{V_1, ..V_9\}$. We assume that he also used this restriction for counting the flip numbers N_k. There, he wrote that only such flips are counted that do not lead to a tiling defect. We believe that here, 'tiling defects' again refers to vertices that are not part of the ideal $\mathcal{Q}_{\mathrm{TTT}}$ because the word 'defect' was used this way in other sections of his thesis. Also note that 'tiling defect' cannot refer to such distortions that we defined above as 'lattice defects' because flips can never change the shape of the triangle tiles. Unfortunately, it was not explained in his thesis why such a strong restriction to the tiling ensemble would be appropriate. But considering the variety of vertices in fig. 27a and 28, it is clear that the crystal in the MD-simulation was certainly not subject to any such conditions.

Although Kiselev's arguments to ignore certain types of flips are not convincing, the first restriction to consider only V_7, V_8 or V_9-flips turns out to be a legitimate approximation. The reason is that the V_4, V_5 and V_6-vertices are quite stable. Also, any flip originating in one of these vertices results in a configuration of much higher energy. Then, $\Delta E \gg 0$ makes such flips very unlikely and their contribution to F_{flip} neglectable.

In general, the closer the acceptance domain of a vertex type V_n lies to the center of $\mathcal{W}$, the more stable is that vertex. This is not at all obvious but rather seems to be a remarkable coincidence. The CPS that defines the positions of the AD in $\mathcal{W}$ and the LJG-potential that determines the vertices energies are mathematically independent concepts. Still, one possible connection can be seen in the fact that the vertices with AD closer to the center, at least V_1, V_2 and V_3, are more symmetric than the others, which is usually an advantage for stability. Yet, it is not explained why any flip from a stable configuration V_4, V_5 or V_6 should always result in a much less stable configuration. It might be the case that this holds just due to the approximation of the flips being launched only from the ground state LI-class. This limits the variety of larger environments surrounding the V_n-vertices and therefore the variety of flip types, compared to a true RT.

4 The Polar Calculus and Phasonic Flips

In this section, it will be explained how the polar calculus is applied on $\mathcal{Q}_{\mathrm{TTT}}$ and on phasonically distorted, aperiodic crystals $\mathcal{Q}(\boldsymbol{\chi})$. Also, the flips with and without Kiselev's restriction are compared. Furthermore, two models of treating two correlated nearest neighbour flips are presented.

4.1 Acceptance Domains with Phasonic Strain

$\boldsymbol{d} \in \mathcal{H}$	$d^{\perp} \in E^{\perp}$	$d^{\parallel} \in E^{\parallel}$
$\frac{1}{2}(\widetilde{\boldsymbol{a}}_0 + \widetilde{\boldsymbol{a}}_1 - \widetilde{\boldsymbol{a}}_2 + \widetilde{\boldsymbol{a}}_3 - \widetilde{\boldsymbol{a}}_4)$	$(0, \sqrt{\frac{2}{5}}\tau)$	$(0, \sqrt{\frac{2}{5}}\frac{1}{\tau})$
$\frac{1}{2}(-\widetilde{\boldsymbol{a}}_0 + \widetilde{\boldsymbol{a}}_1 - \widetilde{\boldsymbol{a}}_2 + \widetilde{\boldsymbol{a}}_3 - \widetilde{\boldsymbol{a}}_4)$	$(-\sqrt{\frac{\tau}{2\sqrt{5}}}, \frac{\tau^2}{\sqrt{10}})$	$(-\sqrt{\frac{1}{2\sqrt{5}\tau}}, -\frac{1}{\sqrt{10}}\frac{1}{\tau^2})$
$\frac{1}{2}(-\widetilde{\boldsymbol{a}}_0 + \widetilde{\boldsymbol{a}}_1 - \widetilde{\boldsymbol{a}}_2 + \widetilde{\boldsymbol{a}}_3 + \widetilde{\boldsymbol{a}}_4)$	$(-\sqrt{\frac{\tau^3}{2\sqrt{5}}}, \frac{1}{\sqrt{10}})$	$(\sqrt{\frac{1}{2\sqrt{5}\tau^3}}, -\frac{1}{\sqrt{10}})$

Table 3: Three of the corners of the windows, represented in different spaces. The other corners are found simply by all possible x- and y-reflections of these.

The AD of any atom configuration $C = \{v_i^{\parallel}\}$ in $\mathcal{Q}_{\mathrm{TTT}}$, with positions given as vectors in $E^{\parallel}$ is computed as follows. First, the atom positions are written in the basis $\{a_j^{\parallel}\}$. The vectors $\boldsymbol{a}_j$ were introduced in section 3.1.1 as a 5D basis of the root lattice $\mathbb{A}_4$. Their $E^{\parallel}$-projection is found via the projection operator $\mathbf{P}^{\parallel}$ of eq. (40). Having written the atoms' position vectors like

$$v_i^{\parallel} = \sum_j c_j^{(i)} a_j^{\parallel} \quad (c_j^{(i)} \in \mathbb{Z}), \tag{65}$$

the corresponding position $v^{\perp}$ in $E^{\perp}$ is found simply by replacing $a_j^{\parallel}$ by $a_j^{\perp}$. Then, the window is attached to each $E^{\perp}$-position with $v^{\perp}$ marking the center. $\mathcal{W}$ is easiest parameterized by its corners $d_i^{\perp}$, $i = 1, .., 10$. These corners are $E^{\perp}$-projections of some of the corners $\boldsymbol{d}_i$ of the root lattice's Voronoi cell. They are written explicitly in table 3 together with their $E^{\perp}$- and $E^{\parallel}$-projections. The AD of the atom configuration C is then the intersection of all these windows

$$\overline{C} = \bigcap_i (v_i^{\perp} + \mathcal{W}). \tag{66}$$

The intersection area of all the windows at different positions can be calculated through triangulation. This is in principal always possible to do by hand, but of course it gets quite tedious with many windows. Using the geometry package *shapely* for *python* each window can be defined as a polygon and their intersection computed automatically.

Fig. 35c shows the construction of the AD of the vertex environment V_8 for a certain orientation. For the AD of vertex environments V_8 and V_9, not only intersections, but also complements of windows must be considered. That's because they don't fill the circle of radius $r_c = 2$ with the maximally possible number of atoms. This information that a certain position is not occupied by an atom, even though it could be, is taken into account by subtracting the window of this hypothetical atom. The AD is constructed with respect to one reference atom, whose position is placed in the origin during the construction. In this case, it is the central atom of V_8. It means that the position of

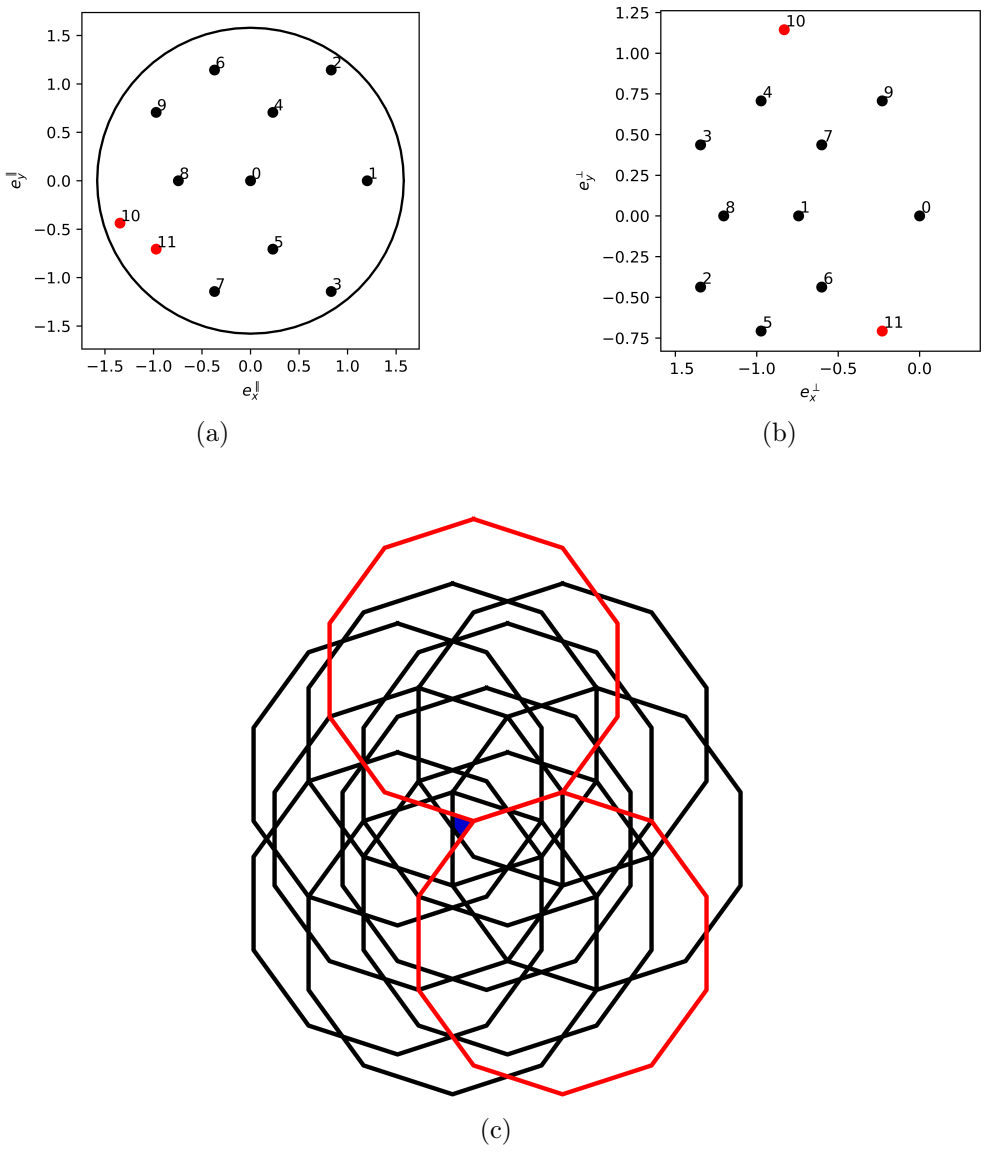

Figure 35: (a) Black dots: Vertex environment V_8. Red dots: Positions where additional atoms would be possible using an acute or obtuse triangle tile in the right orientation. With additional points the vertex type would be V_7 or V_6. (b): Corresponding points in $E^{\perp}$. The small numbers label $E^{\perp}$-points and $E^{\parallel}$-points belonging to the same $\mathcal{H}$-point. (c): A window is attached to each point of (b). The intersection of the black windows and complement of the red windows is the AD of V_8.

the AD is considered within the window of this reference atom (the right most decagon in fig. 35c). Thereby, every $\mathcal{L}$-point that is $\mathbf{P}^{\perp}$-projected into this AD will also be the center atom of a V_8-environment in $\mathcal{Q}$. If we want to distinguish atoms of different environments without ambiguity, the ADs should be constructed with respect to the same reference position. Otherwise the ADs could overlap. An atom might simultaneously be in the center of a V_1-configuration and on the right most position of the V_8-configuration of fig. 35a. But it cancgnnot simultaneously be in the center of both configurations, or on the right most side of both configurations. Hence, ADs of the same reference atom

are disjoint. Constructing the ADs of all other V_n analogously with the central atom as reference, they create the subdivision of the window of fig. 32.

This process can be extended to phasonically distorted crystals, noted $\mathcal{Q}(\boldsymbol{\chi})$. Two processes must be taken into account. Firstly, the corners $\boldsymbol{d}_i$ of the $\mathbb{A}_4$-Voronoi cell are shifted. In general, a phasonic strain could change which of the Voronoi corners end up as the window corners and which are projected somewhere in the interior of $\mathcal{W}$. But for $|\chi_n^{(1)}| < 0.03$, $n \in \{6, 8\}$ this does not happen. The window remains a convex, but not exactly regular decagon (see fig. 36). So the corners of the phasonically distorted window $\mathcal{W}(\boldsymbol{\chi})$ are given by

$$d_i^{\perp}(\boldsymbol{\chi}) = d_i^{\perp} + \boldsymbol{\chi} d_i^{\parallel}, \qquad i = 1, .., 10. \tag{67}$$

As explained in section 3.1.2, the components $\chi_n^{(1)}$, $n \in \{6, 8\}$ are sufficient to calculate the phason elastic constants λ_6, λ_8. Hence, the phasonic strain tensor in this thesis will be either

$$\boldsymbol{\chi} = \frac{\chi_6^{(1)}}{\sqrt{2}} \begin{bmatrix} 1 & 0 \\ 0 & -1 \end{bmatrix} \quad \text{or} \quad \boldsymbol{\chi} = \frac{\chi_8^{(1)}}{\sqrt{2}} \begin{bmatrix} 1 & 0 \\ 0 & 1 \end{bmatrix}. \tag{68}$$

From now on the simpler notation χ_6 and χ_8 shall be used and always refer to the $\chi_6^{(1)}$ and $\chi_8^{(1)}$-components. Also, for some $\boldsymbol{\chi}$-dependent quantity, like the free energy F, we shall write $F(\chi)$ to express a dependency on only χ_6 or only χ_8 with the other component being zero. The hyperlattice points corresponding to the atom positions are shifted in the same manner as the Voronoi-corners. So in a CPS crystal of small but variable phasonic strain, eq. (66) is generalized to

$$\overline{C}(\boldsymbol{\chi}) = \bigcap (v_i^{\perp} + \boldsymbol{\chi} v_i^{\parallel} + \mathcal{W}(\boldsymbol{\chi})). \tag{69}$$

The window, subdivided into the ADs of the vertex configurations V_n, is shown in fig. 36 once with phasonic strain $\chi_8 = 0.03$ and once with $\chi_6 = 0.03$. Compared to the QC-window in fig. 32, the ADs in $\mathcal{W}(\boldsymbol{\chi} \neq \mathbf{0})$ change their size and form. Also, they are not symmetric anymore. This means that differently oriented, but else identical, atom configurations have different densities. The grey area in the χ_8-distorted window is the AD of a new vertex type that is present in any crystal $\mathcal{Q}(\chi_8 > 0)$, but not in $\mathcal{Q}(0)$. The new vertex type may be called V_{10}. In his dissertation, Koschella found a vertex configuration in a binary crystal, which he labeled V_{40}, and, which is identical to V_{10} if one of the two atom types is ignored. V_{10} is also a flipable vertex and its potential energy is equal to that of V_6. The atom arrangement of V_{10} is seen in section 8.3.

Fig. 37 shows the relative densities $\rho_{V_n}(\chi) - \rho_{V_n}(0)$ of the V_n-vertices as functions over χ_6 and χ_8, calculated with the polar calculus. In the short χ-interval shown, they are pretty much perfect parabolas. The curves are only correct for every χ-value that corresponds to an aperiodic crystal. For any periodic approximant, the polar calculus formalism is i.g. not exact. The actual density $\widehat{\rho}$ of any atom configuration in an approximant will have smaller or larger deviations from the densities obtained using the polar calculus. It depends on how good the ratio of a certain AD-area over the area of $\mathcal{W}(\boldsymbol{\chi})$ approaches the ratio of the number of $\mathcal{L}^{\perp}$-points in that AD over the number of $\mathcal{L}^{\perp}$-points in $\mathcal{W}(\boldsymbol{\chi})$. The latter ratio is how the true density $\widehat{\rho}$ can be calculated.

The polar calculus density functions $\rho(\chi)$ of fig. 37 of any atom configuration are clearly continuous, being nothing but intersection area of continuously shifted polygons. Let us

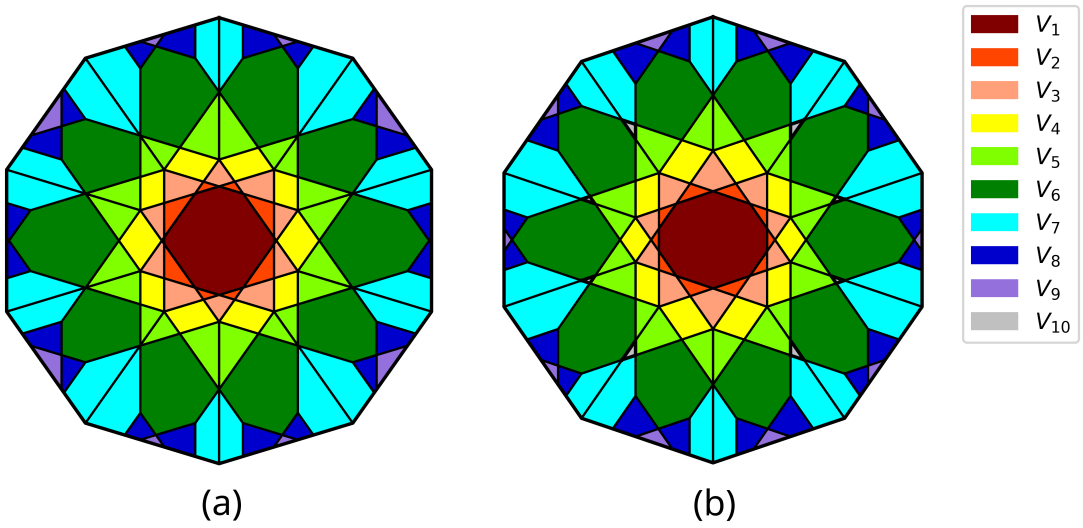

Figure 36: Window of a phasonically distorted crystal $\mathcal{Q}(\boldsymbol{\chi})$. (a): $\chi_6 = 0.03$, $\chi_8 = 0$. (b): $\chi_6 = 0$, $\chi_8 = 0.03$. Here, a new vertex type V_{10} appears. The windows are no longer regular decagons. The phasonic strain also deforms $\mathcal{W}$, but for small χ, this change is hardly visible. A strongly deformed window is seen in appendix 8.2.

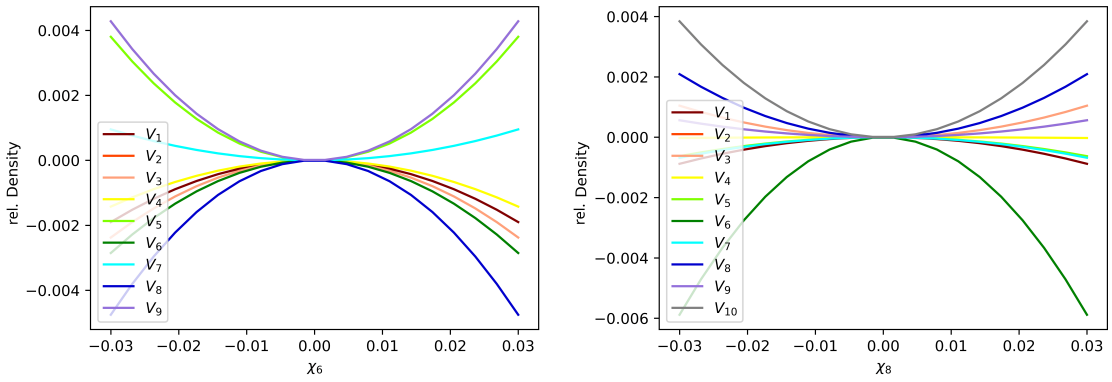

(a) (b)

Figure 37: Relative vertex densities $\rho(\chi) - \rho(0)$ over phasonic strain. The curve of V_2 is not visible because it is identical to the one of V_9.

call the χ-values that produce approximants χ_p, and the ones that produce aperiodic crystals χ_ap. Then, it is $\widehat{\rho}(\chi_\mathrm{ap}) = \rho(\chi_\mathrm{ap})$ and $\widehat{\rho}(\chi_p) \neq \rho(\chi_\mathrm{p})$. In appendix 8.2, it is shown that the sets $\{\chi^{(1)}_{6,\mathrm{p}}\}$, $\{\chi^{(1)}_{8,\mathrm{p}}\}$ are countably infinite and dense in $\mathbb{R}$. This means that the true density function $\widehat{\rho}(\boldsymbol{\chi})$ must be discontinuous in every point χ_p and, due to the density of $\{\chi_\mathrm{p}\}$, also in every point χ_ap. Then also the phasonic free energy F, which is just a linear combination of density functions, is totally discontinuous over $\mathbb{R}$, but continuous over $\{\chi_\mathrm{ap}\}$. It is also discussed in the appendix that the free energy restricted to the domain of approximants, $F|_{\{\chi_\mathrm{p}\}}$, is also discontinuous everywhere.

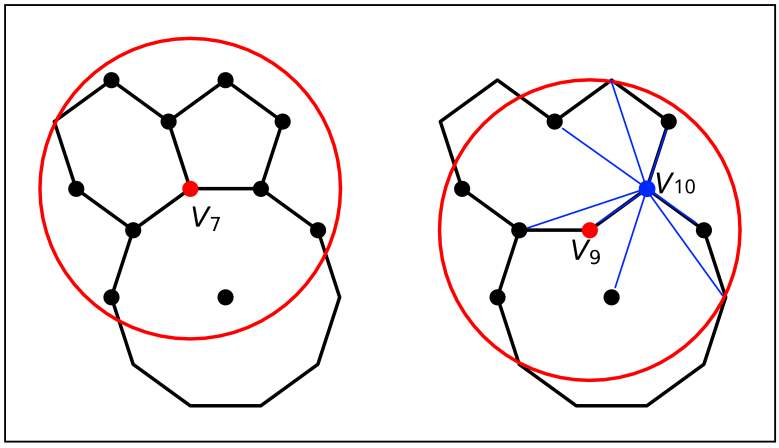

Figure 38: A flip $V_7 \to V_9$ can be realized by this tile combination. The cluster is large enough to determine the particle's energy before and after the flip. In the configuration on the right, a new vertex type V_{10} shows up. It is not important for the flip energy, but it means that this kind of flip was 'forbidden' in Kiselev's flip restriction.

So our initial assumption of $F(\boldsymbol{\chi})$ being an analytical function is actually wrong. It can only be analytical on the set $\{\chi_{\mathrm{ap}}\}$. While the free energy of only aperiodic crystals is still interesting, one might still wonder how significant the deviations between $F|_{\{\chi_{\mathrm{p}}\}}$ and $F|_{\{\chi_{\mathrm{ap}}\}}$ are. It can be shown that $\rho(\chi_6, \chi_8) \to \widehat{\rho(\mathbf{0})}$ as χ_6 and χ_8 go to zero (again see appendix 8.2). So at least in a sufficiently small interval around $\boldsymbol{\chi} = \mathbf{0}$, the fluctuations of $F|_{\{\chi_{\mathrm{p}}\}}$ around $F|_{\{\chi_{\mathrm{ap}}\}}$ should be adequately bounded. As any small but non-zero χ-interval is enough to compute the phasonic constants $\lambda_n = \partial_{\chi_n} F|_{\chi_{ap}}$, they will predict the QC stability around $\chi = 0$ not only on $\{\chi_{\mathrm{ap}}\}$, but also on $\mathbb{R}$. How well $F_{\{\chi_{\mathrm{ap}}\}}$ can predict stability of other crystals $\mathcal{Q}(\boldsymbol{\chi} \neq \mathbf{0})$ shall not be our concern. For larger χ-values one may recall Engel's plot of $E_0|_{\{\chi_{\mathrm{p}}\}}$ (fig. 30b) and find that, although it must be discontinuous everywhere, it looks fairly well-behaved, apart from the regions around the Xi-approximants [14] . Later we will compare our results for $E_0|_{\{\chi_{\mathrm{ap}}\}}$ to this figure and also $F|_{\{\chi_{\mathrm{ap}}\}}$ to the results of Kiselev.

4.2 Single Flips

4.2.1 Flip Types and Flip Counting

Using the short cutoff radius $r_c = 2$, the potential energy of any atom is completely defined by its vertex environment V_n. A flip is characterized by the initial and final vertex type ,V_i and V_f, of the flipping atom. For flips in thermal equilibrium, it does not matter which state is chosen as V_i and which one V_f. For the phasonic relaxation, it does matter. Then, V_i will be the atom's configuration that the particle has in the original CPS-tiling with constant strain $\mathcal{Q}(\boldsymbol{\chi} = \overline{\boldsymbol{\chi}})$, and the flip happens only if $E^{(V_f)} < E^{(V_i)}$. This type of tiling and its LI-class shall be called the *flat tiling* or *flat LI-class* of a given GPS-class. Either way, if a flipable particle is in some configuration V_i, its second state V_f for a hypothetical flip can be found just from inspecting a sufficiently large atom environment surrounding V_i. One can simply imagine how this larger environment would look after a flip, and what the particle's new vertex type would be.

[14] Of course he computed E_0 only for several specific $\boldsymbol{\chi}_{\mathrm{p}}$-points, but they lie in a rather close mesh so that it seems legitimate to assume that there are no discontinuities in between.

Fig. 38 shows again the flip $V_7 \rightarrow V_9$ that was already mentioned in fig. 34. The interaction radius of the particle before and after the flip is explicitly shown. The configuration of D-, H-, and P-tile is enough to know all the atoms in the circle in either flip state. Note that, although the circle is not completely covered by $\mathcal{Q}$-tiles, no atoms were missed. Any further atoms would have to connect to this cluster via one of the triangle tiles, whereby they would always be placed outside of the circle.

Inspecting the surrounding environment of the flip vertices is also how one can identify flips that produce a new vertex type. According to Kiselev's flip restriction, the $V_7 \rightarrow V_9$ flip is actually 'forbidden'. From fig. 38 alone, we can tell that the blue atom cannot have vertex type $V_1, .., V_9$. The blue atom's interaction circle would include all atoms marked by blue lines and perhaps more on the right side that are not shown. Firstly, the blue atom must be a flippable vertex type, as it clearly has the rhombus environment. So assuming that it would be one of $V_4, .., V_9$, its neighbour atoms in the N-tile constitute a shape that is only present in V_5. But V_5 would have two P-tiles attached to that N-tile, which is not possible for the blue vertex due to its neighbour atoms in the U-tile. So it must be a new vertex type. Further properties of the new vertex are not so important as it has no impact on the flip energy $\Delta E = E^{(V_9)} - E^{(V_7)}$. But still, using the polar calculus, it can be shown that the gap on the right side of the blue vertex is always filled by a P-tile, not only in the QC but in any CPS-crystal $\mathcal{Q}(\chi)$ with $|\chi| < 0.03$. Thereby, we find that the blue atom is actually the V_{10}-vertex that was also found to appear in crystals $\mathcal{Q}(\chi_8 > 0)$.

Although it is not mentioned explicitly in Kiselev's thesis, we strongly assume that he counted the flip numbers $N_k(\overline{\chi})$ in the phasonically relaxed crystal, i.e. the ground state of the corresponding GPS-class. Already before introducing the flip-Ising-model, he mentioned that the initial approximants created by the CPS have forbidden vertices, like V_{10}, which he could change into the TTT-vertices during the phasonic relaxation. Most likely the flip $V_9 \rightarrow V_7$ (from right to left in fig. 38) was part of the phasonic relaxation, since it lowers the energy and eliminates V_{10}. This choice is important because different tilings of the same GPS-class have i.g. different flip densities.

Here, we will instead calculate the flip densities n_k in the flat crystal of the corresponding GPS-class. There is no other choice since we want to compute n_k through the polar calculus, which only works in the flat LI-class. Without inspecting them more closely is not possible to say with certainty which of the two tilings, the flat one or the ground state, is the better option for counting the flips. But the following speculative argument can be made in favour of the phasonically relaxed tiling. Though the ground state will surely be a well ordered tiling, it must not be a fixed, single LI-class. Probably, the ground state consists of several LI-classes that differ only by flips with $\Delta E = 0$. Hence, choosing one of them randomly, which is what happens in the phasonic relaxation, it can at least have a random distribution of $\Delta E = 0$-flips. So flip numbers N_k counted this way may be a better approximation of the flip numbers in a true RT-ensemble [15] than the flat tiling, which has experienced no randomization at all. On the other hand, the disadvantage of the ground state is that it will certainly avoid as many high energy configurations as possible. But at high temperatures, such configurations will be part of the randomized crystal. Then the flip numbers counted in the ground state tiling could be less realistic than the ones counted in the flat LI-class.

[15] Actually, n_k and N_k should be functions of $\boldsymbol{\chi}$ and also T. Then, $N_k(\boldsymbol{\chi}, T)$ should ideally be computed as the thermodynamic average of the $N_k^{(i)}$ of all tilings in the GPS-class.

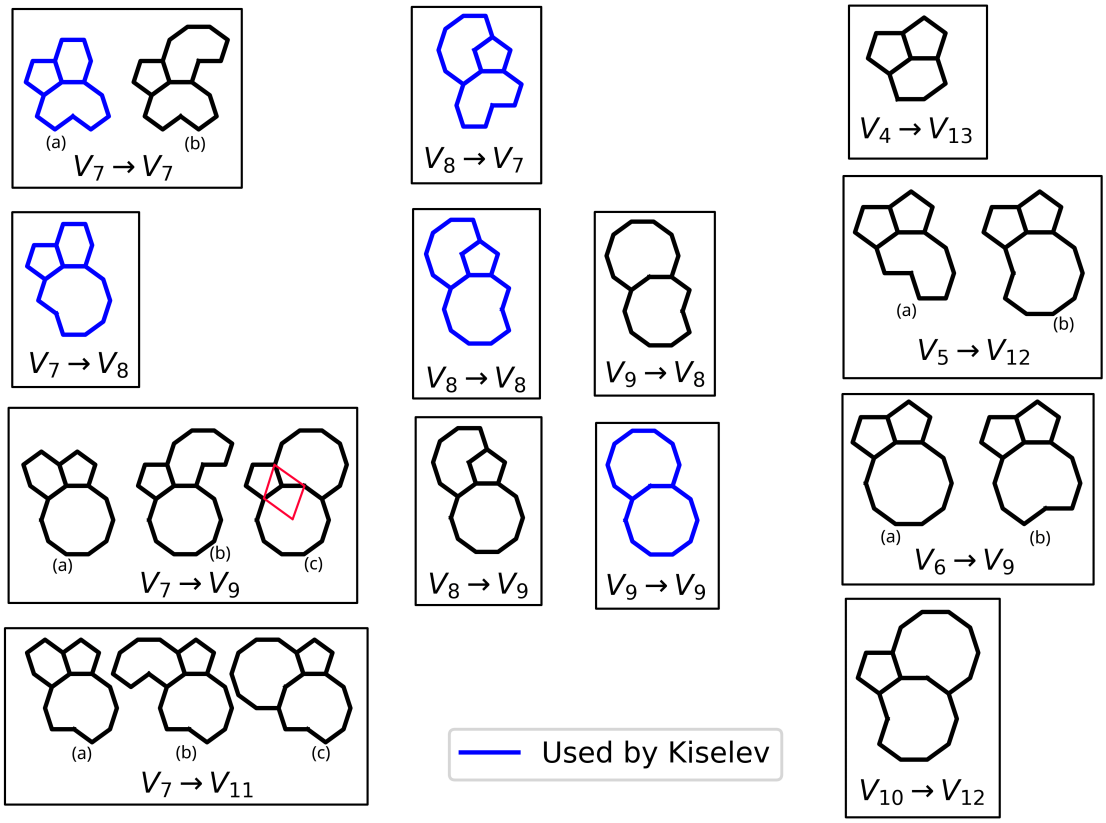

Figure 39: All possible initial flip configurations in the CPS crystals $\mathcal{Q}(|\chi_n| < 0.03)$, $n \in \{6, 8\}$. The flip orientation is shown by the small rhombus in $\mathcal{F}(7, 9)_c$. For some flips $\mathcal{F}(i, j)$, there are several tile combinations labeled (a), (b), etc.

All possible single flips that can happen in any flat crystal $\mathcal{Q}(\chi_n)$ with $|\chi_n| < 0.01$, $n \in \{6, 8\}$ are shown in fig. 39. Let us now use the shorter notation $\mathcal{F}(i, j)$ for a flip $V_i \to V_j$. Analogous as explained for $\mathcal{F}(7, 9)_a$ above, all the flips where checked of whether they fit into Kiselev's flip selection rule or not. Only the ones shown in blue are 'allowed' flips according to the selection rule. Note that $\mathcal{F}(9, 8)$ is considered 'forbidden' as a thermal flip even though it produces no forbidden vertices. That's because in the ground state tiling that Kiselev used these flips were surely in their low energy state V_8. Flipping it back would produce the forbidden vertex V_{10}, analogously as in the example above. So avoiding them is the closest we can get to pretend the system was in ground state. The flip $\mathcal{F}(8, 7)$ also lowers the energy but neither state has forbidden vertices.

For some flips $\mathcal{F}(i, j)$ of fig. 39, there are up to three version that have different combinations of $\mathcal{Q}$-tiles. The most important distinction thereby is between the two versions of $\mathcal{F}(7, 7)$, which are called $\mathcal{F}(7, 7)_a$ and $\mathcal{F}(7, 7)_b$. Only $\mathcal{F}(7, 7)_a$ respects the flip selection rule, while $\mathcal{F}(7, 7)_b$ creates new vertices and even a new tile.

In some clusters of fig. 39, not only the vertices around the flipping particle but also the vertex configuration of the flipping particle itself will not be one of $V_1, .., V_9$ after the flip. The new vertex types that emerge this way are called V_{11}, V_{12} and V_{13}. Their potential energies are $E^{(V_{11})} = -9.3394$, $E^{(V_{12})} = -7.8678$, $E^{(V_{13})} = -6.7365$. The energies of V_{12} and V_{13} are very high compared to the vertices $V_1, .., V_{10}$, making flips that result in

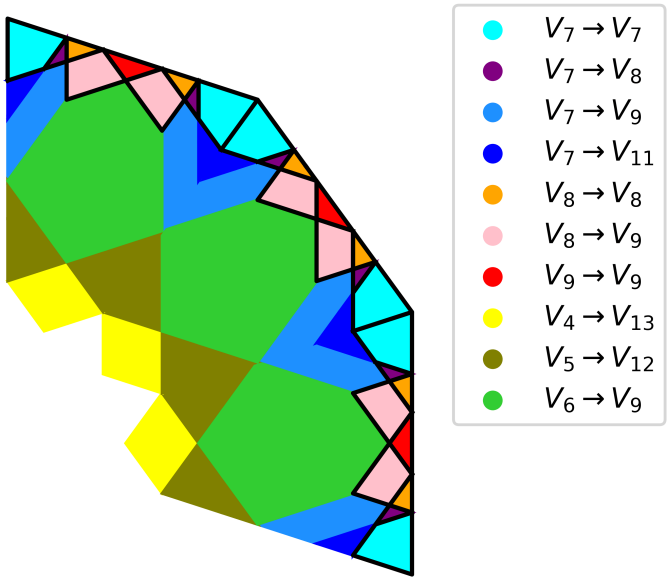

Figure 40: Flip ADs in the ideal QC. The areas outlined in black correspond to flips that where used by Kiselev.

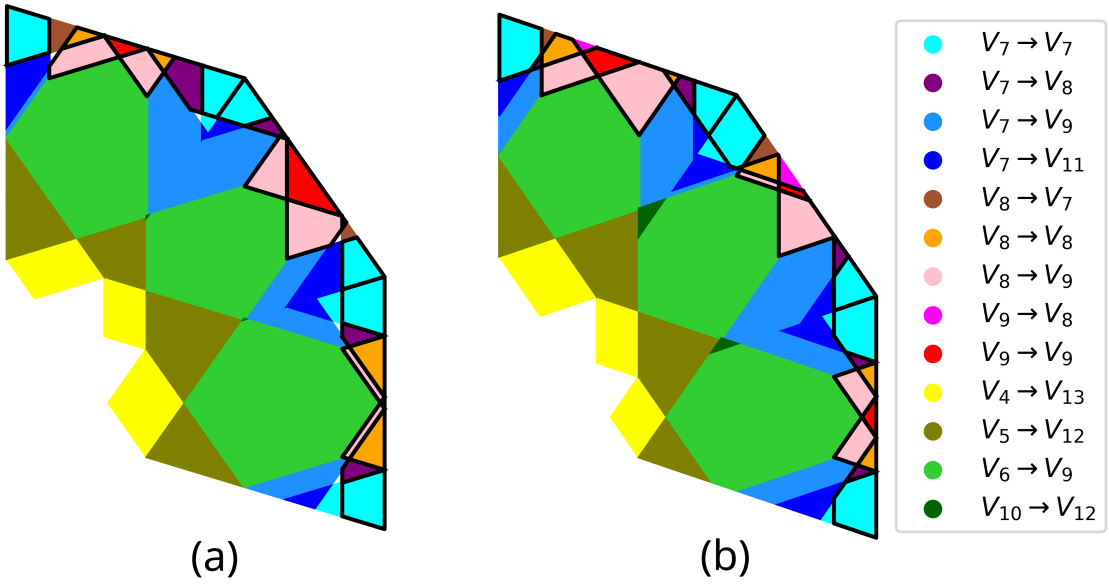

Figure 41: Flip ADs in the phasonically distorted QC. (a): $\chi_6 = 0.03$; (b): $\chi_8 = 0.03$. Tiny white areas in (a) appear only for $\chi_6 > 0.01$.

states V_{12}, V_{13} very unlikely for temperatures T below the melting temperature T_m.

4.2.2 Flip Acceptance Domains

The AD of a flip configuration as in fig. 39 can be found in exactly the same way as the ADs of the vertices V_n. But instead of intersecting the windows of every single atom, it is easier to first compute the ADs of the $\mathcal{Q}$-tiles, then arrange them accordingly in $E^\perp$ and obtain their intersection. In this arrangement, the flip atom of each configuration

was chosen as the reference atom and placed at the origin. Since in the flippable vertices $V_4, .., V_9$ the flip atom was also the reference atom, their ADs overlap with those of configurations of fig. 39, i.e. the V_n-ADs are decomposed into the flip-ADs. We will call the combined ADs of $V_4, .., V_9$ the *flip window* of a given orientation. It is shown in fig. 40 for $\boldsymbol{\chi} = \mathbf{0}$ and in fig. 41 for $\chi = 0.03$ with three orientations. In the QC, where all orientations of any atom configuration are equivalent, one orientation of the flip window would already contain all the information about the flip densities $n_k(\boldsymbol{\chi} = \mathbf{0})$. In $\mathcal{Q}(\chi)$ this is not the case anymore. But still, three segments of the decagon capture the phasonic deformation effect of $\mathcal{W}(\chi)$ completely. This is simply because the phasonic strain matrices in $\chi_6^{(1)}$ and $\chi_8^{(1)}$-direction commute with the reflection matrices in x and y-direction (see section 3.1.2). So all other orientations of the flip window are exactly the reflections of the flip windows in fig. 41. The pictures show again which flips where used by Kiselev (black outlined areas) and which not. Note that the black boundaries of Kiselev's flips cut off a part of the $\mathcal{F}(7,7)$ flips. These cut off areas correspond to $\mathcal{F}(7,7)_b$ in fig. 39.

The flip window of $\mathcal{Q}(\chi_6)$ has some small white areas which are not labeled. They vanish for $\chi_6 < 0.01$, hence their density function $\rho(\chi_6)$ is not parabolic. Eventually we are only interested in calculating the phasonic constants $\lambda = \partial_\chi^2 F(\chi)|_{\chi=0}$. For the ground energy, this is achieved directly by a parabolic fit to $E_0(\chi)$, discussed later. For the configurational free energy, a parabola will be fitted to all the individual flip density functions that constitute $F_c(\chi)$. Any non-parabolic contributions that occur only at larger χ-values would distort our result for the phasonic constants. These flips are beyond the second-order approximation of $F(\boldsymbol{\chi})$ from section 3.1.2. That's why for calculating $\partial_\chi^2 n_k|_{\chi=0}$, we will restrict the parabolic fit to the interval $|\chi| < 0.01$. Nevertheless, we will also compute F up to $\chi = 0.03$, but only for comparison with Kiselev's results. Fig. 36 was shown with $\chi = 0.03$ just to show to the deformations of the ADs more noticeably. These new flips that correspond to the white areas are shown in appendix 8.3.

Just as for the vertices densities $\rho_{V_n}(\chi)$, we can compute the flip density functions via eq. (69). Although the true algebraic form of the density of any atom configuration is some complicated fraction of χ-polynomials, in the interval $|\chi| < 0.01$ all the flip densities are almost perfect parabolas. For the parabolic fit we used the python module *scipy.optimize.curve_fit*, which uses the least square method and provides standard deviations of the fit parameters. The curvature fit errors occurred all at least in the fifth decimal place. The resulting curvatures are listed in table 4 up to the forth decimal place.

4.3 Two-Flip Correlations

The flip-Ising model is a strong simplification of the phenomena that are actually happening in a real QC, or in this case in the MD-simulation crystal. In the review letter [64] following Kiselev's work, a physical justification of this approximation was left to be shown. A first step towards a complete assessment of the flip-Ising model might be to compare it to other, more extensive models. Arguably the simplest model that goes beyond the approximation of independent flips will be presented in the following chapters. For reasons explained soon, it may be called the model of two pentagonally coupled flips. Two different ways are presented of how to treat such flip correlations mathematically.

Type	$\partial\chi_6^2 n$	$\partial\chi_8^2 n$	Energy ΔE_k
$\mathcal{F}(7,7)_a$	-22.1717	-8.7318	0
$\mathcal{F}(7,7)_b$	8.4464	5.5280	0
$\mathcal{F}(7,8)$	12.6696	-1.6351	0.3688
$\mathcal{F}(7,9)$	-7.3906	2.8340	2.325
$\mathcal{F}(7,11)$	9.5021	1.2463	1.9562
$\mathcal{F}(8,7)$	8.4464	5.5280	0.3688
$\mathcal{F}(8,8)$	-3.1676	-1.3889	0
$\mathcal{F}(8,9)$	-10.5577	-1.8149	1.9562
$\mathcal{F}(9,8)$	0.0002	4.2704	1.9562
$\mathcal{F}(9,9)$	4.7509	-3.6472	0
$\mathcal{F}(10,12)$	0	4.2704	5.0151
$\mathcal{F}(4,13)$	-1.5836	-0.0294	9.321
$\mathcal{F}(5,12)$	4.2230	-0.6999	6.6024
$\mathcal{F}(6,9)$	-3.1675	-6.5362	3.9123

Table 4: Types of single flips with density curvature and flip energy. Recall that by definition $\Delta E_k \geq 0$.

4.3.1 Pentagon Coupling

As mentioned in section 3.3.2, one effect that is ignored by the flip-Ising model is the fact that two neighbouring flip particles cannot flip simultaneously. In the case of fig. 34, the two nearest neighbour particles are strongly correlated because each particle is a corner point of the other particles flip rhombus. The corners of a flip rhombus must be fixed in order to assure that both flip states are local potential minima. If the rhombus's corner points change then so will the potential energy landscape surrounding the flip particle. Intuitively, it makes sense to build a hierarchy of flip correlations by starting with fully independent flips and considering nearest neighbour interactions in the next level. We also assume that such nearest neighbour coupling must impact the free energy strongly. In general it can lead to variation of the flip energies, variation of the flip directions and even variation of the total number of flippable particles. Other types of two-flip correlations where the coupled particles are further apart (e.g. as in fig. 33) can only change the flip energies.

The nearest neighbour coupling in fig. 34 can also be identified by the fact that the two flip rhombuses are $2\pi/10$-rotations of each other around the bottom anchor point. This kind of nearest neighbour coupling is almost ubiquitous in the crystals $\mathcal{Q}(\boldsymbol{\chi})$. Except for $\mathcal{F}(4,13)$, all flip types in fig. 39 are i.g. part of such a pair of $2\pi/10$-rotated rhombuses. All pairs of flip particles coupled this way follow a common scheme that is seen in fig. 42. There a generic version of coupled particles is shown, which may be imagined embedded in an arbitrary but fixed atom environment. The corners of the two overlapping rhombs create a regular pentagon shape. The two particles, blue and red, are being flipped consecutively again and again. Each flip of the blue particle changes the direction of the red particles flip rhombus and vice versa. All states reached this way are just rotations and reflections of each other. After five flips, the reflected initial configuration is reached. Continuing this sequence, after five more flips the system will again reach its true initial

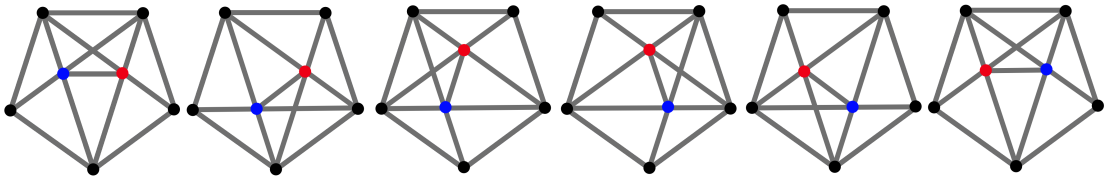

Figure 42: Two nearest neighbour flips are correlated in such a way that one particle is a corner point on the side of the other particle's rhombus. Six consecutive flip states are shown. Each state is related to all other states by some D_{10}-operation. The flip particles can never leave the pentagon that is defined by their rhombuses.

Flip state x_i	Δq_i
1	$(\sqrt{\frac{2}{\sqrt{5}\tau}}, 0)^t = a_0^{\parallel}$
2	$(\sqrt{\frac{\tau}{2\sqrt{5}}}, \frac{1}{\sqrt{2}\tau})^t = -a_3^{\parallel}$
3	$(\sqrt{\frac{1}{2\sqrt{5}\tau^3}}, \frac{1}{\sqrt{2}})^t = a_1^{\parallel}$
4	$(-\sqrt{\frac{1}{2\sqrt{5}\tau^3}}, \frac{1}{\sqrt{2}})^t = -a_4^{\parallel}$
5	$(-\sqrt{\frac{\tau}{2\sqrt{5}}}, \frac{1}{\sqrt{2}\tau})^t = a_2^{\parallel}$

Table 5: The difference of the position vectors of blue and red particle for the first five flip states (fig. 42). Δq_i = red position − blue position. The difference vectors of the other five states are given by $\Delta q_{(i+5)\mathrm{mod}10} = -\Delta q_i$.

configuration. So this two-flip system has a total of 10 different states. Any further surrounding atoms will i.g. change the potential energy of different flip states. But the possible relative positions of the flipping atoms within the pentagon are the same for any further environment. They are listed in table 5. Due to this local symmetry we will call this type of coupling from now on *pentagon coupling* (PC).

For each PC-configuration (atoms arranged as in fig. 42) in a crystal $\mathcal{Q}(\boldsymbol{\chi})$, we want to find its surrounding environment with enough precision to know the energies of all 10 flip states. Of course, switching the two flip particles in a PC-configuration does not change the energy. So there can be at most five non-degenerate flip states. These environments that are sufficiently large to identify all non degenerate states will be called *PC-clusters*. Since the flips shown in fig. 39 are all possible single flips in any crystal $\mathcal{Q}(|\chi| < 0.01)$, each the PC-cluster must contain some combination of these. Further surrounding atoms could be necessary to determine the potential energies of all the states. Luckily, it turns out that this is not the case. All clusters are found simply by adding an extra tile to the single flip configurations. In total, 23 types of PC-clusters were found in the crystals $\mathcal{Q}(|\chi| < 0.01)$. They are shown in fig. 43. A PC-cluster is labeled $\mathcal{F}(i,j)\mathcal{F}(k,l)$, where $\mathcal{F}(i,j)$ is the flip on the left side and $\mathcal{F}(k,l)$ is the flip on the right side, provided that the cluster is oriented such that the common anchor point of the two rhombuses is pointing downwards as in the picture. Note that the cluster $\mathcal{F}(k,l)\mathcal{F}(i,j)$ is just a reflection of $\mathcal{F}(i,j)\mathcal{F}(k,l)$. Only one reflection of each cluster is shown in the picture.

It is remarkable that these relatively small clusters are enough to determine the energies

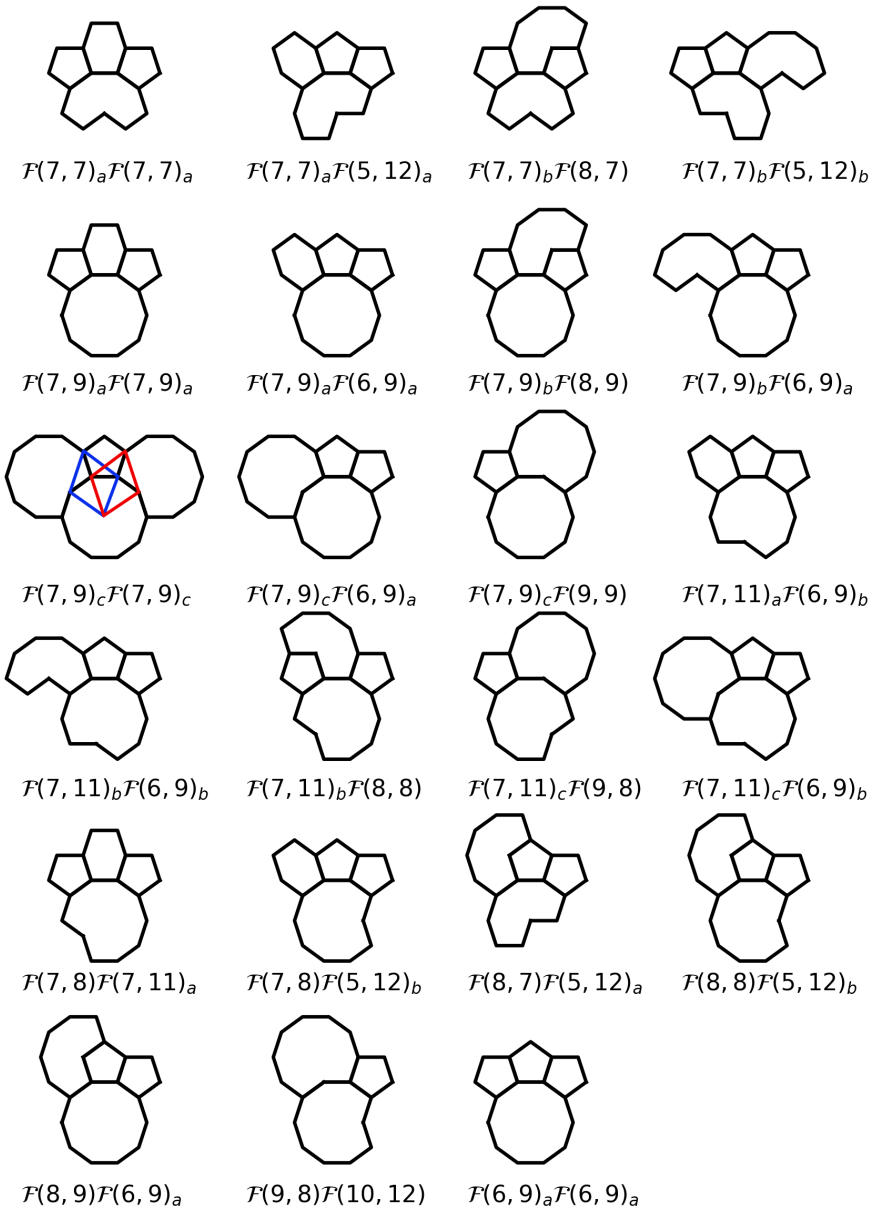

Figure 43: All PC-clusters in CPS-crystals with $|\chi| < 0.01$. The two correlated flips are oriented as shown by the small rhombs in one of the left figures.

of all flip states. The atoms in the cluster must completely fill the interaction circles of both flip particles for all their positions (the positions of the red and blue atom in fig. 42). To show that this is indeed the case, consider one of the most extreme examples, where this rule almost comes to its limit. Fig. 44a shows five consecutive flip states of the PC-cluster $\mathcal{F}(7,7)_a\mathcal{F}(5,12)_a$. Several new tiles are created in this flip sequence. In state 3, 4 and 5 there seems to be a lot of empty space next to at least one of the flipping particles. Fig. 44b shows state 3 with an interaction circle around the critical red particle. If atoms could be added using TTT-tiles in any combination, we could certainly think of a way to fill the interaction circle with more atoms that are not part of the initial PC-cluster. One such example is demonstrated in the picture, using small, green rhombus-tiles, which can be built from two obtuse TTT-triangles. But the PC-cluster is assumed to be placed in a flat CPS-crystal $\mathcal{Q}(|\chi| < 0.01)$. There all atoms are connected only through the five

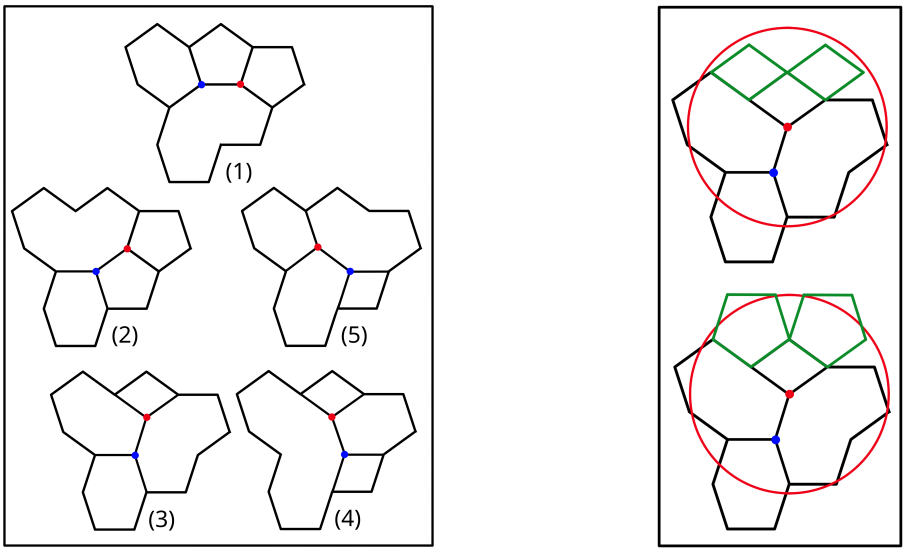

(a) (b)

Figure 44: (a): Five flip states of the cluster $\mathcal{F}(7,7)_a\mathcal{F}(5,12)_a$. Though the two flip particles must follow the regular pentagon pattern as in fig. 42, several states have differing energies due to asymmetric surrounding atoms. (b): The third flip state of (a) with an interaction circle around the red atom. With green rhombs additional points could be placed inside the circle. Below is an attempt using P-tiles. The right P-tile can only add a point at the cost of a lattice defect.

$\mathcal{Q}$-tiles. This can be shown with the polar calculus by covering the ADs of the triangle tiles completely with the ADs of the $\mathcal{Q}$-tiles. It is not hard to see that using the P, H, N, U and D-tiles, no new atoms can be placed inside the circle without creating serious lattice defects. In the picture, two green P-tiles where added demonstratively, which are the smallest $\mathcal{Q}$-tiles. Only the right one would have an additional corner inside the circle, but on the side it creates a gap that cannot be consistently filled with further $\mathcal{Q}$-tiles. So this configuration is not possible. The upper corners of the green pentagons are almost inside the circle. But a trigonometry calculation yields that their distance from the red point is $2.016 > 2$. This example proves also the completeness of many other PC-clusters of fig. 43, like $\mathcal{F}(7,9)_a\mathcal{F}(6,9)_a$ or $\mathcal{F}(8,8)\mathcal{F}(5,12)_a$. The argument applies analogously all other PC-cluster.

The same way we found the ADs of the single flip configurations, we can also compute the ADs of the PC-clusters. The PC-ADs were calculated with respect to one of the flip atoms as reference, so that they lay within the same flip window as the single flips. Then choosing the left or the right flip atom as reference will i.g. create two different but congruent ADs. But these ADs refer to exactly the same PC-cluster, so only one of them was counted in the density function ρ_{pc}. The PC-ADs provide an even smaller subdivision of the flip window, by decomposing the single flip ADs. Actually, the details of this decomposition are not interesting for our purposes. The new ADs should just cover the single flip ADs completely, except for the one of $\mathcal{F}(4,12)$, to proof that all PC-clusters were found. For calculating the phasonic constants, only the curvatures of the density functions of the PC-clusters, $\partial_\chi^2\rho(\chi)$, will be needed. These curvatures are

Type	$\partial_{\chi 6}^2 n^{\mathrm{pc}}$	$\partial_{\chi 8}^2 n^{\mathrm{pc}}$
$\mathcal{F}(7,7)_a\mathcal{F}(7,7)_a$	-22.1717	-8.7318
$\mathcal{F}(7,7)_a\mathcal{F}(5,12)_a$	-22.1717	-8.7318
$\mathcal{F}(7,7)_b\mathcal{F}(8,7)$	8.4463	5.528
$\mathcal{F}(7,7)_b\mathcal{F}(5,12)_a$	8.4463	5.528
$\mathcal{F}(7,8)\mathcal{F}(7,11)_a$	12.6696	-1.6351
$\mathcal{F}(7,8)\mathcal{F}(5,12)_b$	12.6696	-1.6351
$\mathcal{F}(7,9)_a\mathcal{F}(7,9)_a$	-6.3347	11.9433
$\mathcal{F}(7,9)_a\mathcal{F}(6,9)_a$	-6.3347	11.9433
$\mathcal{F}(7,9)_b\mathcal{F}(8,9)$	-10.5577	-1.8149
$\mathcal{F}(7,9)_b\mathcal{F}(6,9)_a$	-10.5577	-1.8149
$\mathcal{F}(7,9)_c\mathcal{F}(9,9)$	9.5018	-7.2944
$\mathcal{F}(7,9)_c\mathcal{F}(7,9)_c$	0	3.8200
$\mathcal{F}(7,9)_c\mathcal{F}(6,9)_a$	9.5017	-11.1144
$\mathcal{F}(7,11)_a\mathcal{F}(6,9)_b$	12.6696	-1.6351
$\mathcal{F}(7,11)_b\mathcal{F}(8,8)$	-3.1676	-1.3889
$\mathcal{F}(7,11)_b\mathcal{F}(6,9)_b$	-3.1676	-1.3889
$\mathcal{F}(7,11)_c\mathcal{F}(9,8)$	0	4.2704
$\mathcal{F}(7,11)_c\mathcal{F}(6,9)_b$	0	4.2704
$\mathcal{F}(8,8)\mathcal{F}(5,12)_b$	-3.1676	-1.3889
$\mathcal{F}(8,9)\mathcal{F}(6,9)_a$	-10.5577	-1.8149
$\mathcal{F}(8,7)\mathcal{F}(5,12)_a$	8.4464	5.528
$\mathcal{F}(9,8)\mathcal{F}(10,12)_b$	0	4.2704
$\mathcal{F}(6,9)_a\mathcal{F}(6,9)_a$	2.1113	-11.5177

Table 6: Curvatures of the PC-cluster densities.

again found by a quadratic fit and are listed in table 6.

4.3.2 Extended Free Energy Model

The pentagonal coupled clusters take into account the correlations between the flips of two neighbouring particles, which results in a total of ten states with at most five different energies. But each PC-cluster is just as independent of the rest of the crystal as the single flips were in the flip-Ising model, introduced in section 3.3.2. Hence the PC-clusters can also be treated as independent 'spins', but with ten states instead of two. Each PC-cluster will be of some type $k \in \{1, .., 23\}$, and each type of cluster has some density $n_k^{\mathrm{pc}}(\boldsymbol{\chi})$, that we obtain from the polar calculus. Furthermore, each state of a PC-cluster has an energy $E_k^{(i)}$. It is simply the sum of the potential energies of the two flip atoms,

$$E_k^{(i)} = \sum_l V_{\mathrm{LJG}}(|r_k^{(l)} - q_i|) + \sum_l V_{\mathrm{LJG}}(|r_k^{(l)} - q_i + \Delta q_i|) + V_{LJG}(|\Delta q_i|), \qquad (70)$$

where $r_k^{(l)}$ are the positions of the surrounding atoms of the type-k PC-cluster, q_i is the position of the blue particle in state x_i and Δq_i are listed in table 5. Because the

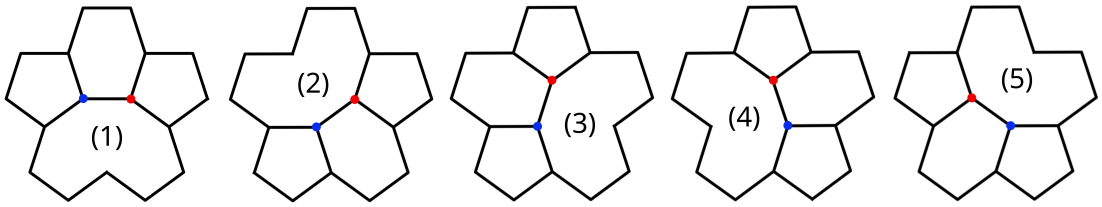

Figure 45: Five flip states of the cluster $\mathcal{F}(7,7)_a\mathcal{F}(7,7)_a$. Due to the pentagonal symmetry of the atom configuration surrounding the flip atoms, all states in this PC-cluster are just rotations and reflections of each other. Hence they are all energetically degenerate.

PC-clusters are complete with respect to the cutoff radius $r_c = 2$, the energy differences $|E_k^{(i)} - E_k^{(j)}|$ of two adjacent states are always equal to the flip energies $|E_k^{(V_i)} - E_k^{(V_j)}|$ as defined in the single flip-Ising model. Only that the PC-clusters will include much more than 13 vertex configurations V_i. These must not be classified in detail. As already in the definition of the single flip configurational free energy F_c, the energies of the PC-states shall be normalized such that the total configurational free energy of PC-clusters vanishes at $T = 0$. So if $E_k^{(\mathrm{g})}$ is the lowest possible energy of a type-k PC-cluster, all states $x_k^{(i)}$ with energies $E_k^{(i)}$ get assigned the effective energy $\Delta E_k^{(i)} = E_k^{(\mathrm{g})} - E_k^{(i)} \geq 0$. The normalized canonical partition sum of one type-k PC-cluster reads

$$Z_k^{\mathrm{pc}} = \mathrm{e}^{E_k^{(\mathrm{g})}/T} \sum_{i=1}^{10} \mathrm{e}^{-E_k^{(i)}/T} = 2 \sum_{i=1}^{5} \mathrm{e}^{-\Delta E_k^{(i)}/T}. \tag{71}$$

The labels (i) are supposed to be ordered like the consecutive flip states in fig. 42, so that we can use $E_k^{(i)} = E_k^{(i+5)\mathrm{mod}10}$. Then the configurational free energy density of PC-clusters in the whole crystal, F_c^{pc}, can be derived completely analogously as for the single flips in eq. (62)

$$F_c^{\mathrm{pc}}(T, \boldsymbol{\chi}) = -T \sum_k n_k^{\mathrm{pc}} \ln Z_k^{\mathrm{pc}}. \tag{72}$$

This extension of single flips to PC-clusters will make a noticeable difference in the free energy and in the phasonic constants. In F_c, the contribution of single flips with large flip energies $\Delta E_k \gg 0$ was neglectable for $T \leq T_m$ since $\ln\bigl(1 + \mathrm{e}^{-\Delta E_k/T}\bigr) \approx 0$. But a PC-cluster with only large flip energies $\Delta E_k^{(i)} \gg 0$ will contribute to F_c^{pc} at least by a term $\propto \ln\left(2 + 2\sum_{i=1}^{4} \mathrm{e}^{-\Delta E_k^{(i)}/T}\right) \approx \ln(2)$, where the proportionality includes the factor $-T$ and the density n_k^{pc} of the corresponding cluster. The PC-model also takes into account the high symmetry of certain clusters. In the single flip model, the flips $\mathcal{F}(7,7)$, $\mathcal{F}(8,8)$, $\mathcal{F}(9,9)$, which have $\Delta E_k = 0$, were all contributing a term $\propto \ln(2)$. Of these symmetric flips, $\mathcal{F}(7,7)_a$ is the only one that can couple to itself. $\mathcal{F}(7,7)_a\mathcal{F}(7,7)_a$ is the most symmetric PC-cluster of all (see fig. 45). Its contribution is $\propto \ln(10)$. For the other symmetric flips, it turns out that the additional states of their PC-clusters, have all quite large potential energies compared to T_m. Hence clusters $\mathcal{F}(8,8)\mathcal{F}(5,12)_b$, $\mathcal{F}(8,8)\mathcal{F}(7,11)_b$ and $\mathcal{F}(9,9)\mathcal{F}(7,9)_c$ will only contribute a term $\sim\propto \ln(4)$.

Note that this PC-free energy density F_c^{pc} is not an additional correction term to the free energy density F_c of single flips. Instead, every single flip of the previous model is already counted in the in the PC-model, except for $\mathcal{F}(4,13)$. The flip $\mathcal{F}(4,13)$ has by

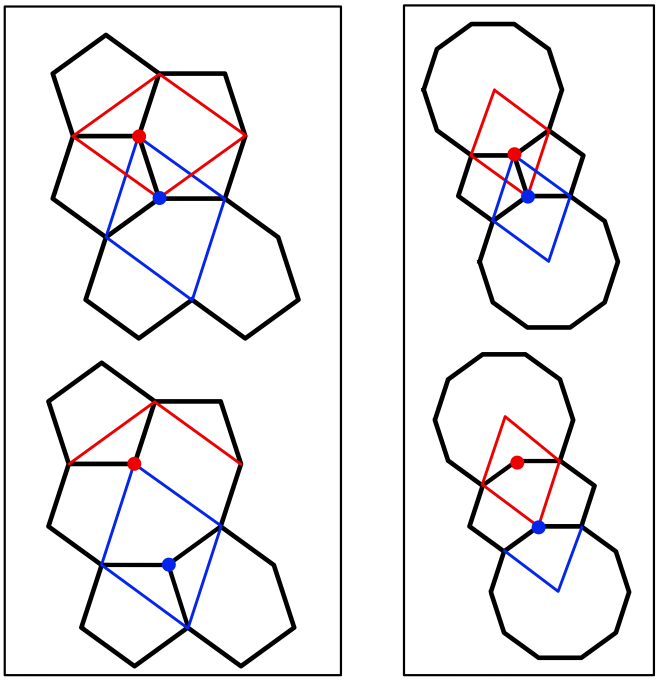

Figure 46: Two examples of restrictively coupled flips. On the left is a coupling of $\mathcal{F}(7,7)_a$ to $\mathcal{F}(4,13)$, where the blue atom, upon flipping, 'destroys' the flip rhombus of the red atom. After the blue flip the red atom has vertex configuration V_3, which is very stable. As the flip $\mathcal{F}(4,13)$ has an extremely small thermal probability this RC-cluster has effectively the same free energy as the single flip $\mathcal{F}(7,7)_a$. On the right is a similar coupling of two $\mathcal{F}(6,9)_a$-flips.

far the highest flip energy ΔE_k and its contribution to F_c or λ_6, λ_8 is essentially zero. Due to its local environment, it cannot couple to other flips in the pentagon style.

4.3.3 Restrictive Nearest Neighbour Coupling

The pentagon coupling is actually not the only way two nearest neighbour flips can be coupled. Two flip rhombuses can also overlap so that the upper corner of one rhombus is the flip atom in the other one. Then, if either atom jumps the other one will no longer be able to flip at all. We might call this kind of nearest neighbour correlation *restrictive coupling* (RC). Two examples are seen in fig. 46. So including the possibility that neither atom jumps, an RC-system of two flips has only three states. Still, its effects on the crystal may be important, but only at higher temperatures. For low temperatures we will demonstrate that, other than for PC-flips, the extension of single flips to RC-flips is not interesting. Looking at the single flips (fig. 39), one can see that if two of them should be restrictively coupled, at least one must be of type $\mathcal{F}(4,13)$, $\mathcal{F}(5,12)$, $\mathcal{F}(10,12)$ or $\mathcal{F}(6,9)$. These all have very large flip energies, with $\Delta E_{\mathcal{F}(6,9)} = 3.9123$ being the smallest. Now consider a free energy model of *RC-clusters* analogous to that of PC-clusters introduced above. If in the single flip model there were two flips with terms $-Tn_a \ln\bigl(1+\mathrm{e}^{-\Delta E_a/T}\bigr)$ and $-Tn_b \ln\bigl(1+\mathrm{e}^{-\Delta E_b/T}\bigr)$ in F_c, where (b) refers to one of the mentioned high energy flips and (a) is any other flip, the RC-combination of these flip would produce a term $-Tn_k^{\mathrm{rc}} \ln\bigl(1+\mathrm{e}^{-\Delta E_a/T}+\mathrm{e}^{-\Delta E_b/T}\bigr)$. For now, let us just compare the logarithm factors of the single flip model and the RC-model. The absolute error of neglecting the RC-effect will be largest if the (b)-flip is $\mathcal{F}(6,9)$, the (a)-flip has flip

energy $\Delta E_a = 0$ and the temperature is $T = T_m = 0.56$. Then the absolute error of the logarithms in the single flip model is

$$\Delta = \left|\ln\left(2 + \mathrm{e}^{-3{,}9123/T_m}\right) - \ln(2) - \ln\left(1 + \mathrm{e}^{-3.9123/T_m}\right)\right| = 4.619 \cdot 10^{-4}.$$

There are 13 flip types k in the single flip model. For an extreme overestimation for the absolute error of the phasonic constants λ_6, λ_8 we may assume $|\partial_\chi^2 n_k| = 20$ for all k (compare the actual values in table 4). Furthermore we pretend that the density of RC-clusters is equal to the denstiy of single flips [16] and use the maximally possible error Δ for each flip. Then still the overestimated error due to neglecting the RC-effect would be

$$\Delta\lambda = 13 \cdot 20 \cdot 4.619 \cdot 10^{-4} = 0.12.$$

From the plots of $\lambda(T)$ in section 5.3 it will be clear that such deviations would change nothing about our results.

So in the temperature regime where the QC is supposed to be stable, the restrictive coupling of only two flips can be neglected. The PC-clusters captures all the significant changes in the phasonic constants due to correlations of two nearest neighbour. Considering correlations between more than two particles, the RC might be more important because then the energy landscape around all the flipping atoms can change more drastically. In general, large numbers of flips correlated over long distances will have tremendous effects on the phase space of a QC and related crystals. For example, several pairs of PC-coupled flips can be placed next to each other. The most obvious example would be a ring of ten P-tiles around a D-tile. Through consecutive flips as shown in fig. 42 all ten flip particles can be interchanged arbitrarily. Then two such ten-flip clusters can also couple and interchange particles. Ultimately, atoms can move arbitrarily far through the crystal only by the means of phasonic flips. This was numerically investigated for the Ammann-Beenker tiling in [65]. Other articles on flip induced diffusion in 2D and 3D QCs are [66, 67]. Also, many of the states that emerge from large clusters of correlated flips will be restrictive, i.e. they decrease the number of possible flips following such a state. Thus, the total density of flippable particles in a crystal $\mathcal{Q}(\chi)$ is actually not constant, as it in the model of PC-clusters.

4.3.4 Markovian Approach to Flip Clusters.

An alternative approach to compute the free energy of flip clusters like the PC-clusters would be via Markov chains. Markov chains are a popular concept of statistical theory with an extremely wide range of applications. Their mathematical background is explained in many books about statistics, probability theory or related topics. A possible introduction to Markov chains is found in chapter 21 of [68], which includes all concepts and theorems that will be used in this section.

The process of particles flipping in a PC-cluster clearly satisfies the *Markovian property*. That is, the probability for an instantaneous transition from one state $x(t)$ to another state $x(t + \Delta t)$ within a fixed, finite time interval of length Δt depends only on the current state. Here, the new state $x(t + \Delta t)$ can be identical to the previous state, since there is no necessity for a particle to flip. The states we are talking about are of course the ten flip states of a PC-cluster. But they are now thought of as separated not only through atom jumps, but also through discrete time steps of length Δt. An

[16] This would mean that all flips are part of two RC-clusters simultaneously. It is of course not true (e.g. the two flips in the right example of fig. 46 can only build one RC-cluster), but the assumption only increases the error. Actually the RC-density is smaller than the flip density.

approximation for the transition probabilities between two states separated by one time step is proposed as follows. Assume some PC-cluster of type k is given in a state $x_k^{(j)}$, $j \in \{1, .., 10\}$. Over time, it may transition into any other state. But in the beginning the only possible options are to stay in $x_k^{(j)}$ (if neither atom jumps), or to transition to state $x_k^{(j+1)\mathrm{mod}10}$ (if the left atom jumps), or to transition to state $x_k^{(j-1)\mathrm{mod}10}$ (if the right atom jumps). In this initial phase, the configuration is just a three level system. Δt should be the time it takes for the system to relax within these first three states, but not further. Then after Δt the whole PC-cluster may be approximately described by the canonical partition function $Z_k^{(j)}$ of this initial three level system

$$Z_k^{(j)} = \mathrm{e}^{-E_k^{(j)}/T} + \mathrm{e}^{-E_k^{(j+1)\mathrm{mod}10}/T} + \mathrm{e}^{-E_k^{(j-1)\mathrm{mod}10}/T}. \tag{73}$$

The superscript j refers to the initial state $x_k^{(j)}$. The potential energies $E_k^{(m)}$, $m \in \{1, .., 10\}$ were defined in eq. (70). Then the probability $p_k^{(j,i)}$ for the transition from state $x_k^{(j)}$ into state $x_k^{(i)}$ is defined as the canonical equilibrium probability of state $X_k^{(i)}$ with respect to the partition sum $Z_k^{(j)}$

$$p_k^{(j,i)} = \frac{\exp\left(-E_k^{(i)}/T\right)}{Z_k^{(j)}}. \tag{74}$$

These expressions fulfill the essential features that are expected from the transition probabilities. The transition into a certain state $x_k^{(j+1)}$ [17] is unlikely if that state has a much higher energy than the current state $x_k^{(j)}$, or if the other neighbour state $x_k^{(j-1)}$ has a much lower energy than both $x_k^{(j+1)}$ and $x_k^{(j)}$. But of course these $p_k^{(i,j)}$ cannot be exactly correct because the time Δt_+ it takes till the probability for a flip $x_k^{(j)} \to x_k^{(j+1)}$ is given by eq. (74) is i.g. different than the time Δt_- it takes till the flip $x_k^{(j)} \to x_k^{(j-1)}$ has occurred with a probability of eq. (74). Also, the whole concept of fixed, discrete transition times is forced onto the system. In reality, flips can happen in arbitrary time distances.

An important question in a Markov process is how the possible states are connected to each other. This is usually depicted in a diagram called the Markov chain. The Markov chain of a PC-cluster is fairly simple as shown in fig. 47. Clearly all states can be reached from each other with a non-zero probability. Also, given any starting state, there is a non-zero probability to reach that state again after any number of time steps. Markov chains with these properties are called *irreducible* and *aperiodic*. Finite, irreducible, aperiodic Markov chains are also known to be *ergodic*. This is the essential requirement for the following calculation.

The occupation probabilities $p_k^{(i)}$ of the 10 possible flip states can be represented in a state vector $\boldsymbol{p}_k = [p_k^{(1)}, .., p_k^{(10)}]^t$. Given an initial state vector $\boldsymbol{p}_k(0)$, the occupation probability of a certain state $x_k^{(j)}$ after one time step is given by

$$p_k^{(j)}(1) = p_k^{(j)}(0)p_k^{(j,j)} + p_k^{(j-1)}(0)p_k^{(j-1,j)} + p_k^{(j+1)}(0)p_k^{(j+1,j)}.$$

This expression is also found by multiplying a *transition matrix* $\mathbf{T}_k$ to the initial state vector $\boldsymbol{p}_k(0)$. The entries of $\mathbf{T}_k$ are the transition probabilities $p_k^{(i,j)}$ and their distribution represents the structure of the Markov chain.

[17] All superscript like $x^{(i\pm1)}$ in this section are supposed to be mod(10).

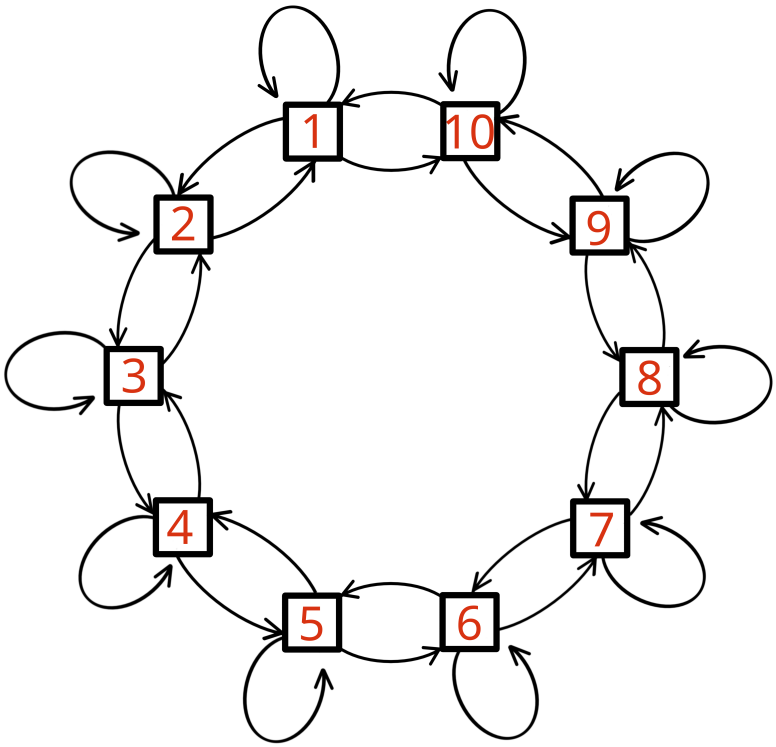

Figure 47: Markov chain of a generic PC-cluster. Each state can transition into itself and into its neighbour states. To each arrow belongs a transition probability $p^{(i,j)}$. States on opposition sites of the decagon have the same energy.

$$\mathbf{T} = \begin{bmatrix} p_k^{(1,1)} & p_k^{(2,1)} & 0 & 0 & 0 & 0 & 0 & 0 & 0 & p_k^{(10,1)} \\ p_k^{(1,2)} & p_k^{(2,2)} & p_k^{(3,2)} & 0 & 0 & 0 & 0 & 0 & 0 & 0 \\ 0 & p_k^{(2,3)} & p_k^{(3,3)} & p_k^{(4,3)} & 0 & 0 & 0 & 0 & 0 & 0 \\ & & & & \ldots & & & & & \\ & & & & & \ldots & & & & \\ & & & & & & \ldots & & & \\ p_k^{(1,10)} & 0 & 0 & 0 & 0 & 0 & 0 & 0 & p_k^{(9,10)} & p_k^{(10,10)} \end{bmatrix} \tag{75}$$

The normalization condition of the new state vector, $\sum_i p_k^{(i)}(1) = 1$, is ensured by the normalization of the matrix columns, $\sum_i p_k^{(j,i)} = 1$. Then in general, the state vector $\boldsymbol{p}_k(n)$ after n steps is given by

$$\boldsymbol{p}_k(n) = \mathbf{T}_k^n \boldsymbol{p}_k(0). \tag{76}$$

Now the ergodicity of the Markov process tells us that for $n \to \infty$, $\boldsymbol{p}_k(n)$ converges towards a unique equilibrium state vector $\boldsymbol{p}_k^{\text{eq}} = \boldsymbol{p}_k(\infty)$. This equilibrium distribution of state probabilities will eventually be reached with arbitrary precision, regardless of the initial distribution. Once the system has reached such an equilibrium distribution, it will stay in it for all times. So $\boldsymbol{p}_k^{\text{eq}}$ must be an eigenvector of the transition matrix

$$\mathbf{T}\boldsymbol{p}_k^{\text{eq}} = \boldsymbol{p}_k^{\text{eq}}. \tag{77}$$

The eigenvalue is of course one due to the normalization of $\boldsymbol{p}_k(n)$. With ideal transition

probabilities $p_k^{(i,j)}$ the occupation probabilities in thermal equilibrium $p_k^{(j)\mathrm{eq}}$ should equal the thermal probabilities $\mathrm{e}^{-\Delta E_k^j}/Z_k^{\mathrm{pc}}$ that are obtained from the canonical partition sum of the PC-cluster, as introduced in section 4.3.2. Later, we will compare the results for the phason elastic constants calculated with these two methods, the Markov chain and the canonical formalism.

The eigenvalue equation (77) can easily be solved numerically. The numerical effort can be reduced by noting again that $E_k^{(i+5)} = E_k^{(i)}$, from which follows $p_k^{(i,j)} = p_k^{(i+5,j+5)}$ and $p_k^{(i)\mathrm{eq}} = p_k^{(i+5)\mathrm{eq}}$. So we just need to diagonalize a 5×5 matrix, that is the upper left block matrix of $\mathbf{T}_k$ with the element $p_k^{(6,5)}$ relabeled as $p_k^{(1,5)}$ and placed in the first column. Then from the eigenvector of this 5×5 matrix, the true equilibrium probabilities $p_k^{(i)}$ differ only by a factor $1/2$. Next, we compute the entropy of the PC-cluster at hand via the well known formula

$$S_k = -\sum_i p_k^{(i)\mathrm{eq}} \ln\Big(p_k^{(i)\mathrm{eq}}\Big). \tag{78}$$

Then the configurational free energy of a type-k PC-cluster is found by considering its temperature derivative at constant volume V and particle number N

$$\Big(\frac{\partial F_{c,k}}{\partial T}\Big)_{V,N} = -S_k. \tag{79}$$

Integrating this equation from $T' = 0$ to $T' = T$ the free energy $F_{c,k}(T)$ is obtained with $F_{c,k}(T = 0) = 0$. The temperature dependent part of the phasonic constants follows analogously as in the Boltzmann formalism.

$$\lambda_n(T) = -T\sum_k \frac{\partial^2 n_k^{\mathrm{pc}}}{\partial \chi_n^2} F_{c,k}(T), \qquad n \in \{6,8\}. \tag{80}$$

Their offset is as always computed from the curvature of the ground state energy $E_0(\chi)$, which will be defined in the next section.

4.4 Analytical Phasonic Relaxation Through Single Flips

The ground state energy density for the model of independent flips is based on the formula for the potential energy density of a flat CPS-crystal $\mathcal{Q}(\boldsymbol{\chi})$ (eq. (59) in section 3.3.1). In some of these crystals, there are atom configurations whose energy can be lowered by a single flip. There are only two types of such configurations, the flips $\mathcal{F}(8,7)$ and $\mathcal{F}(9,8)$. All other flips are already in their low energy state when constructed in a flat crystal. So for the ground state energy, we assign to every atom with a local configuration $\mathcal{F}(8,7)$ the energy $E^{(V_7)}$ and to every atom with configuration $\mathcal{F}(9,8)$ the energy $E^{(V_8)}$. In other words we subtract the energy density $n_{\mathcal{F}(8,7)}E^{(V_8)}$ and replace it by the flipped energy density $n_{\mathcal{F}(8,7)}E^{(V_7)}$, and the same for $\mathcal{F}(9,8)$. Interestingly, such energy lowering single flips only show up for $\boldsymbol{\chi} \neq \mathbf{0}$. The ground state energy density written in terms of vertex densities $\rho_{V_i}(\chi)$ and flip densities $n_{\mathcal{F}(i,j)}(\chi)$ reads

$$E_0(\chi) = \sum_{i=1}^{10} \rho_{V_i} E^{(V_i)} + n_{\mathcal{F}(8,7)}(E^{(V_7)} - E^{(V_8)}) + n_{\mathcal{F}(9,8)}(E^{(V_8)} - E^{(V_9)}). \tag{81}$$

This is most likely not the true ground state energy of any such crystal $\mathcal{Q}(\chi)$. Surely, the energy can be lowered more by including the effect of correlated flips. One example of two correlated flips that can further lower the energy was discussed in section 3.3.2

fig. 33. That example of a correlation between two $\mathcal{F}(9,9)$ flips is present in crystals $\mathcal{Q}(|\chi_8| > 0)$ but it is not included in eq. (81). We will later refer to this cluster as $\mathcal{F}(9,9)^2$. The question for the true ground state energy of a GPS-class seems very difficult to answer exactly, especially when considering aperiodic crystals. Perhaps some atom clusters with three of four correlated flips will also include low energy flip states, similar to the $\mathcal{F}(9,9)^2$-example of fig. 33. The effect of such larger clusters on E_0 could be taken into account in the same way as for the one-flip-clusters $\mathcal{F}(8,7)$ and $\mathcal{F}(9,8)$. It is not clear till which cluster size such an energy lowering effect can occur. At least for the PC-clusters we compared all flip states of each cluster to see which is their ground state. It was found that all clusters have minimal energy in their initial state (the one in the flat crystal), except for those that include the flips $\mathcal{F}(8,7)$ or $\mathcal{F}(9,8)$. So nearest neighbour correlations provide no correction to the ground state energy. Hence, eq. (81) is also the ground state energy in the model of pentagonally coupled flips.

5 Results

5.1 Including the Flip Restriction

5.1.1 Ground State Energy

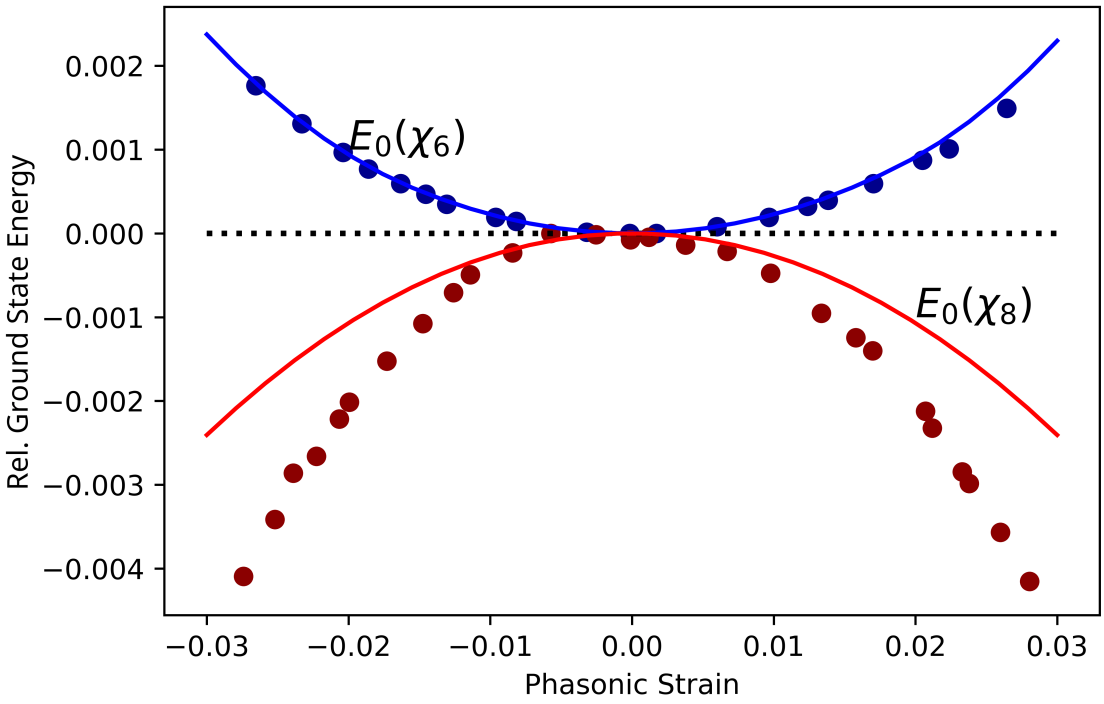

Figure 48: The offset adjusted ground state energy $E_0(\chi_6) - E_0(0)$ and $E_0(\chi_8) - E_0(0)$. The single dots are data from Kiselev's thesis. We refer to the dotted graphs as $E_0^{(\mathrm{K})}(\chi)$. Continuous curves are calculated from eq. (81).

A plot of E_0 over χ_6 and χ_8 is seen in fig. 48. The curves are compared with the ground state energies of Kiselev who obtained them via Monte Carlo driven phasonical relaxation. We may refer to his energy values as $E_0^{(\mathrm{K})}(\chi)$. Both data sets, $E_0(\chi)$ and $E_0^{(\mathrm{K})}(\chi)$ were manipulated by adding a constant offset such that the curves meet in the origin. This way, it is easier to compare the different curvatures. The true value for $E_0^{(\mathrm{K})}(0)$ in Kiselev's work was -6.649, while the analytic expression eq. (81) yields $E_0(0) = -6.647$ as the QCs ground state energy. The small difference between these values must be due to the fact that in Kiselev's computation the QC was modeled by an approximant with very small phasonic strain.

It is remarkable how well the two data sets $E_0^{(\mathrm{K})}(\chi_6)$ and $E_0(\chi_6)$ are agreeing. We conclude that the vertex densities in Kiselev's approximants are very close to the densities predicted by the polar calculus. The nice accordance of the parabolas also suggests that Kiselevs phasonic relaxation in χ_6-approximants consisted mostly of individual flips $\mathcal{F}(8,7)$ (the other energy lowering flip, $\mathcal{F}(9,8)$, has almost zero density in $\mathcal{Q}(\chi_6)$, comp. table 4). It makes sense that the phasonic relaxation did not include many correlated flips because these are likely to violate the flip restriction rule that was used throughout his work. The red parabolas, $E_0^{(\mathrm{K})}(\chi_8)$ and $E_0(\chi_8)$ do not agree so well. Here Kiselevs approximants reach significantly lower energies than the continuous curve. Therefore also the curvatures of the two parabolas will differ, which has an impact on the pha-

sonic constant λ_8. The most significant reason seems to be that, other than for χ_6, the crystals $\mathcal{Q}(\chi_8)$ may include clusters of correlated flips that can lower the energy and also obey the flip restriction rule. But the most important feature of fig. 48 is that the parabolas $E_0^{(\mathrm{K})}(\chi_8)$ and $E_0(\chi_8)$ are open downwards. So both models predict the QC to be unstable at $T = 0$, as was observed in Engel's simulation. Rather, fig. 48 suggests that the true ground state should lie in some χ_8-GPS-class. Actually, the true ground states, the Xi-approximants, have phasonic strain in both χ-directions ($\chi_8 = -0.180$, $\chi_6 = 0.111$ and $\chi_8 = 0.146$, $\chi_6 = 0.034$), but they lie beyond the range presented here. The curvatures $\partial^2_{\chi_6} E_0(\chi_6)$, $\partial^2_{\chi_8} E_0(\chi_8)$ are exactly the values of the phasonic constants at $T = 0$. These curvatures are listed below. We also write the curvatures of $E_0^{(\mathrm{K})}(\chi)$ obtained by Kiselev, denoted $\lambda^{(\mathrm{K})}(0)$, which were extracted from his diploma thesis [10].

$$\lambda_6(0) = 2.265, \qquad \lambda_8(0) = -2.676 \tag{82}$$

$$\lambda_6^{(\mathrm{K})}(0) = 2.314, \qquad \lambda_8^{(\mathrm{K})}(0) = -5.318 \tag{83}$$

An error due to imperfections in the parabolic fit occurs in the parameters $\lambda(0)$ not earlier than in the fourth decimal place.

A phasonic relaxation was also already done by Michael Engel. Even though the general structure of his 3D plot of the phasonic ground state energy (fig. 30b) seems to agree with the graphs of fig. 48, his numeric results for the phason elastic constants, which shall be called $\lambda^{(\mathrm{E})}(0)$, show deviations from the values of $\lambda^{(\mathrm{K})}(0)$ and $\lambda(0)$.

$$\lambda_6^{(\mathrm{E})}(0) = 1.1, \qquad \lambda_8^{(\mathrm{E})}(0) = -2.1.$$

Engel mentioned that these constants have large error ranges, probably due to imperfection in the stochastic relaxation process. Unfortunately, concrete values for the error bars were not provided.

5.1.2 Discussion of the Contribution of Flip Correlations to $E_0(\chi)$

One might wonder if the previously mentioned cluster of $\mathcal{F}(9,9)$-flips (fig. 33 on page 49, let us call it $\mathcal{F}(9,9)^2$) could be what makes the difference between the curves $E_0^{(\mathrm{K})}(\chi_8)$ and $E_0(\chi_8)$. Each such cluster lowers the total energy by an amount $E^{(V_8)} - E^{(V_9)}$. So we may include it in eq. (81) by adding the term $n_{\mathcal{F}(9,9)^2}(E^{(V_8)} - E^{(V_9)})$, where $n_{\mathcal{F}(9,9)^2}$ is the density of these clusters, as always obtained from the polar calculus. The result is seen in fig. 49a. Indeed, now the analytical and numerical curves agree much better over the χ_8-variable. The curvature resulting from this plot is $\lambda_8'(0) = -4.544$, so still not quite the same as $\lambda_8^{(K)}(0)$. Probably, Kiselev's phasonic relaxation included more kinds correlated flips besides $\mathcal{F}(9,9)^2$.

One might also speculate whether the shape of the numerical parabola is significantly effected by the fact that $E_0^{(\mathrm{K})}(\chi)$ is a function over approximants, i.e. over the set $\{\chi^p\}$. As such, it has infinitely many discontinuities and must deviate from the analytical function $E_0(\chi)$ everywhere (comp. section and appendix 8.2). These discontinuities could explain the small fluctuations that are visible especially in $E_0^{(\mathrm{K})}(\chi_8)$. But such fluctuations alone should not be able to change the parabolas shape enough to produce a deviation in curvature of size $|\lambda_8^{(\mathrm{K})}(0) - \lambda_8'(0)| = 0.774$. For the same argument would also hold in the case of $E_0^{(\mathrm{K})}(\chi_6)$, where the deviation of fit parameters is only 0.049.

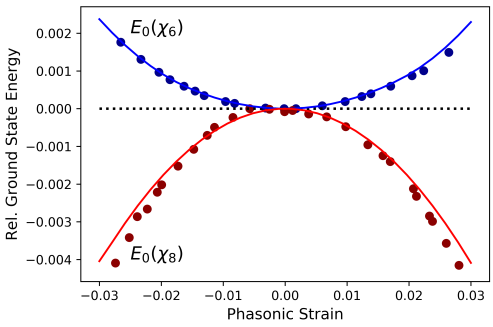

(a) Here the analytic energy $E_0(\chi)$ includes a correction term due to $\mathcal{F}(9,9)^2$-clusters. Thereby the red parabola $E_0(\chi_8) - E_0(0)$ becomes more narrow and comes closer to the numeric data points. $E_0(\chi_6)$ is not effected by this adjustment.

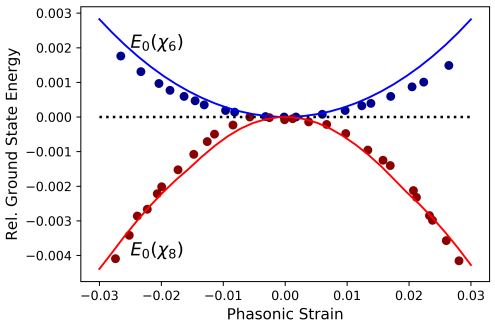

(b) Additionally to $\mathcal{F}(9,9)^2$, also $\mathcal{F}(8,8)^2$-correction terms are added to $E_0(\chi)$. The $\mathcal{F}(8,8)^2$-cluster is shown in fig. 50b. The new correction term decreases $E_0(\chi)$ further. But $E_0(0)$ is decreased more than $E_0(|\chi_6| > 0)$. Hence the parabola $E_0(\chi_6) - E_0(0)$ becomes narrower.

Figure 49: Ground energy with adapted offset such that all curves intersect the origin. The dotted graphs are the same as in fig. 48. The continuous curves result from eq. ((81)) with different correction terms.

Regardless of how crucial the cluster $\mathcal{F}(9,9)^2$ is for Kiselev's result $E_0^{(\mathrm{K})}(\chi_8)$, there is strong evidence that his phasonic relaxation did not reach the true ground state energy. This evidence is given by a second energy lowering flip cluster, which we shall call $\mathcal{F}(8,8)^2$ and, which was definitely ignored in the process. As shown in fig. 50b, after two correlated flips the energy of such a cluster is lowered by an amount $E^{(V_7)} - E^{(V_8)}$ compared to its initial state (the state in the flat crystal). Fig. 50a shows the course of the density of this cluster over χ. Clearly, it does not vanish at $\chi = 0$, hence $\mathcal{F}(8,8)^2$ is present in the QC. But in Kiselev's thesis it was written explicitly that the number of flips in the phasonic relaxation of the ideal quasicrystalline tiling was equal to zero. A plot of $E_0(\chi)$ that includes also $\mathcal{F}(8,8)^2$, analogously to $\mathcal{F}(9,9)^2$, is shown in fig. 49b. Note again that the curves are offset adjusted. The QC's analytical ground energy $E_0(0)$ drops by -0.001 when the $\mathcal{F}(8,8)^2$-effect is included in eq. (81). The blue parabola $E_0(\chi_6)$ now also deviates noticeably from its numerical counterpart because $\mathcal{F}(8,8)^2$ is also present in $\mathcal{Q}(\chi_6)$.

The $\mathcal{F}(8,8)^2$-cluster is only a representative example. Due to the flip restriction rule, it is likely that Kiselev's relaxation ignored more energy lowering flip correlations. The conclusion is that neither $E_0(\chi)$ nor $E_0^{(\mathrm{K})}(\chi)$ are really trustworthy candidates for the true χ-dependent ground state energy density. But the values $\lambda(0)$ are crucial for the phason elastic stability analysis of the QC. When we compute the full phasonic constants $\lambda(T)$, their offset will decide where, or even if a phase transition happens. So is there any meaningful choice for $\lambda(0)$? Yes, we should consider the values $\lambda_6(0) = 2.265$, $\lambda_8(0) = -2.676$, which come from the model of fully independent flips, without any correlation corrections. The reason is that they are consistent with the rest of our theory. As mentioned before, the PC-clusters add no correction to the ground state energy. Hence, any further correlations that may make an impact on $E_0(\chi)$ are not included in the model for the dynamic part of the free energy $F_c(\chi)$. Sure, there certainly are

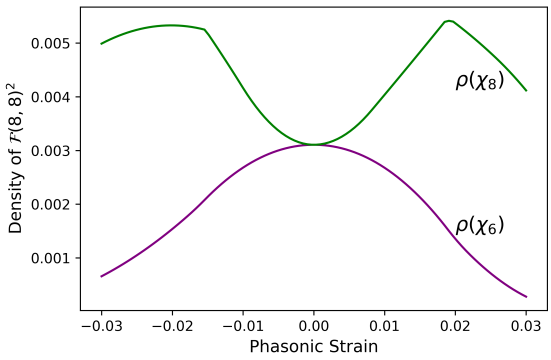

(a) Density of the $\mathcal{F}(8,8)^2$-cluster (configuration (1) in fig. 50b). The cluster has non zero density in the flat QC ($\chi = 0$). The curve $\rho(\chi_8)$ is far from harmonic for $|\chi_8| > 0.01$.

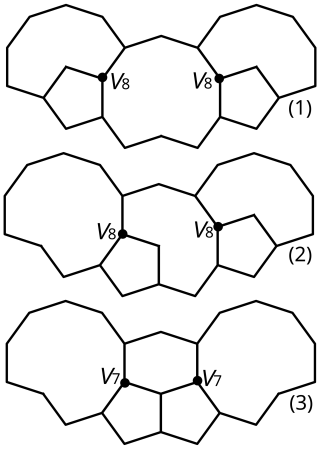

(b) Both flip atoms individually can only perform a flip $\mathcal{F}(8,8)$ in configuration (1). But if both atoms flip they lie in each others interaction circle. This changes their vertex type to V_7 and lowers their energy.

Figure 50

clusters of correlated flips that will have an effect on E_0 and $\lambda(0)$, perhaps even a big one. But likewise there are also various clusters that will make an impact on the flip dynamics and thereby on F_c and $\lambda(T)$. Loosely speaking, it is unfair to include clusters with large correlation distance, like $\mathcal{F}(9,9)^2$ in the ground state energy, but restrict the configurational free energy to nearest neighbour correlations. For now, the single flips and the PC-clusters are the only types of flip configurations for which all representatives with their densities are known. Hence, they will be the only ones to be regarded in a self-consistent model of the full free energy $F = E_0 + F_c$.

5.1.3 Configurational Free Energy

Before discussing and comparing the results of the configurational free energy density one thing should be mentioned. The flip energies ΔE_k defined in section 3.3.2 and listed in table 4 are simply differences of two vertex energies $E^{(V_j)}$ (table 2). Besides the vertex energies Kiselev also noted the flip energies explicitly in his thesis. The symmetric flips just have $\Delta E = 0$, as expected. The others are

$$\Delta E_{\mathcal{F}(7,8)} = 0.2663, \quad \Delta E_{\mathcal{F}(8,9)} = 1.99732, \quad \Delta E_{\mathcal{F}(7,9)} = 2.15422.$$

It is easy to check that these values differ from the naively calculated energy differences listed in table 4. Upon investigating this oddity, it turned out that Kiselev had used the larger cutoff radius $r_c = 2.5$ to compute the flip energies, rather than the one that defines the vertex environments and their energies ($r_c = 2$). This method, which was not further explained in his diploma thesis, seems to hold some inconsistencies. Firstly, for a larger cutoff radius there may also a larger number of environments around a flip atom, which have possibly different energies. Then two flips $\mathcal{F}(i,j)$ of the same type regarding the vertices V_i $i \in \{1,..,9\}$ could have different environments regarding the cutoff $r_c = 2.5$. So in these larger environments, the two flip particles could have different potential energies and thereby different flip energies. This means that using the cutoff radius 2.5 not

only the value of the flip energies should change, but also the number of flip types could increase. In that sense, attributing the flips that are defined via $r_c = 2$ only a single energy value with respect to $r_c = 2.5$, that value might not be well defined. However, while trying to construct a demonstrative example for this problem we came to the conclusion that for none of the flips used by Kiselev such an energy splitting occurs. For all of his flips (the 'allowed' ones), the possible atom environments within a interaction circle of $r_c = 2.5$ provide actually the same flip energy. Only the value of that energy changes compared to $r_c = 2$. Still, an example of the described energy ambiguity is shown in appendix 8.4, but that example-flip is forbidden in the selection rule.

Secondly, it seems odd to use a different cutoff radius for the vertex energies E^{V_i} that are used in the ground state energy, eq. (81) than for the flip energies ΔE_k that are used in the configurational free energy. But actually, Kiselev did not use the vertex energies of table 2 to compute $E_0^{(\mathrm{K})}$. Rather, he measured the potential energy density during the phasonic relaxation so long till it converged to a minimal value. Since he measured the flip energies that are part of this process with the cutoff $r_c = 2.5$, we assume that he also used the same cutoff to measure the total potential energy of the sample. Of course, the analytical results for $E_0(\chi)$ shown in the previous chapter do depend directly on the vertex energies of cutoff radius 2. So this could be another error source when comparing later results of $\lambda(T)$ to Kiselev's. But at least for $E_0(\chi_6)$, we see that the analytical and numerical ground state energies agree well, despite the supposedly different vertex energies. Either way, in this section we have the chance to use the same flip energies as Kiselev, noted above, to calculate the configurational free energies.

Fig. 51a shows a plot of the relative configurational free energy density $F_c(\chi) - F_c(0)$ over the phasonic strain χ_6 and χ_8 at a temperature $T = 0.35$. The continuous curves were calculated using the model of independent flips (eq. (63) in section 3.3.2). Only the flip types $\mathcal{F}(7,7)_a$, $\mathcal{F}(8,8)$, $\mathcal{F}(9,9)$, $\mathcal{F}(7,8)$, $\mathcal{F}(8,7)$ were taken into account. These are the ones that are allowed according to Kiselev's flip restriction rules. The dotted data points in fig. 51a show the relative configurational free energy $F_c^{(\mathrm{K})} - F_c^{(\mathrm{K})}(0)$ from Kiselev's diploma thesis, also at $T = 0.35$. Both data sets are offset adjusted such that all curves intersect the origin. The true values at $\chi = 0$ are $F_c(T = 0.35, \chi = 0) = 0.0291$ and $F_c^{(\mathrm{K})}(T = 0.35, \chi = 0) = -0.0294$.

The blue graphs in fig. 51a, $F_c(\chi_6)$ and $F_c^{(\mathrm{K})}(\chi_6)$, agree very well for $|\chi_6| < 0.01$, but diverge at larger phason strain. This is due to the phasonic relaxation. Although we assume that no correlated flips were part of Kiselev's phasonic relaxation of the χ_6-crystals, the single flips $\mathcal{F}(8,7)$ that were part of it should i.g. still be coupled to other, neighbouring flips. The type of these neighbouring flips would change upon flipping $\mathcal{F}(8,7)$ and so would the flip numbers N_k counted in the ground state. These altered flip numbers (or rather the corresponding densities) will of course impact $F_c^{(\mathrm{K})}(\chi)$. Recall that the flip densities n_k in the analytic model are computed from the flat LI-class. The density of energy lowering flips $\mathcal{F}(8,7)$ is zero at $\chi_6 = \chi_8 = 0$ and grows monotonically with $|\chi_6|$. Therefore also the effect of altering flip densities in phasonically relaxed crystals, and thereby the discrepancy between the the blue curves, will be neglectable around $\chi = 0$ and increase for larger phasonic strain.

Exactly the same effect also happens in the χ_8-approximants. But here it is even stronger, since the phasonic relaxation of crystals $\mathcal{Q}(|\chi_8| > 0)$ includes, additionally to $\mathcal{F}(8,7)$, also $\mathcal{F}(9,8)$ and several correlated flip sequences, one of them $\mathcal{F}(9,9)^2$. The latter shall now demonstrate the error that is being discussed. During the relaxation two initial

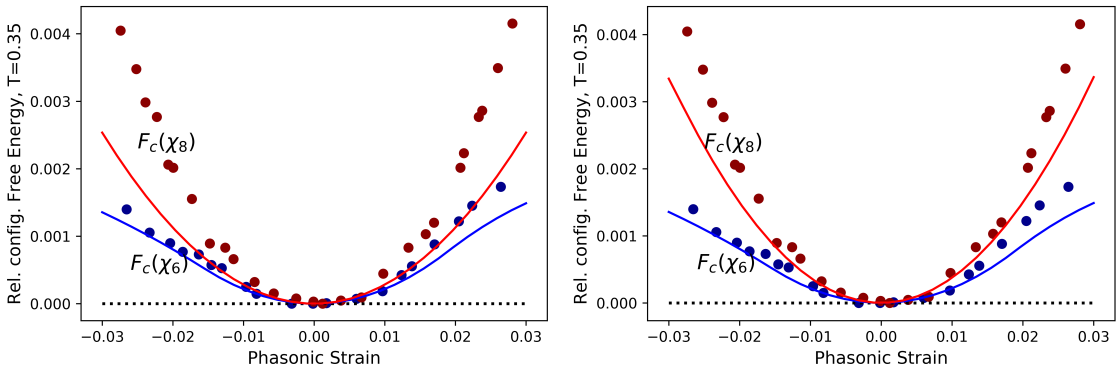

(a) Both analytical curves are calculated using the flip densities that are found in a flat crystal $\mathcal{Q}(\chi)$. The flip densities in the numeric computation were measured in the ground state of each GPS-class.

(b) Here a correction term is added to $F_c(\chi_8)$. It represents certain changes of flip densities in the phasonic relaxation due to flip correlations in the cluster $\mathcal{F}(9,9)^2$.

Figure 51: Configurational free energy density over phason strain at temperature $T = 0.35$. The scattered data points show Kiselev's results $F_c^{(\mathrm{K})}(\chi)$, to which the analytical, continuous curves $F_c(\chi)$ are compared.

$\mathcal{F}(9,9)$-flips, which contribute strongly to the free energy since $\Delta E_{\mathcal{F}(9,9)} = 0$, become $\mathcal{F}(8,9)$-flips. The latter have almost vanishing contribution at low temperatures because $\Delta E_{\mathcal{F}(8,9)} > T_m$. Hence, counting the numbers of single flips in a crystal where all $\mathcal{F}(9,9)^2$-configurations are in their ground state will lead to a lower entropy and larger free energy than if the numbers were counted in the flat LI-class. Together with the fact that $n_{\mathcal{F}(9,9)^2}(\chi_8)$ is monotonically increasing over $|\chi_8|$, this explains why Kiselev's parabola $F_c^{(\mathrm{K})}(\chi_8)$ is narrower than $F_c(\chi_8)$.

In principle, such effects on $F_c^{(\mathrm{K})}$ due to altered flip densities can be imitated in F_c similarly as the changes of E_0 due to energy lowering flips. Meaning we subtract the flip contribution of all $\mathcal{F}(9,9)$-flips that are part of a $\mathcal{F}(9,9)^2$-cluster and replace them by the flip term corresponding to $\mathcal{F}(8,9)$-flips. Formally, this adjusted version of F_c reads

$$\begin{aligned} F_c(T,\chi) = -T\Big[\sum_k n_k \ln\Big(1+\mathrm{e}^{-\Delta E_k/T}\Big) \\ + 2n_{\mathcal{F}(9,9)^2}\Big(\ln\Big(1+\mathrm{e}^{-\Delta E_{\mathcal{F}(8,9)}/T}\Big) - \ln(2)\Big)\Big]. \end{aligned} \tag{84}$$

A plot of the free energy calculated from this equation is seen in fig. 51b. The red parabola $F_c(\chi_8)$ has become narrower and fits better to $F_c^{(\mathrm{K})}(\chi_8)$. But there is still some difference between the two data sets. To make them agree even better, one would have to identify all the flips that were part of the phasonic relaxation and also classify them according to their coupling to neighbouring flips (this was not done completely in the $\mathcal{F}(9,9)^2$-example). With all this information at hand, more correction terms could be added to eq. (84), which should improve the accordance between the analytical and numerical model further.

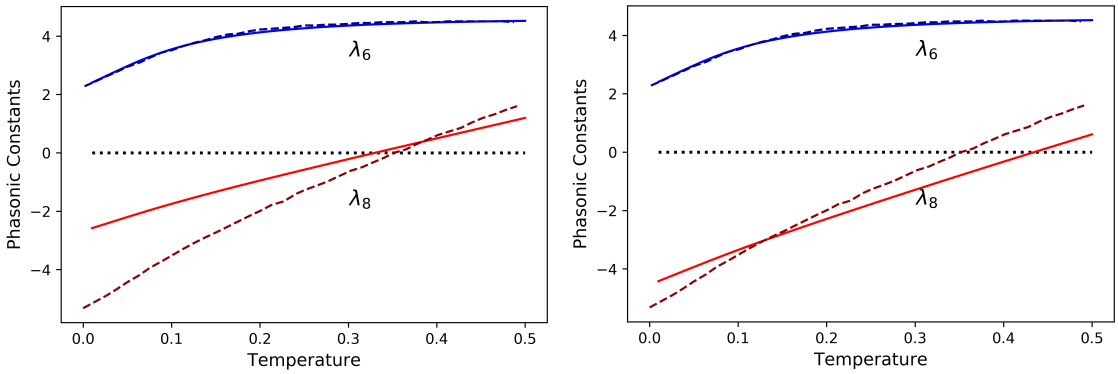

(a) The continuous curves, $\lambda(T)$ were calculated using the approximation of independent single flips for E_0 and F_c.

(b) Here the impact of flip correlations in the cluster $\mathcal{F}(9,9)^2$ was taken into account in the analytical phasonic relaxation, hence in E_0, and also in the flip densities that were calculated from the corresponding ground state.

Figure 52: Phason elastic constants over temperature. The QC's melting temperature in the simulation was at $T = 0.56$. Dotted lines are Kiselev's numeric results, $\lambda^{(\mathrm{K})}(T)$ published in [64].

5.1.4 Phason Elastic Constants

The phason elastic constants $\lambda(T)$ are calculated with an offset $\lambda(0) = \partial_\chi^2 E_0(\chi)$ that ignores all flip correlations during the phasonic relaxation and a temperature dependent part $\partial_\chi^2 F_c(T,\chi)$ that considers only flips which are in accordance with Kiselev's flip selection rule. Also, the temperature dependent part was calculated using Kiselev's flip energies mentioned in the previous section to better compare the analytic results, $\lambda(T)$, to his. These results are seen in fig. 52a, where the dotted lines are the numeric phasonic constants $\lambda^{(\mathrm{K})}(T)$, which were taken from the review paper [64].

$\lambda_6(T)$ and $\lambda_6^{(\mathrm{K})}(T)$ agree very good for the full temperature range. Considering the discrepancy in the configurational free energies $F_c(\chi_6)$, $F_c^{(\mathrm{K})}(\chi_6)$, this is actually surprising. But recall that, to determine $\lambda(T)$, we apply a quadratic fit to $F_c(T,\chi)$ that only uses the small interval $|\chi| < 0.01$. In this region, the analytical and numerical free energies of χ_6-crystals coincide almost perfectly. Presumably, Kiselev used the whole interval $|\chi| < 0.03$ for a fit to determine $\lambda^{(\mathrm{K})}(T)$. But, while $F_c(\chi_6)$ clearly shows non-harmonic behaviour at $|\chi_6| > 0.02$, $F_c^{(\mathrm{K})}(\chi_6)$ stays more in parabolic shape. So this larger fit interval should not distort his fit parameter as much as it would for a fit to $F_c(\chi_6)$.

The curves of $\lambda_8(T)$, $\lambda_8^{(\mathrm{K})}(T)$ have different values at $T = 0$ and different slopes. The causes of both features are explained by the discussion of $E_0(\chi_8)$ and $F_c(\chi_8)$ in the previous chapters. It is clear from fig. 51 that a fit to $F_c^{(\mathrm{K})}(\chi_8)$ in the interval $|\chi_8| < 0.03$ will predict a larger curvature than a fit to $F_c(\chi_8)$ in any interval. The general behaviour of $\lambda_8(T)$ and $\lambda_8^{(\mathrm{K})}(T)$ is similar though. Starting from negative values they increase monotonically with T and change their sign before reaching the melting temperature $T_m = 0.56$. As explained in chapter 3.1.2, the sign of the phasonic constants decides over the QCs stability. λ_6 is always positive, which supports the QC. The sign change of

λ_8 predicts a phase transition with the QC being the high temperature phase. Remarkably, very similar phase transition temperatures (0.33 and 0.35) are predicted by both models. The true phase transition in Engel's MD-simulation occurred at $T_c = 0.37 \pm 0.03$.

Regardless of how well $\lambda_8(T)$ or $\lambda_8^{(\mathrm{K})}(T)$ predict this empirical value, neither of them should be taken too seriously. They are based on the unjustified assumption that certain flips in the QC and other crystals $\mathcal{Q}(\boldsymbol{\chi})$ should be ignored regardless of their thermal probabilities (see section 3.3.2). The significant effects of this selection rule will be demonstrated in the next chapter. The rather nice results of fig. 52 are caused by two independent, false assumptions. Namely the flip restriction and the sufficiency of the independent flip approximation.

In the previous chapters, an idea was provided of how to fix the deviation of the numerical and analytical free energy in crystals $\mathcal{Q}(\chi_8)$. To some extend the analytical results could be brought to better agreement with the numerical ones by using an extension for the formulas of $E_0(\chi_8)$ and $F_c(\chi_8)$. The phasonic constants with the correlation-corrected offset $\lambda_8'(0)$ and a temperature dependent part according to eq. (84) are shown in fig. 52b. Both, the effect of flip correlations in the phasonic relaxation as well as the effect of the phasonic relaxation on the flip densities were reconstructed analytically only partially. Still, the corresponding improvements are already visible in the offset and slope of λ_8.

5.2 Phasonic Constants Without the Flip Restriction

Now we drop the flip selection rule. Nothing about the independent flip approximation or the general formulas for F_c and E_0 changes. But the flip type index k now runs over all 13 single flips of fig. 39. Also, other than in the previous calculations, here we use the simpler flip energies of table 4, instead of the values proposed by Kiselev. Otherwise, the energies of all vertices $V_4, .., V_{13}$ would have to be recalculated with larger cutoff radius $r_c = 2.5$. As shown in appendix 8.4, this would also increase the number of vertex and flip types. For the PC-clusters discussed in the next section, the variety of distinguishable types would grow even more if the large cutoff is used. In this sense, we are talking here about a slightly different crystal than the one in Engel's simulation. But as a plot of the potential (fig. 26) suggests, the difference of the LJG-potential between $r = 2$ and $r = 2.5$ is very small. That is why the following results are still worth comparing to those of the simulation.

The new phason elastic constants, $\lambda(T)$, are shown in fig. 53a. The values $\lambda(0)$ are not changed because none of the additional flips can decrease the potential energy. Strong deviation from Kiselev's results are visible. A phase transition into a stable QC phase is still present. But the transition temperature is less realistic as it lies at $T = 0.78$, so above melting temperature $T_m = 0.56$. $\lambda_8(T)$ is still monotonically increasing, but slower as in the previous case. $\lambda_6(T)$ is decreasing for $T > 0.3$ and its sign changes from positive to negative not far after $\lambda_8(T)$ switched from negative to positive. Hence, a hypothetical destabilization of the QC above $T \approx 1.2$ is predicted. Of course, in reality there would have been a transition into the liquid phase before. The model of rigid lattices and flips as the essential excitations has meaning only in a finite temperature range.

Actually, all the significant changes in this calculation compared to the one with the flip restriction come down to one new flip type. It is $\mathcal{F}(7,7)_b$. Due to zero flip energy (with $r_c = 2$), it has a strong contribution to the configurational free energy. As seen in table 4, the density of these flips increase over $|\chi_6|$ and $|\chi_8|$. So they help increase the

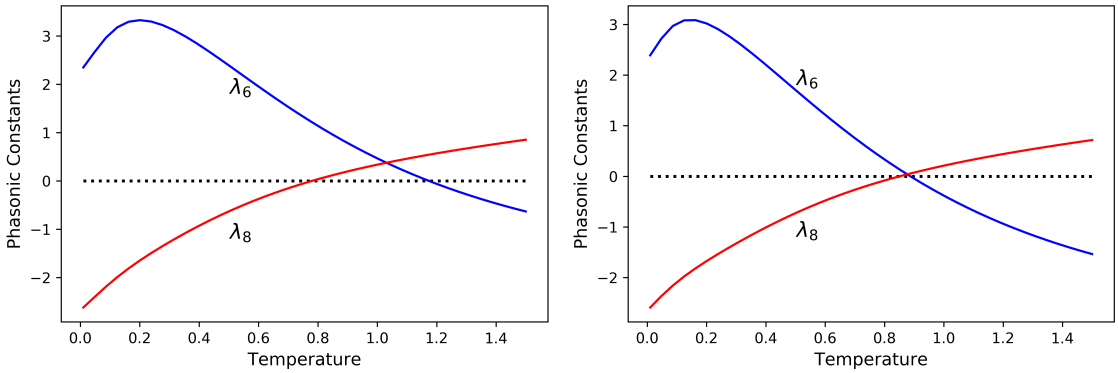

(a) The energies of all vertices and flips are calculated with cutoff radius $r_c = 2$.

(b) The energies of the important flips were calculated with the cutoff radius $r_c = 2.5$.

Figure 53: Phason elastic constants with the approximation of independent flips and including all possible single flips.

entropy in distorted crystals $\mathcal{Q}(\chi \neq 0)$ more than in the QC. That means they contribute to the phasonic constants negatively. All other flip types that were ignored by Kiselev have large flip energies and very small thermal probabilities at $T < T_m$. Fig. 54 shows the contribution $-\frac{\partial^2 n_k}{\partial \chi^2} \ln\left(1 + \mathrm{e}^{-\Delta E_k/T}\right)$ of all flip types to the phasonic constants. Flips which contribute positively ($0 > \partial_\chi^2 n_k$) and negatively ($0 < \partial_\chi^2 n_k$) to $\lambda(T)$ are distinguished by color. Also, the diagram is shown for two different temperatures $T = 0.2$ and $T = 0.6$, which are also distinguished by color. Only for the $\mathcal{F}(7,7)$-flips the two variants (a) and (b) are distinguished. For others, like $\mathcal{F}(7,11)_{a,b,c}$, the sum of contributions is shown. It is demonstrated that even at temperatures slightly above T_m the contribution of high energy flips is neglectable. Only for the $\mathcal{F}(7,8)$ and $\mathcal{F}(8,7)$-flips, which have the lowest nonzero energy, the temperature increase makes a noteworthy difference. To the symmetric flips, the temperature does not matter. The non visible flip contributions are not zero but just extremely small.

Because the only important flips are $\mathcal{F}(7,7)_a$, $\mathcal{F}(7,7)_b$, $\mathcal{F}(8,8)$, $\mathcal{F}(9,9)$, $\mathcal{F}(7,8)$ and $\mathcal{F}(8,7)$, we can actually approximate the phasonic constants of a system with cutoff $r_c = 2.5$ very well by only adjusting the energies of these flips. The others are neglectable for either cutoff radius. For $\mathcal{F}(7,7)_a$, $\mathcal{F}(8,8)$ and $\mathcal{F}(9,9)$, it is already known from Kiselev that they have $\Delta E_k = 0$ also in the longer potential range. Also, the energy of $\mathcal{F}(7,8)$ was already mentioned before, $\Delta E_{\mathcal{F}(7,8)} = 0.2663$. Only the energy of $\mathcal{F}(7,7)_b$ we must calculated explicitly for $r_c = 2.5$ (see appendix for details). It is $\Delta E_{\mathcal{F}(7,7)_b} = 0.015$. So changing only these flip energies the phasonic constants were calculated once again and are shown in fig. 53b. This plot should give an idea of how much the choice of potential cutoff impacts the phasonic constants. The general course of the two curves is not different compared to fig. 53a. But the sign change of λ_8 now happens at $T = 0.85$ and λ_6 cuts the horizontal axis already at 0.89. So the temperature interval where the QC would be stable (i.e. λ_6, $\lambda_8 > 0$) is vanishingly small and lies far above the melting temperature.

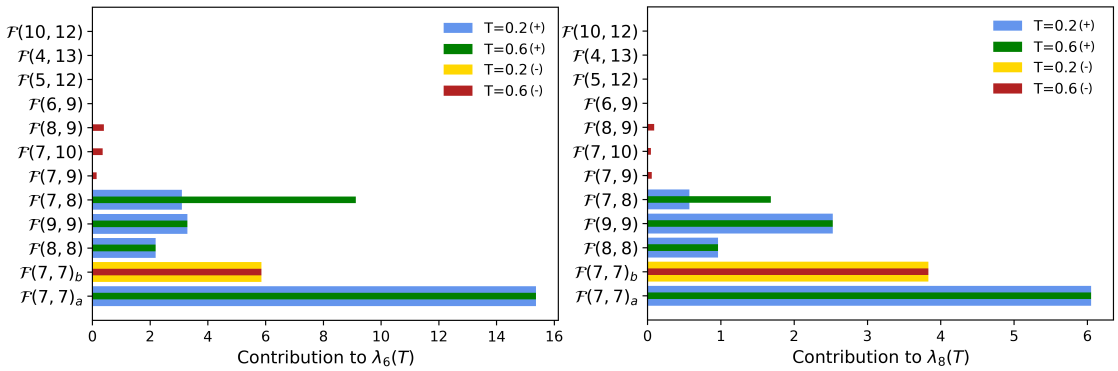

Figure 54: The contribution of different flip types to the phasonic constants is $-\frac{\partial^2 n_k}{\partial \chi^2} \ln\left(1 + \mathrm{e}^{-\Delta E_k/T}\right)$. It is shown for both phasonic strains at two temperatures. Some flips contribute positively (+), others negatively (-). Alone the flip $\mathcal{F}(7,7)_b$ makes the significant difference between the models with and without flip restriction.

5.3 Phasonic Constants Including Nearest Neighbour Correlations

The unsatisfying results of the previous section can be improved by switching from the approximation of independent single flips to the slightly more elaborate approximation of independent PC-clusters. In section 4.3.1, the structure of PC-clusters was explained. The phasonic constants are calculated once using the extended version of the canonical flip-Ising model (section 4.3.2) and once using the Markovian approach (section 4.3.4). In fig. 55 the solid lines represent the results of the canonical formalism, while the dashed lines show the results of the calculation using Markov chains.

As discussed in chapter 5.1.2, the offset values $\lambda(0)$ are still based only on uncorrelated single flips. The QC is now predicted to become stable at $T > 0.22$ and it stays stable beyond its empirical melting temperature. $\lambda_6(T)$ will change its sign above T_m. The phase transition temperature is not very accurate though. Recall the transition observed by Engel at $T_c = 0.37 \pm 0.02$. Over all, the pentagon correlations have the effect of increasing both, $\lambda_6(T)$ and $\lambda_8(T)$, which enlarges the temperature range of QC-stability. At low temperatures, the curves calculated with the Markov chain are almost identical to those of the canonical ensemble. At high temperatures, the difference between the two methods will become stronger.

In fig. 56, the quantity $-\frac{\partial^2 n_k^{\mathrm{pc}}}{\partial \chi^2} \ln\left(Z_k^{\mathrm{pc}}\right)$, which is a measure for the contribution of a PC-cluster to the phasonic constants is plotted, analogously as for the single flips before. Again, whether a flip contributes positively (+) or negatively (−) is marked by the color of the bars, like also the two representative temperatures ($T = 0.2$ and $T = 0.6$). Bars of zero width in the λ_6-plot correspond to clusters that are simply not present in $\mathcal{Q}(\chi_6)$. The distribution is much richer than for the single flips. Besides the dominant presence of $\mathcal{F}(7,7)_a\mathcal{F}(7,7)_a$, other, previously neglectable flips are now contributing significantly, e.g. $\mathcal{F}(6,9)_a\mathcal{F}(6,9)_a$ in the λ_8-plot.

The beneficial effect of the PC-model on the QC stability, compared to the model of single flips, is strong evidence that nearest neighbour correlations played a crucial role in the MD-simulation. The most important feature of the QC in terms of entropical stabilization is that it maximizes the density of symmetrical clusters with low energy

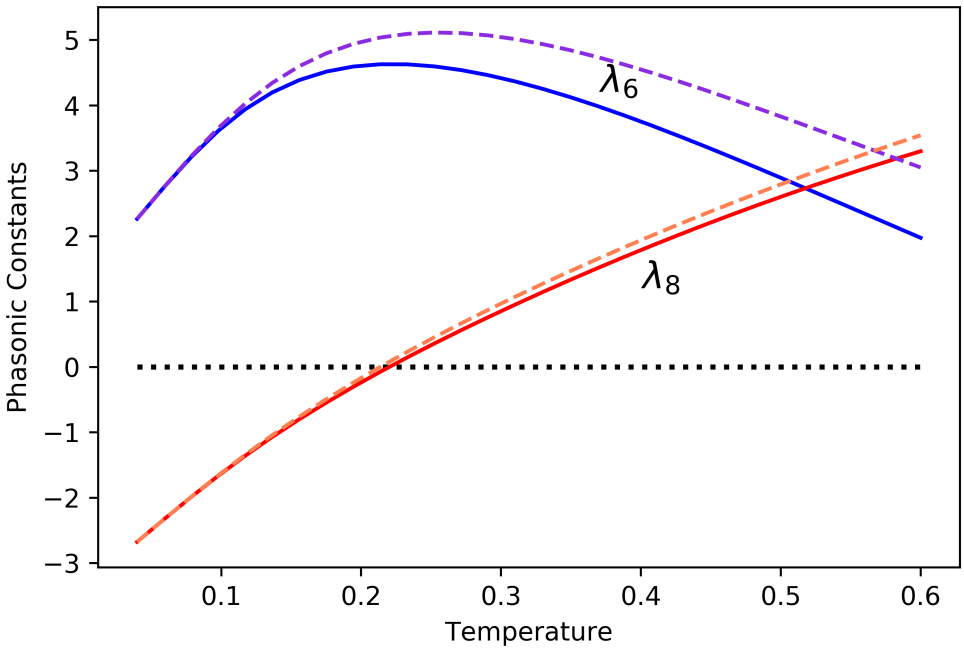

Figure 55: Phasonic constants from the model of PC-clusters. For solid lines the free energy of PC-clusters was calculated using the canonical Boltzmann formalism (section 4.3.2). For dashed lines, the Markov formalism of section 4.3.4 was used.

flips, most prominently the cluster $\mathcal{F}(7,7)_a\mathcal{F}(7,7)_a$.

5.4 On Low and High Temperature Stability

The plots of the phasonic constants, figs. 53 and 55, show only a small temperature interval. But the high temperature behaviour of $\lambda_6(T)$ and $\lambda_8(T)$ can be derived easily from their definition. For the model of independent single flips (SF) or PC-clusters this definition reads

$$\lambda(T) = \lambda(0) - T\sum_k \frac{\partial^2 n_k^{\mathrm{sf/pc}}}{\partial\chi^2}\ln\left(Z_k^{\mathrm{sf/pc}}\right), \tag{85}$$

where the index k labels either single flips or PC-clusters, and could in principal also refer to clusters of higher order correlation. For $T\to\infty$, all flip states will have the same thermal probability, regardless of their energy. Then Z_k^{sf} becomes simply $\ln(2)$ and Z_k^{pc} becomes $\ln(10)$. So the high temperature behaviour of the phasonic constants is simply

$$\lambda(T\to\infty) \propto -T\sum_k \frac{\partial^2 n_k^{\mathrm{sf/pc}}}{\partial\chi^2} = -T\partial_\chi^2 n_{\mathrm{tot}}^{\mathrm{sf/pc}}. \tag{86}$$

$n_{\mathrm{tot}}^{\mathrm{sf}}$, $n_{\mathrm{tot}}^{\mathrm{pc}}$ are the total densities of single flips or PC-clusters. They are i.g. not equal, and not only because the flip $\mathcal{F}(4,13)$ is missing in the PC-clusters. Every flip, except $\mathcal{F}(4,13)$, is contained in at least one PC-cluster. But every cluster contains two flips. Since not all flips are part of two PC-clusters simultaneously, we have $n_{\mathrm{tot}}^{\mathrm{pc}} < n_{\mathrm{tot}}^{\mathrm{sf}}$.

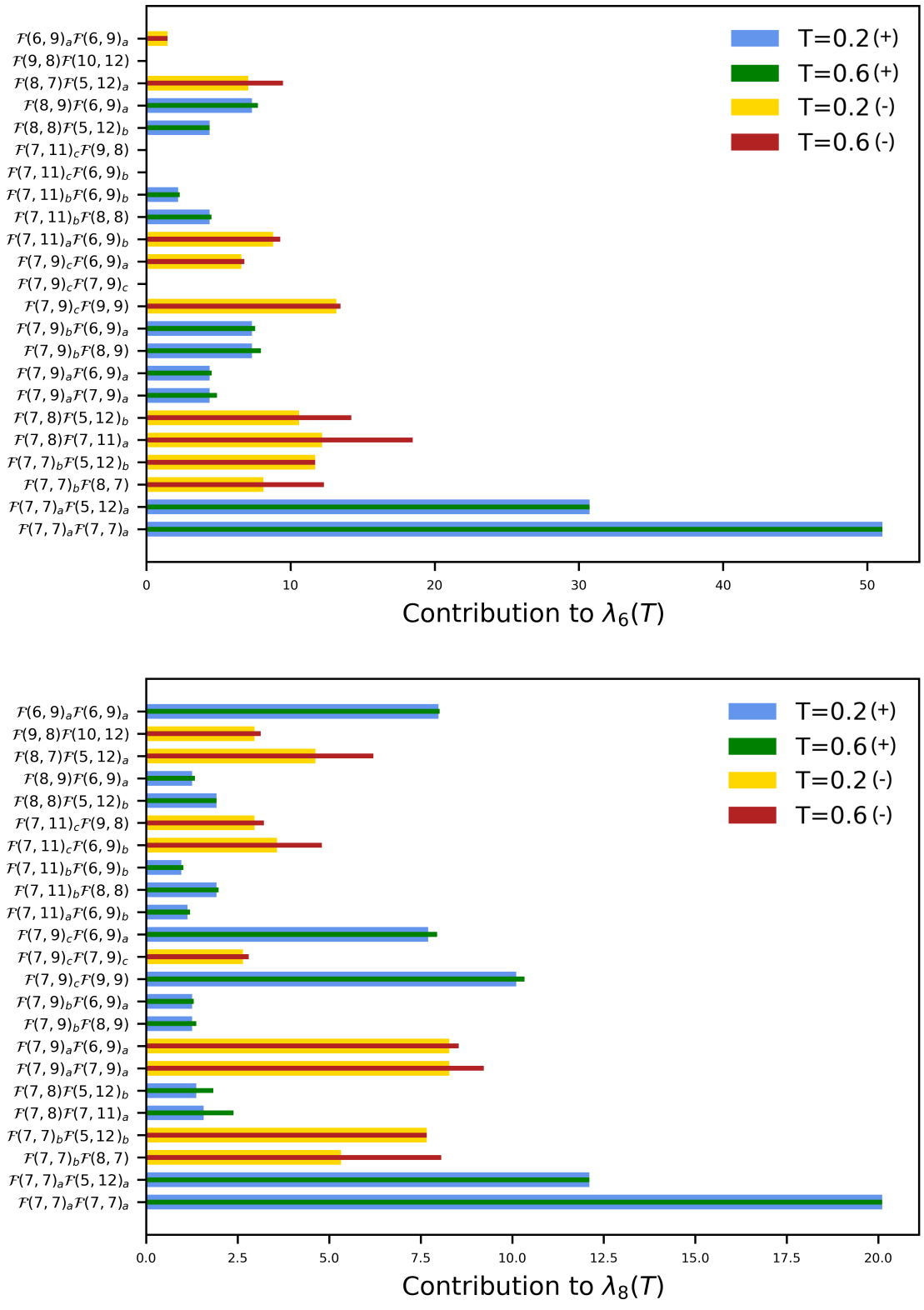

Figure 56: The contribution $-\frac{\partial^2 n_k^{\mathrm{pc}}}{\partial \chi^2}\ln\left(Z_k^{\mathrm{pc}}\right)$ of all PC-clusters to the phasonic constants. Depending on the curvature of n_k^{pc} a cluster $'k'$ contributes negatively (-) or positively (+). The contributions are shown for two different temperatures.

The curvature of the total single flip density could be calculated from the curvatures of single flips (table 4), which yields $\partial^2_{\chi_6} n^{\mathrm{sf}}_{\mathrm{tot}} = -0.0001$, $\partial^2_{\chi_8} n^{\mathrm{sf}}_{\mathrm{tot}} = -1.3143$. This would predict $\lambda^{\mathrm{sf}}_6, \lambda^{\mathrm{sf}}_8 > 0$ for $T \to \infty$. But these numbers are not accurate. The parabolic fit that was used to determine the curvatures was only accurate to the forth decimal place. As there are 13 flip types, an error up to ± 0.0013 for the total curvatures is possible. So we cannot be sure about the sign of $\partial^2_{\chi_6} n^{\mathrm{sf}}_{\mathrm{tot}}$, which is the crucial parameter concerning QC-stability.

The easiest and most safe way to determine this sign is simply to consider the acceptance domain of all flips together. It was called flip window in section 4.2.2. Instead of adding all flip ADs together, we can construct it simply as the AD of five atoms that built a generic flip rhombus. Then the density of all flips can be calculated by applying the polar calculus to the whole flip window. The relative density, $n_{\mathrm{tot}}(\chi)^{\mathrm{sf}} - n_{\mathrm{tot}}(0)^{\mathrm{sf}}$, is plotted over χ in fig. 57. Unsurprisingly, $\partial^2_{\chi_8} n^{\mathrm{tot}}(\chi_8)^{\mathrm{sf}}$ is clearly negative. At first glance $n^{\mathrm{sf}}_{\mathrm{tot}}(\chi_6)$ seems to be opened upwards and hence should have positive curvature. But it has clearly a non-parabolic shape, even in the small interval $|\chi_6| < 0.01$. That is rather unexpected because the curve is the sum of all single flip densities $n_k(\chi_6)^{\mathrm{sf}}$, which were almost perfect parabolas in this interval. Plotting $n_{\mathrm{tot}}(\chi_6)^{\mathrm{sf}}$ in even smaller intervals it still keeps its non-harmonic shape until eventually the numerical geometry program can no longer compute the χ-dependent AD-areas precisely. So the true curvature $\partial^2_{\chi_6} n^{\mathrm{sf}}_{\mathrm{tot}}$ may either be zero, meaning the lowest order polynomial in $n^{\mathrm{sf}}_{\mathrm{tot}}(\chi_6)$ is $\mathcal{O}(\chi_6^4)$, or it is extremely small but positive. Either way, fig. 57a clearly shows that there are crystals $\mathcal{Q}(\chi_6 > 0)$ with a larger flip density and therefore larger entropy than the QC. Hence the model of single flips cannot predict entropical QC-stability at $T \to \infty$. Thereby it is not in accordance with the RT-hypothesis, which was proven rigorously for the extreme case of fully degenerate tiling configurations [8]. It is not surprising that such a simple model is inaccurate at high temperatures. As T grows larger, more and more high energy flips are activated. Thereby, larger and more complicated sequences of correlated flips will have significant thermal probabilities and contribute to the free energy. This way, more and more LI-classes will be reachable from each other via flip sequences within a certain GPS-class. Eventually, not that GPS-class that has the largest flip density in one particular LI-class (like the flat one or the ground state) will have the highest entropy. Instead, that GPS-class dominates, which includes the largest variety of LI-classes.

Next, consider the curvature of the total PC-density, $\partial^2_\chi n^{\mathrm{pc}}_{\mathrm{tot}}$. This time, there is no uncertainty about the sign if we compute it like $\sum_{k=1}^{23} \partial^2_\chi n^{\mathrm{pc}}_k$ from the individual PC-curvatures from table 6. This summation, plus the density of $\mathcal{F}(4,13)$ yields $\partial^2_{\chi_6} n^{\mathrm{pc}}_{\mathrm{tot}} = -2.1116$, $\partial^2_{\chi_8} n^{\mathrm{pc}}_{\mathrm{tot}} = -2.5917$. Just to be sure, we computed the curvatures also directly from a fit to the curve $n^{\mathrm{pc}}_{\mathrm{tot}}(\chi)$, which was obtained from the AD of a generic PC-cluster, analogously as for the single flips. The fit parameters agreed with the noted values up to the forth decimal place. This is also another proof that the 23 PC-cluster types are complete. So it is $\lambda^{\mathrm{pc}}_6(T \to \infty) > 0$ and $\lambda^{\mathrm{pc}}_8(T \to \infty) > 0$. In fig. 55 the curve $\lambda^{\mathrm{pc}}_6(T)$ decreases, and it will indeed become negative at $T = 0.83$. This oscillating behaviour corresponds to the step wise 'activation' of flips of different energy. Once all flips are present with equal thermal probability, the curve will become and stay positive. Since we argued that flip correlations play an important role at high temperatures, it seems plausible that the PC-model agrees with the RT-hypothesis while the SF-model does not. But this coincidence should not be taken too seriously. Yes, the PC-clusters certainly include some high temperature flip sequences that are neglected in the SF-model. But the range of LI-classes reached this way is still far small to be compared to the excessive

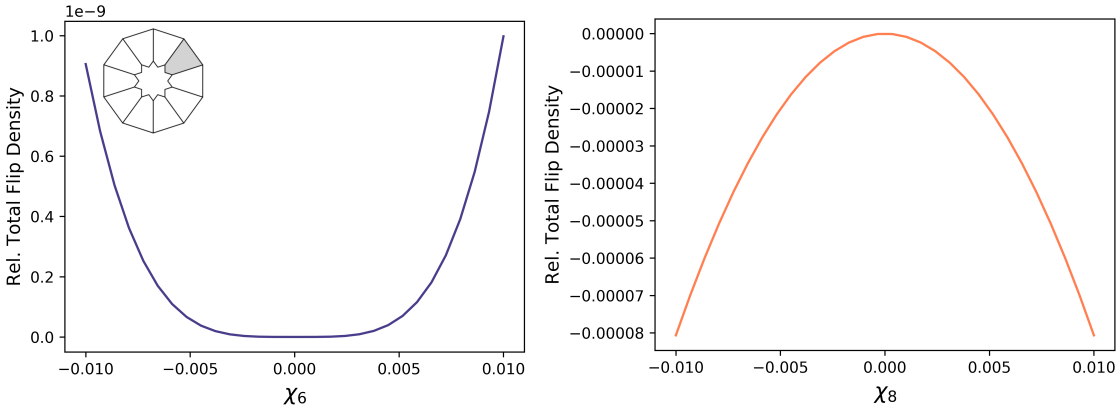

(a) (b)

Figure 57: The relative total density of single flips $n^{\mathrm{sf}}_{\mathrm{tot}}(\chi) - n^{\mathrm{sf}}_{\mathrm{tot}}(0)$. It is calculated from the polar calculus. The AD of all flips, called flip window, is seen in (a). The sign of the curvature of these curves decides over the QC-stability at $T \to \infty$ in the SF-model.

restructurings that would happen in a true high temperature RT-phase. For example, the effects of varying flip densities, mentioned in section 4.3.3 was completely ignored.

Of course, the QC-stability that is predicted at temperatures $0.22 < T$ is not stability in terms of a ground state. But it is also not stability in terms of a completely randomized tiling. The non-linear behaviour of $\lambda_6(T)$ shows that the crystal has not yet reached its fully degenerate RT-phase at $T = 0.6$. It is stabilized only by the fraction of PC-clusters that include many low energy flips. The LJG-potential supports predominantly flips in such symmetric clusters that are very frequent in the flat crystal $\mathcal{Q}(\chi = 0)$. So this low-temperature QC-stability happens not despite, but because of the interaction between the tiles.

The MD-crystal in Engel's simulation looked quite similar to the range of LI-classes that were considered in the present work. Meaning, it consisted mostly of $\mathcal{Q}$-tiles, P, H, N, U, D and also the S-tile that is created in the flip $\mathcal{F}(7,7)_b$ (see appendix 8.4). It is not a fully randomized tiling as was already explained in section 3.2. This supports the conclusion that the phase transition predicted by the model of PC-clusters is indeed the kind of phase transition that was observed in Engel's work. Still, the model certainly does not capture all the complex flip-effects that were part of the simulation, which is why the transition temperature is not very accurate. This accuracy should improve by extending the model to include higher order correlations. Such were certainly part of the MD-crystal as can be seen in Engel's dissertation [9].

6 Summary

In his diploma thesis from 2011, Kiselev computed the phason elastic constants of a QC that is based on the Tübingen triangle tiling and is governed by a pair interaction in form of the Lennard-Jones Gauß-potential. His thesis and also the present one are based on the MD-simulation of a QC by Engel. It serves as the empirical data.

The first goal of this thesis was to reconstruct these numerically computed phasonic constants, but with only analytical methods. The central formalism in this procedure is the polar calculus, which was explained in the beginning of this work. Then several aspects of Engel's and Kiselev's work were discussed. One thing that is definitely worth mentioning is that the general theory of phasonic constants is not well defined in the mathematical sense. The theory is based on the assumption that the phason elastic free energy $F(T, \boldsymbol{\chi})$ is an analytic function. It was explained that this is i.g. not true because $F(T, \boldsymbol{\chi})$ is not even continuous. However, there is a natural way to approximate $F(T, \boldsymbol{\chi})$ by a continuous function. This function, which is essentially the phasonic free energy itself but restricted to the domain of aperiodic crystals, was computed, but again only approximately. The approximation happens in the treatment of phasonic flips in the QC and related crystals. In the flip-Ising model, which was already used by Kiselev, the flips behave like a lattice of independent spin 1/2-particles. The main difference to Kiselev's work was that the densities of the different flip types were calculated analytically using the polar calculus. Comparing the ground energies $E_0(\chi)$, the configurational free energies $F_c(\chi)$ and the phasonic constants $\lambda(T)$, it was found that the analytical formalism can in principle reproduce the numerical results accurately. Concerning the phasonic strain variable χ_6, the analytical functions $E_0(\chi_6)$ and $\lambda_6(T)$ agreed very well with Kiselev's plots. Less accurate were the results concerning the other phasonic strain, χ_8. The differences were due to Kiselev's numerical phasonic relaxation, which was poorly imitated in the analytical independent flip model. A method to take the effects of the phasonic relaxation into account also in the analytical formalism was proposed and demonstrated. Indeed, the results improved when applying this correction method. Besides these quantitative differences, the main realizations of Kiselev's work were undoubtedly observed also in the analytical results. That is that the theory of phasonic constants predicts an instability of the QC at $T = 0$ and stability above some phase transition temperature $T_c > 0$. This was also the observation in Engel's simulation.

A second, important topic of this work was that part of Kiselev's work, and thereby also its analytical reconstruction, was subject to an unreasonable assumption that we called the flip restriction or flip selection rule. Discussing his work, we argued that any restriction of flips that is not due to low thermal probability is not justified. Using a larger, unrestricted set of flip types the phasonic constants were calculated again. The results deviated strongly from the calculation with restricted flips and did no longer match the observations of the MD-simulation. We concluded that the approximation of independent flips is actually not sufficient to explain the contribution of flip dynamics to the QC's thermal stability.

Thirdly, we proposed a slightly more elaborate model for the flip dynamics. Instead of single, independent flips, it considers independent pairs of flips. In each pair, the flips are coupled in a way that produces ten states which can be represented as the corners of a pentagon. Thus, this kind of interaction was called pentagonal coupling (PC) and the flip pairs together with further surrounding atoms were called PC-clusters. 23 types of PC-clusters were identified and classified. An extended version of the flip-Ising model was defined to calculate the free energy of each PC-cluster. Also, it was proposed that

the PC-clusters could be treated as Markov chains. The phasonic constants were calculated again with this new model, which is still fully analytic and based on the polar calculus. The result improved a lot compared to those of the independent flip approximation. It predicts the phase transition to the QC-phase at $T_c = 0.22 > 0$, which lies below the melting temperature of the crystal in the simulation. Still, it is inaccurate considering the empirical phase transition temperature $T_c = 0.37$. The stability at low but nonzero temperatures that our model predicts is not simply due to pure randomness in the QC-phase. Rather, the QC is found to support specific atom configurations that, in combination with the LJG-potential, produce a large configurational entropy already at low temperatures. So, the RT-hypothesis that states that QCs are entropy-stabilized high temperature phases was confirmed for a model QC with a non-trivial pair interaction potential using only analytical methods.

7 Outlook

Several topics were mentioned in this thesis but discussed only superficially. Some of them would deserve deeper investigation. First of all, the curious density functions $\rho(\boldsymbol{\chi})$, and thereby also the free energy $F(\boldsymbol{\chi})$ on the domain of all $\boldsymbol{\chi} \in \mathbb{R}^{2\times 2}$. It is remarkable how the continuous process of varying the orientation of a surface in a hyperspace can produce totally discontinuous functions. Related questions could be:

- Can the CPS of 2D and higher dimensional tilings be adjusted, like the 1D case, such that the polar calculus works also on periodic CPS-tilings exactly? Possible approaches could be to study the choice of the hyperlattice or the choice of the window.
- Can the discontinuities in the density functions be characterized somehow? Can the whole $\boldsymbol{\chi}$-space be divided into certain regions, each with an upper limit for the discontinuous fluctuations of ρ?

In section 2.5, one question was mentioned that is important for the conceptual range of the formalism that we used.

- Given a 2D CPS-tiling like the TTT or similar ones that supports the concept of phasonic flips, consider all infinite tilings that can be built using the prototiles of the given tiling. By projecting the $E^{\parallel}$-coordinates of these tilings into the hyperspace, each tiling can be attributed a 2D cut-surface, perhaps a very rough one. The average orientation of this surface corresponds to the global phasonic strain (GPS) of the tiling. Now, can all tilings that have the same GPS be transformed into each other only via sequences of phasonic flips?
- And if so, are the distances of correlated flips in such sequences bounded? Here we assume that using flip sequences with unbounded correlation distances also transitions between tilings of different GPS should be possible

These questions did not directly impact the calculations in this thesis. Of the tilings that were considered, all those with same GPS were by definition related to each other through flip sequences with finite correlation distance.

Concerning our flip model, it would of course be interesting to consider the structure of clusters with higher order correlation. Also, the model of PC-clusters holds similar problems as the single flip model that it should improve. While the latter neglects all flip correlations, the PC-clusters take into account the correlation of next neighbour pairs. But each pair is still considered independent, while in reality they are also coupled to each other. Hence, again we ignore certain correlations. Here, an important question arises. Does the error of the free energy due to neglecting flip correlations increase or decrease if F is computed using larger and larger clusters of coupled flips but neglecting the coupling between the clusters? Our results, which are much more realistic with the PC-model than with the single flip model, clearly suggest that error decreases. But a more quantitative explanation would be nice.

The question about QC-stability is often simply called 'energy vs. entropy'. The answer of this thesis is entropy, in the sense that the QC minimizes $F(T > T_c, \boldsymbol{\chi})$ but not $E_0(\boldsymbol{\chi})$. But it is also not stabilized by pure randomness. Its essential feature are finite atom clusters that allow many different states of similar energy. Are there experimental high temperature QCs with similar properties? What is their analog to the cluster

$\mathcal{F}(7,7)_a\mathcal{F}(7,7)_a$ that contributes so much to the stability in our case. Finding such key-structures and their flipping behaviour could give insight into the interaction potential of real QCs.

8 Appendix

8.1 Origin of the phasonic displacement

Consider the function $F(\boldsymbol{x}) = \mathrm{e}^{(\boldsymbol{k}_1\cdot\boldsymbol{x})}+\mathrm{e}^{(\boldsymbol{k}_2\cdot\boldsymbol{x})}$ with $\boldsymbol{x}$ variable in $\mathbb{R}^2$. Let $\boldsymbol{k}_1$ and $\boldsymbol{k}_2$ be two orthonormal wave vectors in $\mathbb{R}^2$. Then F is periodic on the lattice $\{n\boldsymbol{a}_1+m\boldsymbol{a}_2|n,m\in\mathbb{Z}\}$ with $\boldsymbol{a}_1\cdot\boldsymbol{k_1}=2\pi$, $\boldsymbol{a}_1\cdot\boldsymbol{k_2}=0$ and $\boldsymbol{a}_2\cdot\boldsymbol{k_1}=0$, $\boldsymbol{a}_2\cdot\boldsymbol{k_2}=2\pi$. Now decompose $\mathbb{R}^2$ into $E^{\parallel}$ and $E^{\perp}$, which are rotations of the $\boldsymbol{k}_2$ and $\boldsymbol{k}_2$-axis as in section 2.2.3. We define the cut-function

$$f(x^{\parallel}) = F(\boldsymbol{x})|_{x^{\perp}=0} = \mathrm{e}^{ik_1^{\parallel}x^{\parallel}} + \mathrm{e}^{ik_2^{\parallel}x^{\parallel}}$$

as the function F with its domain being reduced to $E^{\parallel}$. If $E^{\parallel}$ cuts through the $\{\boldsymbol{k}_1,\boldsymbol{k}_2\}$-coordinate system at an angle θ such that the slope $m^{\parallel}=\tan(\theta)$ and therefore the ratio of the projected wave vectors $k_1^{\parallel}/k_2^{\parallel}=m^{\parallel}$ are irrational, it is easy to show that $f(x^{\parallel})$ is aperiodic. We can create aperiodic functions from higher dimensional periodic functions very similar as aperiodic lattices are projections of higher dimensional periodic lattices. Now independent of the slope, shifting the coordinate system by some vector $\boldsymbol{\gamma} = (\gamma^{\parallel},\gamma^{\perp})\in\mathbb{R}^2$, we consider how its different components impact the cut function

$$\widetilde{f}(x^{\parallel}) = F(\boldsymbol{x}+\boldsymbol{\gamma})|_{x^{\perp}=0} = \mathrm{e}^{i(k_1^{\parallel}(x^{\parallel}+\gamma^{\parallel})+k_1^{\perp}\gamma^{\perp})} + \mathrm{e}^{i(k_2^{\parallel}(x^{\parallel}+\gamma^{\parallel})+k_2^{\perp}\gamma^{\perp})}. \tag{87}$$

While the shift $\gamma^{\parallel}$ in parallel space just causes a rigid translation of $f(x^{\parallel})$ the $\gamma^{\perp}$-shift in perpendicular space creates also a phase difference $\frac{k_1^{\perp}}{k_1^{\parallel}}-\frac{k_2^{\perp}}{k_2^{\parallel}}=\frac{2}{\sin(2\theta)}$ between the two plane waves. Using trigonometric identities, eq. 87 can also be written as a product of a plane wave with wave vector $\frac{1}{2}(k_1^{\parallel}+k_2^{\parallel})$ with an amplitude modulation with wave vector $\frac{1}{2}(k_1^{\parallel}-k_2^{\parallel})$

$$\begin{aligned}\widetilde{f}(x^{\parallel}) =& 2\cos\left(\frac{(k_1^{\parallel}-k_2^{\parallel})}{2}\left(x^{\parallel}+\gamma^{\parallel}+\frac{k_1^{\perp}-k_2\,{}^{\perp}}{k_1^{\parallel}-k_2^{\parallel}}\gamma^{\perp}\right)\right)\\ &\exp\left\{i\frac{(k_1^{\parallel}+k_2^{\parallel})}{2}\left(x^{\parallel}+\gamma^{\parallel}+\frac{k_1^{\perp}+k_2\,{}^{\perp}}{k_1^{\parallel}+k_2^{\parallel}}\gamma^{\perp}\right)\right\}.\end{aligned}$$

Then the phase difference between the plane wave and the modulation wave is

$$\frac{k_1^{\perp}+k_2\,{}^{\perp}}{k_1^{\parallel}+k_2^{\parallel}}\gamma^{\perp}-\frac{k_1^{\perp}-k_2\,{}^{\perp}}{k_1^{\parallel}-k_2^{\parallel}}\gamma^{\perp}=\frac{2}{\cos(2\theta)}\gamma^{\perp}.$$

As the phase shift is only due to the $E^{\perp}$-displacement, manipulations of a CPS system in $E^{\perp}$-direction are called *phasonic* modes.

However, the $E^{\perp}$-space is a purely mathematical concept and does not exist as a real physical space in which one could perform translations. Physically the phasonic displacement corresponds to an inhomogeneous phononic displacement of the wave $\gamma^{\parallel}(x^{\parallel})$. Similarly the phasonic flips in a quasicrystal can be seen as a special kind of lattice vibration. This connection was first noted in [69]. There the plane wave from above (periodic or aperiodic) corresponds to a charge density wave (CDW) in a bcc crystal. This article originally introduced the term *phason* as a certain superposition of phonons that causes a phase shift in the CDW.

8.2 2D Approximants

Consider an arbitrary but fixed lattice vectors $\boldsymbol{p} = \sum_{i=1}^{4} n_i \boldsymbol{a}_i$ in $\mathcal{L}$. Upon applying a phasonic strain $\boldsymbol{\chi} = \begin{bmatrix} \chi_{11} & 0 \\ 0 & \chi_{22} \end{bmatrix}$, an approximant shall be created whose lattice $\mathcal{L}^{\parallel}$ is supposed to be periodic with respect to the $E^{\parallel}$-projections of this vector, i.e. $p^{\parallel}$. Lets denote the phasonically distorted lattice $\mathcal{L}'$. This means that every two points in $\mathcal{L}'$ that are separated by $\boldsymbol{p}'$ must have the same $E^{\perp}$-projection. So it is

$$\boldsymbol{P}^{\perp}(\boldsymbol{p}') = 0. \tag{88}$$

Writing the two components of this equation, labeled x and y, we have

$$\begin{aligned} p_x^{\perp\prime} &= \sqrt{\frac{\tau}{2\sqrt{5}}}\Big((\chi_{11}/\tau^2 - \tau)(n_1 + n_4) + (1/\tau - \chi_{11})(n_2 + n_3)\Big) = 0 \\ p_y^{\perp\prime} &= \frac{1}{\sqrt{2}}\Big((1 + \chi_{22})(n_1 - n_4) + (\chi_{22}/\tau - \tau)(n_2 - n_3)\Big) = 0. \end{aligned} \tag{89}$$

Already it is clear that the two components have each two independent integer parameters. Let us write this in a slightly different form using identities for the golden mean like $1 - \frac{1}{\tau} = \frac{1}{\tau^2}$.

$$\begin{aligned} p_x^{\perp\prime} &= \sqrt{\frac{\tau}{2\sqrt{5}}}\Big(\frac{-1}{\tau}(n_1 + n_4 - n_2 - n_3) - (n_1 + n_4) \\ &\quad + \chi_{11}\Big[n_1 + n_4 - n_2 - n_3 + \frac{-1}{\tau}(n_1 + n_4)\Big]\Big) = 0 \\ p_y^{\perp\prime} &= \frac{1}{\sqrt{2}\tau}\Big(\tau\Big[n_1 - n_4 - \tau(n_2 - n_3)\Big] + \chi_{22}\Big[n_2 - n_3 + \tau(n_1 - n_4)\Big]\Big) = 0 \end{aligned} \tag{90}$$

Now renaming the integer parameters as $n_1 + n_4 - n_2 - n_3 = k$; $-(n_1 + n_4) = l$; $n_1 - n_4 = m$; $n_2 - n_3 = n$, we arrive at the equations that were used by Kiselev to construct approximants with orthorhombic unit cells

$$\begin{aligned} \chi_{11}(\tau k + l) + \tau l - k &= 0 \\ \chi_{22}(\tau m + n) + \tau(m - \tau n) &= 0. \end{aligned} \tag{91}$$

Then the phasonic strain must have the form

$$\chi_{11} = \frac{k/l - \tau}{\tau k/l + 1}, \qquad \chi_{22} = -\tau\frac{m/n - \tau}{\tau m/n + 1}. \tag{92}$$

It is now easy to see that the sets of all such χ_{11} or χ_{22} are dense in $\mathbb{R}$. As we started with an arbitrary lattice vector all approximants that can be created with the diagonal $\boldsymbol{\chi}$-matrix above are fully defined by two rational numbers $k/l, m/n \in \mathbb{Q}$. Because of the isomorphism between the two χ-bases (eq. (50) in section 3.1.2), also the sets $\{\chi_{6,\mathrm{p}}\}$, $\{\chi_{8,\mathrm{p}}\}$ are dense.

Next we want to find the distribution of $\mathcal{L}^{\perp}$'-points in $E^{\perp}$ for a given $\boldsymbol{\chi}$. For that consider again an arbitrary point $\boldsymbol{v}' = \sum_{i=1}^{4} v_i \boldsymbol{a}_i' \in \mathcal{L}'$. Again, we write its $E^{\perp}$-components and perform some substitutions

$$
\begin{aligned}
v_x^{\perp\prime} &= \sqrt{\frac{\tau}{2\sqrt{5}}}\Big(\underbrace{(\chi_{11}/\tau^2 - \tau)}_{A^{(x)}} \underbrace{(v_1 + v_4)}_{z_1^{(x)}} + \underbrace{(1/\tau - \chi_{11})}_{B^{(x)}} \underbrace{(v_2 + v_3)}_{z_2^{(x)}} \Big) \\
v_x^{\perp\prime} &= \frac{1}{\sqrt{2}}\Big(\underbrace{(1 + \chi_{22})}_{A^{(y)}} \underbrace{(v_1 - v_4)}_{z_1^{(y)}} + \underbrace{(\chi_{22}/\tau - \tau)}_{B^{(y)}} \underbrace{(v_2 - v_3)}_{z_2^{(y)}} \Big).
\end{aligned}
\tag{93}
$$

Pulling $B^{(x)}$ and $B^{(y)}$ out of the braces we have $v_j^{\perp\prime} \propto B^{(j)}(\frac{A^{(j)}}{B^{(j)}} z_1^{(j)} + z_2^{(j)}), \quad j \in \{x, y\}$. Using the form of χ_{11} and χ_{22} from eq.(92), the coefficients can be reformulated like

$$
\begin{aligned}
B^{(x)} &= \frac{\sqrt{5}}{\tau k/l + 1}, \qquad A^{(x)}/B^{(x)} = -(l+k)/l \\
B^{(y)} &= \frac{\sqrt{5}\tau}{\tau + n/m}, \qquad A^{(y)}/B^{(y)} = -n/m.
\end{aligned}
\tag{94}
$$

The whole lattice $\mathcal{L}^{\perp\prime}$ is found by all possible integer parameter combinations. We write the lattice $\mathcal{L}^{\perp\prime} = \mathcal{L}_x^{\perp\prime} \times \mathcal{L}_y^{\perp\prime}$ in terms of its sublattices in x and y-direction

$$
\begin{aligned}
\mathcal{L}_x^{\perp\prime} &= \Big\{ \sqrt{\frac{\tau}{2\sqrt{5}}} B^{(x)} \Big(\frac{-(k+l)}{l} z_1^{(x)} + z_2^{(x)} \Big) \mid z_1^{(x)}, z_2^{(x)} \in \mathbb{Z} \Big\} \\
\mathcal{L}_y^{\perp\prime} &= \Big\{ \sqrt{\frac{1}{2}} B^{(y)} \Big(\frac{-n}{m} z_1^{(y)} A^{(y)}/B^{(y)} + z_2^{(y)} \Big) \mid z_1^{(y)}, z_2^{(y)} \in \mathbb{Z} \Big\}.
\end{aligned}
\tag{95}
$$

It is well known that any set $\{\frac{p}{q} n + m | n, m \in \mathbb{Z}\}$ with coprimes $p, q \in \mathbb{Z}$ is equal to the periodic lattice $\{n/q | n \in \mathbb{Z}\}$, where $|1/q|$ is the shortest possible distance between two lattice points. Then, assuming k, l, and m, n are coprime, the shortest distance ε_x, ε_y between two points in $\mathcal{L}_x^{\perp}$ and $\mathcal{L}_x^{\perp}$ are

$$
\begin{aligned}
\varepsilon_x &= \sqrt{\frac{\tau}{2\sqrt{5}}} B^{(x)} \frac{1}{l} = \sqrt{\frac{\sqrt{5}\tau}{2}} \frac{1}{\tau k + l} \\
\varepsilon_y &= \sqrt{\frac{1}{2}} B^{(y)} \frac{1}{m} = \sqrt{\frac{5}{2}} \frac{\tau}{\tau m + n}.
\end{aligned}
\tag{96}
$$

The closer the points of $\mathcal{L}^{\perp\prime}$ lie together, the smaller will be the error when calculating atom configuration densities with the polar calculus. As explained in section 2.2.5, for a densely filled window, meaning $\varepsilon_x = \varepsilon_y = 0$, the polar calculus is exact. From eq. (92) we see that as χ approaches zero the rational numbers k/l and m/n must approximate the golden mean τ better and better. This demands for larger and larger coprimes k, l and m, n, making ε_x and ε_y smaller and approaching zero. So by choosing a χ-interval around zero sufficiently small, the error of the polar calculus will also become arbitrarily small. Hence $\lim_{\chi \to 0} \rho(\chi) = \widehat{\rho}(0)$.

On the other hand, if ε_x, ε_y become large, i.e. for small numbers k, l, m, n, the deviation between the true density $\widehat{\rho}$ of an atom configuration and the calculated one, ρ, will increase. In section 2.2.6, it was shown for a 1D CPS that under certain conditions the polar calculus can function for arbitrary approximants. But that is generally not the case for the 2D approximants defined above as any example calculation will show. One extreme example is shown in fig. 60. On the left, the lattice $\mathcal{L}^{\perp\prime}$ of the Xi-approximant

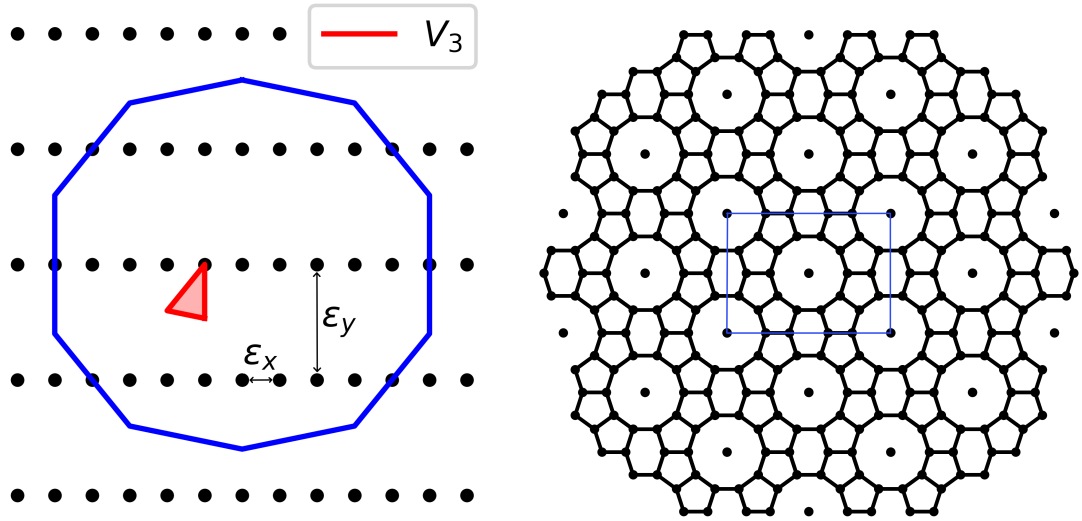

(a) (b)

Figure 58: (a): $\mathcal{L}^{\perp\prime}$-lattice of the Xi-approximant with lattice constants ε_x, ε_y. The window (blue) includes large empty areas. Also the AD of the V_3-vertex is empty. (b): A patch of the Xi-approximant with unit cell in blue. It has no vertices of type V_3.

is depicted, which is obtained from choosing $k = 3$, $l = 2$, $m = 2$, $n = 1$. The Xi-approximant in $E^{\parallel}$ is shown on the right. The red triangle is the AD of the vertex type V_3 in a certain orientation. It was computed with respect to the distorted lattice $\mathcal{L}'$, according to eq. (69) of section 4.1. Its area is $|\overline{V_3}(\boldsymbol{\chi})| = 0.0277$. Then, according to the polar calculus, the density of this V_3-vertex in the Xi-approximant would be

$$\rho_{V_3} = \frac{|\overline{V_3}(\boldsymbol{\chi})|}{|\mathcal{W}(\boldsymbol{\chi})|} = 0.009.$$

But as one can see in the Xi-patch in fig. 58b the V_3-vertex configuration is actually not present at all. This is also apparent in $E^{\perp}$ as there are no $\mathcal{L}^{\perp\prime}$-points inside $\overline{V_3}$. One point touches the corner, but it is not supposed to be counted. Recall that the window is a half open set which causes also the ADs to be partially open. So the percentage error of the polar calculus in this case is actually 100%.

From figure 58a, it is also easy to understand why the density function $\widehat{\rho}|_{\{\chi_\mathrm{p}\}}$ for an arbitrary AD, restricted to approximants is discontinuous. Whenever a change of χ changes the value of $\widehat{\rho}|_{\{\chi_\mathrm{p}\}}$, a finite number of $\mathcal{L}^{\perp}$-points enter or exit the AD. So $\widehat{\rho}|_{\{\chi_\mathrm{p}\}}$ must always increase or decrease at least by an amount $\frac{1}{\#(\mathcal{W}(\chi))}$, where $\#(\mathcal{W}(\chi))$ is the number of $\mathcal{L}^{\perp}$-points in the window. So in any χ-interval, $\widehat{\rho}|_{\{\chi_\mathrm{p}\}}$ is either constant or it jumps abruptly. As the free energy $F|_{\{\chi_\mathrm{p}\}}$ is a linear combination of density functions corresponding to ADs that cover the whole window, it is certain that at least one of these density functions changes for any change of χ_ap. So $F|_{\{\chi_\mathrm{p}\}}$ will be discontinuous everywhere.

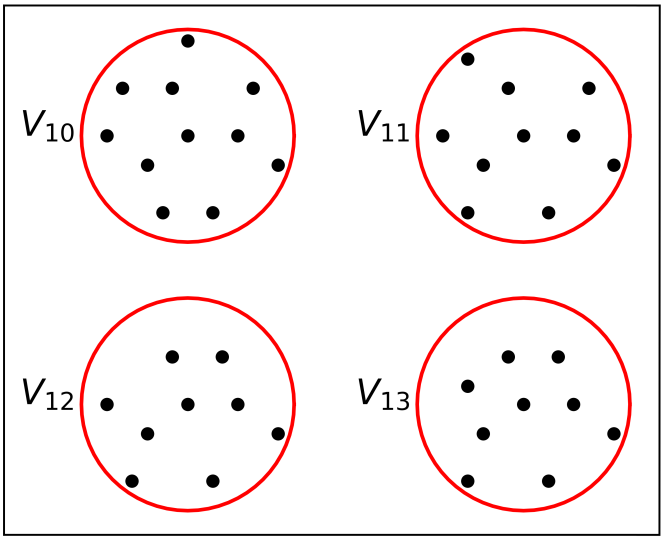

Figure 59: New vertices that appear due to phasonic strain, or due to single flips. The red circle marks the interaction circle of the central atom.

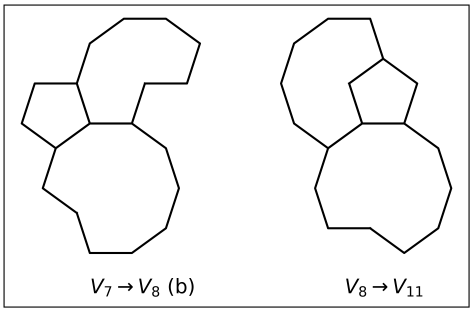

(a) These configurations are present in crystals $\mathcal{Q}(|\chi_6| > 0.01)$.

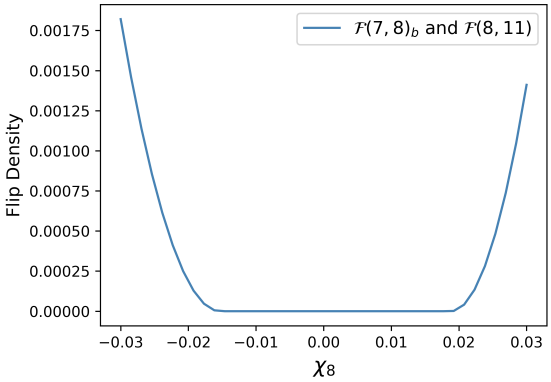

(b) Both flip clusters have the same density function. Its also shows that the densities of atom configurations are i.g. not symmetric functions of χ. This is not a surprise because already the windows area $|\mathcal{W}(\chi)|$ is asymmetric over χ.

Figure 60

8.3 Other Vertices and Flips

Just for completeness, some vertices and flips that were mentioned in certain sections will be displayed here. Firstly, there is the vertex type called V_{10} that appears due to $\chi_8 > 0$. Besides being a flippable vertex itself, it can also emerge as a side effect of several other flips, like $\mathcal{F}(7,9)_a$. It is shown in fig. 59 together with the vertices V_{11}, V_{12} and V_{13}. The latter ones do not occur in any of the flat tilings with $|\chi| < 0.03$, but they are possible flip states of some of the vertices $V_4, .., V_{10}$. The Flip clusters $\mathcal{F}(7,8)_b$ and $\mathcal{F}(8,10)$ (fig. 60a) show up in phasonically distorted crystals $\mathcal{Q}(\chi_6 > 0.01)$. They were not included in

the free energy calculations. Due to their non-parabolic density function (fig. 60b) their contributions to F are clearly beyond the second order approximation of section 3.1.2.

8.4 About the Cutoff Radius $r_c = 2.5$

With a cutoff radius $r_c = 2.5$, it is i.g. no longer possible to define flips according to the vertex environments V_i of their two states, where V_i are defined for a radius $r_c = 2$. An example is the flip $\mathcal{F}(5, 12)$ in fig. 61. Within an interaction circle of radius 2, its two variants $\mathcal{F}(5, 12)_a$ and $\mathcal{F}(5, 12)_b$ are indistinguishable. In the larger circle of radius $r_c = 2.5$, they are distinguished as they are based either on an N-tile (a) or on a U-tile (b). Such a geometrical difference must not necessarily impact the flip energies, but in this case it does. Assuming that the rest of the red circles in fig. 61 is filled identically for both variants, the configuration (a) has one more neighbouring atom at a distance $2.455 < 2.5$ (marked as a red dot), than the configuration (b). This causes a difference in the potential energies of the two variants, which then again corresponds also to a difference of flip energies. The precise energies of this example are not interesting though. For both sizes of interaction circles, the flip energy will be so large ($\Delta E > 6$) that the flips have essentially vanishing thermal probabilities at temperatures $T < T_m = 0.56$. The flips that were used by Kiselev are not subject to such an energy splitting when the cutoff radius is increased from 2 to 2.5.

Another, perhaps more important example is the flip $\mathcal{F}(7, 7)_b$, which contributes significantly to the phasonic constants. For $r_c = 2$, its flip energy is zero since its two states are of the same vertex type V_7. For $r_c = 2.5$, this changes. There are only 3 possible atom distances in the crystals $\mathcal{Q}(|\chi| < 0.03)$ that are shorter than 2. Increasing the cutoff to 2.5, there are 6 possible atom distances. The distances $d < 2.5$ between the flip atom of a $\mathcal{F}(7, 7)_b$ configuration and its neighbouring atoms are shown in fig. 62 for both flip states. While the numbers of neighbour atoms within the $r_c = 2$-circle does not change upon flipping, the numbers of neighbours with distance $2 < d < 2.5$ does. In the right state, x_2, there is one more point on the forth neighbouring shell and two points less on the sixth neighbouring shell. The radii of these shells are $d_4 = 2.018$ and $d_6 = 2.455$. Hence, the energy difference between the two states is

$$\Delta E_{\mathcal{F}(7,7)_b} = |V_{\mathrm{LJG}}(2.018) - 2V_{\mathrm{LJG}}(2.455)| = 0.015. \tag{97}$$

The left state, x_1, in fig. 62 is mainly characterized by the two N-tiles on top of each other. The state x_2, includes a new tile, which we shall call 'S-tile' due to its shape. It is the tile that produces the extra point in the fourth neighbouring shell that would not be there in $\mathcal{F}(7, 7)_a$. This extra atom with distance 2.018 from the blue flip-atom, and therefore the S-tile, is what makes x_2 more stable than x_1. Though the energy difference is very small, there is actually empirical evidence for the stability of the S-tile. Consider the large screenshot of the MD-crystal from Engel's simulation, fig. 28. Counting the presence of the two flip states of $\mathcal{F}(7, 7)_b$, we find the combination of N-tiles as in x_1 only five times, but the S-tiles more than 18 times. At least 17 of these S-tiles are equipped with P-tiles and H-tiles as in x_2. So they could in principle flip into the state x_1. But apparently, very few of them do. The advantageous effect of the S-tile on energetic stability discussed above is a reasonable explanation for this asymmetry in the densities of the flip states of $\mathcal{F}(7, 7)_b$.

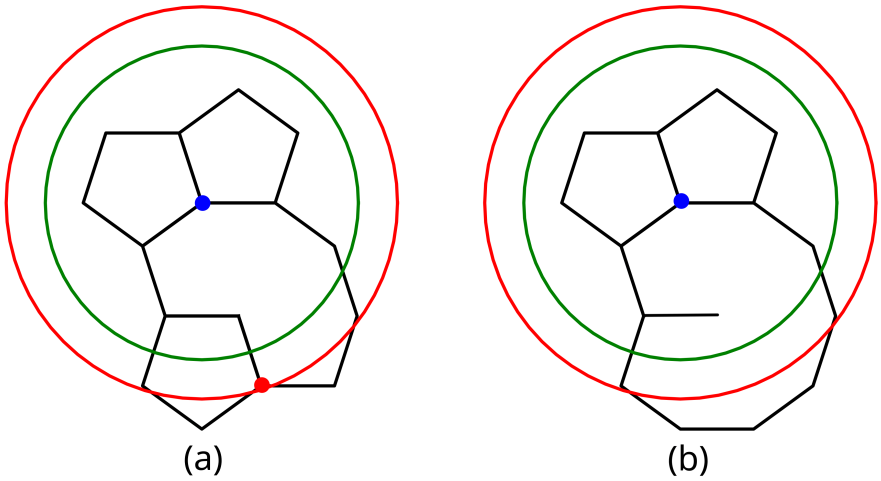

Figure 61: The flips $\mathcal{F}(5,12)_a$ and $\mathcal{F}(5,12)_b$ with interaction circles of radius 2 and 2.5. In the small circle both variants have the same number of neighbour atoms. In the big circle $\mathcal{F}(5,12)_a$ has one atom more.

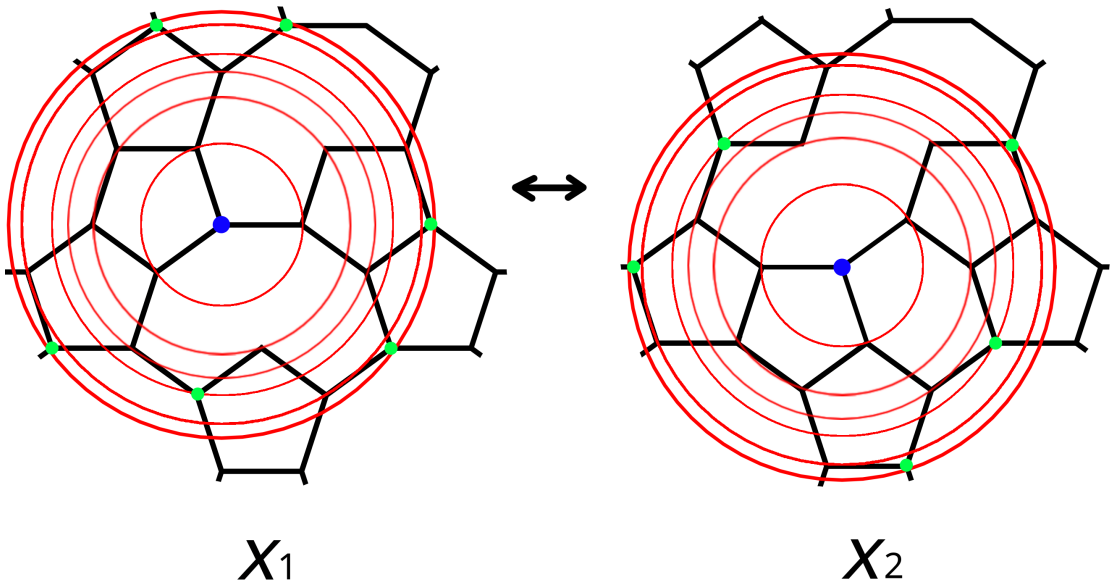

Figure 62: The two states of $\mathcal{F}(7,7)_b$ with an interaction circle of radius 2.5. The six possible distances between the flip atom and its neighbours are marked by smaller circles. The numbers of neighbour atoms on the 4th and 6th circle (marked by green dots) are not equal for both states.

9 Abbreviations

- QC $\widehat{=}$ Quasicrystal
- SR $\widehat{=}$ Substitution Rule
- LI $\widehat{=}$ Local Indistinguishability
- MLD $\widehat{=}$ Mutual Local Derivability
- PT $\widehat{=}$ Penrose Tiling
- RD $\widehat{=}$ Robinon's Decomposition
- ABT $\widehat{=}$ Ammann-Beenker Tiling
- TTT $\widehat{=}$ Tübingen Triangle Tiling
- RT $\widehat{=}$ Random Tiling
- CPS $\widehat{=}$ Cut and Project Scheme
- AD $\widehat{=}$ Acceptance Domain
- GPS $\widehat{=}$ Global Phasonic Strain
- IR $\widehat{=}$ Irreducible Representation
- LJG $\widehat{=}$ Lennard-Jones Gauß
- MD $\widehat{=}$ Molecular Dynamics
- MC $\widehat{=}$ Monte Carlo
- PC $\widehat{=}$ Pentagonal Coupling
- RC $\widehat{=}$ Restrictive Coupling

10 References

[1] Scholz E., Brieskorn E. (2019): Klassische Gestalten und moderne Strukturen in Geometrie und Kristallographie, chapter 4, page 689; script of the lecture 'Lineare Algebra III - Teil B' by Egbert Brieskorn, edited and published by Erhard Scholz, *University Wuppertal*, Digital Edition (open access)
https://www.imaginary.org/de/background-material/lineare-algebra-iii-teil-b

[2] Ball P. (2011): In retrospect: On the Six-Cornered Snowflake, *Nature*, Vol **480**, 455
https://doi.org/10.1038/480455a

[3] Uwe Grimm (2015): Aperiodic crystals and beyond, *Acta Crystallography section B*, Vol **71**, 3, pages 258-274
https://doi.org/10.1107/S2052520615008409

[4] D. Shechtman, I. Blech, D. Gratias, and J. W. Cahn (1984): Metallic Phase with Long-Range Orientational Order and No Translational Symmetry, *Physical Review Letters*, Vol **53**, 20, pp 1951-1953
https://doi.org/10.1103/PhysRevLett.53.1951

[5] Henley C. (1991): Random Tiling Models, pp. 429-524 in Quasicrystals - The State Of The Art ed. DiVincenzo D., Steinhardt P. *World Scientific Publishing* Singapore (1991)
https://doi.org/10.1039/C2CS35120J

[6] Strandburg K. (1989): Random-tiling quasicrystal, *Phys. Rev. B*, Vol **40**, 6071
https://doi.org/10.1103/PhysRevB.40.6071

[7] Zeger G., Plachke D., Carstanjen H. and Trebin H-R. (2000): Is d-Al–Cu–Co a random tiling?, *Materials Science and Engineering: A*, Vol **294-296**, pp. 291-294
https://doi.org/10.1016/S0921-5093(00)01214-4

[8] Richard C., Höffe M., Hermisson J., Baake M. (1998): Random tilings: concepts and examples, *J. Phys. A: Math. Gen*, Vol **31**, 6385
https://iopscience.iop.org/article/10.1088/0305-4470/31/30/007/pdf

[9] Engel M. (2008): Dynamics and Defects of Complex Crystals and Quasicrystals: Perspectives from Simple Model Systems (Dissertation, Physik). *Universität Stuttgart*
https://tinyurl.com/mv2jtbce

[10] Kiselev A. (2011): Phasonen in quasikristallinen Strukturen des Lennard-Jones-Gauß-Systems (Diplomarbeit, Physik). *Universität Stuttgart*
https://tinyurl.com/mwmpvzj5

[11] Baake M., Kramer P., Schlottmann M., Zeidler D. (1990): PLANAR PATTERNS WITH FIVEFOLD SYMMETRY AS SECTIONS OF PERIODIC STRUCTURES IN 4-SPACE, *Int. J. Mod. Phys.*, Vol **40**, 15n16, pp. 2217–2268
https://doi.org/10.1142/S0217979290001054

[12] Kleber W., Bautsch H. J. and Bohm J. (1990): Einführung in die Kristallographie, page 15, 19, *Verlag Technik*
https://bit.ly/3rAUnfq

[13] Hoffmann F. (2016): Introduction to Crystallography, *Springer Fachmedien Wiesbaden GmbH*
https://bit.ly/3OlZZ6Z

[14] Dana E. S. (1922): A Textbook of Mineralogy (3. edition), page 25, 26, *John Wiley and Sons Inc. New York*
https://bit.ly/380i6i3

[15] Wilson C. C. (2000): Single Crystal Neutron Diffraction From Molecular Materials, page 22, *World Scientific Publishing Co. Pte. Ltd*
shorturl.at/nyDS4

[16] McCusker L. B. and Baerlocher C. (2013): Electron crystallography as a complement to X-ray powder diffraction techniques, from Zeitschrift für Kristallographie - Crystalline Materials, page 1-10, *Oldenburg Wissenschaftsverlag*
shorturl.at/fjmBL

[17] Cowley J. M. (1995): Diffraction Physics (third edition), *Elsevier Science B. V.*
shorturl.at/bqJK4

[18] Warren B.E. (1940): X-Ray Diffraction Study of the Structure of Glass, *Chemical Reviewa* Vol. **26**, 2, pp. 237-255
https://doi.org/10.1021/cr60084a007

[19] Kelley S.S., Rials T.G., Glasser W.G. (1987): Relaxation behaviour of the amorphous components of wood, *J Mater Sci* Vol **22**, pp. 617–624
https://doi.org/10.1007/BF01160778

[20] Unge M., Christen T. and Törnkvist C. (2012): Electronic structure of polyethylene — Crystalline and amorphous phases of pure polyethylene and their interfaces, *2012 Annual Report Conference on Electrical Insulation and Dielectric Phenomena*, pp. 525-530
https://doi.org/10.1109/CEIDP.2012.6378835

[21] Baake M. and Grimm U. (2013): Aperiodic Order Volume 1: A Mathematical Invitation (3. edition), *Cambridge University Press*
https://tinyurl.com/2sn5t43k

[22] Terence J. Kemp, Nataniel W. Alcock, 100 years of X-ray crystallography, *Science Progress*, March 2017 pages 25-44
https://doi.org/10.3184/003685017X14858694684395

[23] Bronwen W.Cribb, RonRasch, JohnBarry, Christopher M.Palmer, Distribution of calcium phosphate in the exoskeleton of larval Exeretonevra angustifrons Hardy (Diptera: Xylophagidae), Arthropod Structure Development, Vol. **34**, 1, pages 41-48 (2005)
https://doi.org/10.1016/j.asd.2004.08.002

[24] Online Dictionary of Crstallography from the IUC
https://dictionary.iucr.org/Crystal

[25] Ludwig W., Falter C. (1988): Symmetries in Physics. Group Theory Applied to Physical Problems, *Springer Verlag Berlin Heidelberg*
shorturl.at/jnuH8

[26] Erhard Scholz (1989): Symmetrie Gruppe Dualität - Zur Beziehung zwischen theoretischer Mathematik und Anwendungen in Kristallographie und Baustatik des 19. Jahrhunderts, pages 55-62, *Birkhäuser Verlag, Basel, Boston, Berlin*
shorturl.at/dzLO1

[27] Saurel P. (1911): On the Classification of Crystals, *Bulletin of the American Mathematical Society*, Vol. **17**, 8, pp. 398-409

[28] Online Dictionary of Crystallography from the IUC
https://dictionary.iucr.org/Laue_class

[29] Batterman B.W. and Cole H. (1964): Dynamical Diffraction of X Rays by Perfect Crystals, *Rev. Mod. Phys*, Vol **36**, 681, pp.
https://doi.org/10.1103/RevModPhys.36.681

[30] Okaya Y., Saito Y. and Repinsky R. (1955): New Method in X-Ray Crystal Structure Determination Involving the Use of Anomalous Dispersion, *Phys. Rev*, Vol **98**, pp. 1857-1858
https://doi.org/10.1103/PhysRev.98.1857

[31] Jagannathan A., Duneau M. (2013): An eightfold optical quasicrystal with cold atoms, *EPL*, Vol **104**, 66003
https://doi.org/10.1209/0295-5075/104/66003

[32] Katrych S., Weber T., Massüger L., Kobas M., Palatinus L., Chapius G., Steurer W. (2007): New stable decagonal quasicrystal in the system Al–Ir–Os, *Journal of Alloys and Compounds*, Vol **428**, pp. 164–172
https://doi.org/10.1016/j.jallcom.2006.03.064

[33] Jayaraman A., Baez-Cotto C., Mann T., Mahanthappa M. (2021): Dodecagonal quasicrystals of oil-swollen ionic surfactant micelles, *PNAS*
https://doi.org/10.1073/pnas.2101598118

[34] Bindi L., Steinhardt P. J., Yao N. and Lu P. J. (2009): Natural Quasicrystals, *Science*, Vol **324**, 5932, pp. 1306–1309
https://doi.org/10.1126/science.1170827

[35] Bindi L., Eiler J. M., Guan Y., Hollister L. S., MacPherson G., Steinhardt P. J., Yao N. (2012): Evidence for the extraterrestrial origin of a natural quasicrystal *Proceedings of the National Academy of Sciences* Vol **109**, 5, pp. 1396–1401
https://doi.org/10.1073/pnas.1111115109

[36] Bindi L., Steinhardt P., Kolb W., Eby G. (2021): Accidental synthesis of a previously unknown quasicrystal in the first atomic bomb test, *PNAS*
https://doi.org/10.1073/pnas.210135011

[37] M.C. Escher (1938): Two Birds
https://www.wikiart.org/en/m-c-escher/two-birds

[38] Weisstein, Eric W. "Wallpaper Groups." From MathWorld–A Wolfram Web Resource
https://mathworld.wolfram.com/WallpaperGroups.html

[39] D. Frettlöh, E. Harriss, F. Gähler: Tilings encyclopedia
(See this page for tiling pictures and information about their inventor.)
https://tilings.math.uni-bielefeld.de/

[40] Sing B., Wellberry T. R. (2006): Deformed model sets and distorted Penrose tilings, from Zeitschrift für Kristallographie - Crystalline Materials, page 621-634, *Oldenburg Wissenschaftsverlag München*
https://doi.org/10.1524/zkri.2006.221.9.621

[41] Senechal M. (1996): Quasicrystals and Geometry, chapter 7.2, pp. 209–213, *Cambridge University Press*
shorturl.at/hzFQX

[42] Socolar J.E.S. and Taylor J.M. (2011): Forcing Nonperiodicity with a Single Tile, *arXiv:1009.1419v2 [math.CO]*
https://arxiv.org/pdf/1009.1419.pdf

[43] Baake M. (1999): A Guide to Mathematical Quasicrystals, *arXiv:math-ph/9901014*
https://doi.org/10.48550/arXiv.math-ph/9901014

[44] Rokhsar D., Wright D., Mermin N. (1988): The Two-Dimensional Quasicrystallographic Space Groups with Rotational Symmetries less than 23-Fold, *Acta Cryst. A*, Vol **44**, pp. 197-211
https://doi.org/10.1107/S0108767387010511

[45] Onoda G.Y., Steinhardt P.J., DiVincenco D.P. and Socolar J.E.S. (1988): Growing Perfect Quasicrystals, *Phys. Rev. Let.* Vol **60**, 25, pp. 2653-2656
https://physics.princeton.edu//~steinh/growthQC.pdf

[46] Bruijn, de, N. G. (1981): Algebraic theory of Penrose's non-periodic tilings of the plane. I, II : dedicated to G. Pólya. Indagationes Mathematicae, Vol **43** (1), pp. 39-66
https://pure.tue.nl/ws/files/4344195/597566.pdf

[47] Levitov L.S., (1988): Local Rules for Quasicrystals, *Commun. Math. Phys.* Vol **119**, pp. 627-666
https://doi.org/10.1007/BF01218348

[48] Koschella U. (2005): Phason-elastische Energie in dekagonalen Quasikristallen (Dissertation, Physik). *Universität Stuttgart*
shorturl.at/pyBL9

[49] Au-Yang H., Perk J. (2006): QUASICRYSTALS: PROJECTIONS OF 5-D LATTICE INTO 2 AND 3 DIMENSIONS, *arXiv:math-ph/0606028*
https://doi.org/10.48550/arXiv.math-ph/0606028

[50] Zeger G. (1995): Strukturmodelle und ihre Anwendung: Die dekagonale quasikristalline T–Phase d–AlCuCo (Diplomarbeit, Physik). *Universität Stuttgart*
https://elib.uni-stuttgart.de/bitstream/11682/4650/1/diplom.pdf

[51] Grant Glouser, cut-and-project-tiling, *programm on GitHub*
https://github.com/gglouser/cut-and-project-tiling

[52] Katz A., Duneau M. (1986): Quasipeeriodic Patterns and Icosahedral Symmetry, *J. Phys. France* Vol *47*, pp. 181-196
https://doi.org/10.1051/jphys:01986004702018100

[53] Au-Yang H., Perk J. (2013): Quasicrystals—The impact of N.G. de Bruijn, *Indagationes Mathematicae*, Vol **24**, 4, pp. 996-1017
https://doi.org/10.1016/j.indag.2013.07.003

[54] Vekilov Y., Isaev E., Arslanov S. (2000): Influence of phason flips, magnetic field, and chemical disorder on the localization of electronic states in an icosahedral quasicrystal, *Phys. Rev. B*, Vol **62**, 14040
https://link.aps.org/doi/10.1103/PhysRevB.62.14040

[55] Sokolar J., Lubensky T., Steinhardt P. (1986): Phonons, phasons, and dislocations in quasicrystals, *Phys. Rev. B*, Vol **34**, 3345
https://link.aps.org/doi/10.1103/PhysRevB.34.3345

[56] Abe E., Pennycook S., Tsai A. (2003): A. Direct observation of a local thermal vibration anomaly in a quasicrystal, *Nature*, Vol **421**, pp. 347–350
https://doi.org/10.1038/nature01337

[57] Freedman B, Bartal G., Segev M. et al. (2006): Wave and defect dynamics in nonlinear photonic quasicrystals, *Nature*, Vol **440**, pp. 1166–1169
https://doi.org/10.1038/nature04722

[58] Yamada T., Takakura H., Euchner H. et al. (2016): Atomic structure and phason modes of the Sc–Zn icosahedral quasicrystal, *IUCrJ*, Vol **3**, 4 pp. 247-258
https://doi.org/10.1107/S2052252516007041

[59] Baake M., Grimm U., Moody R. (2002): What is Aperiodic Order?, *arXiv:math/0203252v1 [math.HO]*
https://doi.org/10.48550/arXiv.math/0203252

[60] Baake M., Grimm U. (2012): Mathematical diffraction of aperiodic structures, *Chem. Soc. Rev.*, Vol **41**, pp. 6821-6843
https://doi.org/10.1039/C2CS35120J

[61] Gähler F., Jeong H. C. (1995): Quasicrystalline ground states without matching rules, *J. Phys. A: Math. Gen.*, Vol **28**, 1807
https://iopscience.iop.org/article/10.1088/0305-4470/28/7/006

[62] Burkov S. (1990): Ground states of two-dimensional quasicrystals, *Phys. Rev. B*, Vol **41**, 10413
https://doi.org/10.1103/PhysRevB.41.10413

[63] Koschella U. (2001): Zur Phason-Phonon-Kopplung in dekagonalen Quasikristallen (Diplomarbeit, Physik). *Universität Stuttgart*
https://tinyurl.com/4um6tjxs

[64] Kiselev A., Engel M., Trebin H.-R. (2012): Confirmation of the Random Tiling Hypothesis for a Decagonal Quasicrystal, *Phys. Rev. Lett.*, Vol **109**, 225502
https://doi.org/10.1103/PhysRevLett.109.225502

[65] D. Joseph, M. Baake, P. Kramer, H.-R. Trebin (1994): Diffusion in 2D Quasi-Crystals, *Europhys. Lett.*, Vol **27**, 6
https://iopscience.iop.org/article/10.1209/0295-5075/27/6/007

[66] A. Trub, H.-R. Trebin (1994): Topology of the phason degree of freedom, phason singularities, and diffusive motion in octagonal quasicrystals, *J. Phys. I France*, Vol **4**, 12, pp. 1855-1866
https://doi.org/10.1051/jp1:1994226

[67] A Rudinger, H.-R. Trebin (1994): Phase-induced atomic permutations in icosahedral quasicrystals: a model for self-diffusion, *J. Phys. A:*, Vol **27**, 24
https://iopscience.iop.org/article/10.1088/0305-4470/27/24/010/meta

[68] Bonamente M. (2013): Statistics and Analysis of Scientific Data, 3rd edition, *Springer Science+Business Media New York*
https://doi.org/10.1007/978-981-19-0365-6

[69] Overhauser A. (1971): Observability of Charge-Density Waves by Neutron Diffraction, *Phys. Rev. B*, Vol **3**, 3173
https://doi.org/10.1103/PhysRevB.3.3173

11 Acknowledgements

I want to thank all the people who helped me in the process of working out and writing this master thesis. My gratitude goes first of all to the professors Dr. Johannes Roth and Dr. Hans-Rainer Trebin. I have to thank Mr. Roth already for originally introducing me into the topic of quasicrystals. After offering a lecture on quasicrystals as an extension to the course 'group theoretical methods in physics', he continued to give this lecture even though I was the only participant. He remembered my subsequent request for a master thesis in this field for several months till he and Mr. Trebin had found a possible topic. While working on the thesis he was always available to help out with a huge repertoire of literature as well as profound personal experience and he never hesitated to listen to my results, problems or thoughts about physics in general. The same gratitude I owe also to Mr. Trebin. Having worked on the topic of quasicrsytals for many years and having guided the work on many of the sources that I was using constantly, his experience was unquestionably a big help. But even more than for his knowledge I am thankful for his active participation in my work. He engaged me to discuss my work frequently and looked critically as well as constructively on my ideas and writings. Most importantly though, he managed to assure me about the significance of my work. This emotional support I valued a lot because the fact that I was virtually the only one in the institute working on qusicrystals presented a considerable mental hurdle at times. Nevertheless, the institute FMQ provided a pleasant and comfortable atmosphere for my studies. I felt welcome in the Roth group and enjoyed spending time with its members as well as with the members of the other groups.

12 Ehrenwörtliche Erklärung

Gemäß §24 Abs. 7 der Prüfungsordnung der Universität Stuttgart für den Masterstudiengang Physik (2015) versichere ich hiermit, dass:

- ich diese Masterarbeit selbstständig verfasst habe,
- nur die angegebenen Quellen benutzt wurden und alle wörtlich oder sinngemäß aus anderen Werken verwendeten Aussagen als solche gekennzeichnet wurden,
- diese Masterarbeit weder vollständig noch in wesentlichen Teilen Gegenstand eines anderen Prüfungsverfahrens gewesen ist,
- ich identische elektronische und gedruckte Exemplare eingereicht habe.

Stuttgart, 6. November 2022 Moritz Holzwarth

13 Deutsche Zusammenfassung

In seiner Diplomarbeit von 2011 berechnete Kiselev die phasonelastischen Konstanten eines Quasikristalls, der auf dem Tübinger Dreiecksmuster basiert und dessen atomare Interaktionen von einem Paarpotential namens Lennard-Jones Gauß-Potential bestimmt werden. Seine Arbeit, wie auch die hier gezeigte, basieren auf einer Molekulardynamik-Simulation eines Quasikristalls von Engel aus dem Jahr 2008. Diese Simulation wird zum Vergleich mit empirischen Daten herangezogen.

Das erste Ziel dieser Masterarbeit ist es, die numerisch bestimmten phasonischen Konstanten zu rekonstruieren, allerdings nur durch analytische Methoden. Der zentrale Formalismus hierbei ist das Polarenkalkül, welches zu Beginn der Arbeit erklärt wird. Danach werden einige Aspekte der Arbeiten von Engel und Kiselev diskutiert. Nennenswert ist insbesondere, dass die Theorie der phasonischen Konstanten nicht wohldefiniert ist, im mathematischen Sinne. Sie beruht auf der Annahme, dass die phasonelastische freie Energie, $F(T, \boldsymbol{\chi})$ eine analytische Funktion ist. Es wird erklärt, dass dies i.a. nicht der Fall ist, da $F(T, \boldsymbol{\chi})$ nicht stetig ist. Es gibt jedoch einen natürlichen Weg, um $F(T, \boldsymbol{\chi})$ durch eine stetige Funktion zu approximieren. Diese Funktion, die im Grunde die phasonische freie Energie selbst, nur mit einem auf aperiodische Kristalle beschränkten Definitionsbereich ist, wird berechnet, aber auch wieder nur näherungsweise. Die Näherung liegt in der Beschreibung von phasonischen Flips im QC und verwandten Kristallen. Im sogenannten Flip-Isingmodell, welches bereits von Kiselev eingeführt wurde, werden die Flips wie unabhängige Spin 1/2-Teilchen auf einem Gitter behandelt. Der Unterschied zu Kiselevs Arbeit ist nun, dass die Dichten dieser Flips mittels des Polarenkalküls berechnet werden. Aus einem Vergleich der Grundzustandsenergien $E_0(\chi)$, der Konfigurations-freien Energien $F_c(\chi)$ und der phasonischen Konstanten $\lambda(T)$ ergibt sich, dass der analytische Formalismus die numerischen Ergebnisse im Prinzip akkurat reproduzieren kann. Bezüglich der phasonischen Verzerrung χ_6 stimmen die analytischen Funktionen $E_0(\chi_6)$ und $\lambda_6(T)$ sehr gut mit Kiselevs Plots überein. Weniger gut stimmen die Ergebnisse bezüglich der phasonischen Verzerrung χ_8 überein. Der Unterschied liegt an der von Kiselev verwendeten phasonischen Relaxation, welche im analytischen Flipmodell ungenau wiedergegeben wird. Es wird eine Methode vorgeschlagen und dargestellt, welche es erlaubt, die Effekte der phasonischen Relaxation besser zu berücksichtigen. In der Tat verbessern sich die Ergebnisse aufgrund dieser Korrektur. Ungeachtet der rein quantitativen Unterschiede werden die entscheidenden Erkenntnisse aus Kiselevs Arbeit ebenfalls in den analytischen Ergebnissen gefunden. Diese sind, dass die Theorie der phasonischen Konstanten eine Instabilität des QC bei $T = 0$ vorhersagt und Stabilität oberhalb einer Phasenübergangstemperatur $T_c > 0$. Dies war auch die Beobachtung in Engels Simulation.

Ein weiteres, wichtiges Thema dieser Masterarbeit ist, dass Teile von Kiselevs Diplomarbeit, und dadurch auch deren analytische Rekonstruktion, einer fragwürdigen Annahme unterlagen, welche wir als Flip-Einschränkung oder Flip-Auswahlregel bezeichnen. Als Teil der Diskussion seiner Arbeit erörtern wir, dass jeder Ausschluss von Flips, der nicht auf vernachlässigbaren thermischen Wahrscheinlichkeiten beruht, ungerechtfertigt ist. Unter Verwendung einer größeren, uneingeschränkten Menge von Fliparten wurden die phasonischen Konstanten erneut berechnet. Die Ergebnisse weichen stark von den vorherigen mit der Flip-Einschränkung ab und stimmten kaum noch mit den Beobachtungen der Molekulardynamik-Simulation überein. Daraus schließen wir, dass die Approximation der unabhängigen Flips nicht ausreichend ist, um den Beitrag der Flip-Dynamik zur Stabilität des QC zu erklären.

Drittens wird ein etwas erweitertes Model der Flip-Dynamik vorgeschlagen. Anstatt unabhängiger Einzelflips werden dabei unabhängige Paare von gekoppelten Flips betrachtet. Die Kopplung in jedem Paar ist derart, dass es zehn mögliche Zustände gibt, die als Ecken eines Pentagons dargestellt werden können. Daher werden diese Art der Flip-Interaktion 'Pentagon-Kopplung' (PC) genannt und die Flip-Paare, zusammen mit weiteren Umgebungsatomen 'PC-Cluster'. Es werden 23 Arten von PC-Clustern bestimmt und klassifiziert. Zur Berechnung der freien Energie der PC-Cluster wird eine einfache Erweiterung des Flip-Isingmodells definiert. Außerdem wird erwähnt, dass die PC-Cluster im Prinzip mittels Markovketten beschrieben werden können. Mit diesem neuen Modell, welches weiterhin vollkommen analytisch ist und auf dem Polarenkalkül basiert, werden die phasonischen Konstanten ein weiteres Mal berechnet. Das Ergebnis ist deutlich zufriedenstellender im Vergleich zur vorherigen Rechnung mit unabhängigen Einzelflips. Es sagt einen Phasenübergang bei $T_c = 0.22$ voraus, der unterhalb der empirischen Schmelztemperatur liegt. Dennoch ist es nicht sehr akkurat, denn die empirische Phasenübergangstemperatur liegt bei $T_c = 0.37$. Die Stabilität bei niedrigen aber positiven Temperaturen, die dieses Modell vorhersagt ergibt sich nicht allein aus dem große Phasenraumvolumen der QC-Phase. Es ist eher so, dass der QC bestimmte Atomkonfigurationen fördert, die, in Kombination mit dem LJG-Potential, bereits bei niedrigen Temperaturen eine hohe Entropie haben. Somit wird die Random-Tiling-Hypothese, welche besagt, dass Quasikristalle entropiestabilisierte Hochtemperaturphasen sind, bestätigt am Beispiel eines Modell-QCs mit nichttrivalem Paarinteraktionspotentials. Hierfür werden ausschließlich analytische Methoden verwendet.